H-MODE ACCESS AND CHARACTERISTICS AT NEAR-UNITY ASPECT RATIO ON THE PEGASUS TOROIDAL EXPERIMENT

by

Kathreen E. Thome

A dissertation submitted in partial fulfillment of

the requirements for the degree of

Doctor of Philosophy

(Nuclear Engineering and Engineering Physics)

at the

UNIVERSITY OF WISCONSIN–MADISON

2016

Date of final oral examination: 12/11/2015
The dissertation is approved by the following members of the Final Oral Committee:
David Anderson, Jim and Anne Sorden Professor, Electrical and Computer Engineering
James Blanchard, Duane H. and Dorothy M. Bluemke Professor, Engineering Physics
Raymond Fonck, Steenbock Professor in Physical Science, Engineering Physics
Chris Hegna, Professor, Engineering Physics
John Sarff, Professor, Physics

Abstract

The high-confinement (H-mode) operating regime is achieved at near-unity aspect ratio ($A \lesssim 1.2$) in the Pegasus Toroidal Experiment. Ohmic H-mode is attained via high-field-side fueling and low edge recycling in both limited and diverted magnetic topologies. This features of this regime are: formation of a quiescent edge; reduced D_α emissions; increased core rotation; formation of edge current and pressure pedestals; measured energy confinement consistent with the IPB98(y,2) scaling [1]; and increased heating in the electron and ion channels.

The H-mode power threshold, P_{LH}, behaves quite differently at low-A when compared with high-A operations. The threshold has been studied in both limited and favorable single null diverted plasmas in Pegasus, with $P_{LH} = 10$–$20\times$ higher than projected by the conventional ITPA08 scaling [2]. This continues and emphasizes the trend indicated from other low-A tokamaks, MAST and NSTX, that increasingly more power than predicted by the scaling is required as A decreases. Unlike at higher-A, no minimum P_{LH} with density is observed. Also in contrast to higher-A tokamaks, where P_{LH} is $\gtrsim 2\times$ higher in limited plasmas than diverted plasmas, the threshold in approximately the same in both limited and favorable single null diverted Pegasus plasmas. Some of these P_{LH} results are consistent with the FM^3 model for the L-H transition [3].

Two classes of edge localized modes (ELMs) have been observed. Small, Type III-like ELMs are present at low Ohmic input power P_{OH} and have toroidal mode number $n \leq 4$. At $P_{OH} \gg P_{LH}$, they transition to large, Type-I-like ELMs with intermediate $5 < n < 15$. These ELM magnetic structures behave opposite that of high-A plasmas, with n lower, presumably due to the naturally higher J/B peeling mode drive at low-A. The unique edge plasma parameters afforded by near-unity A operations allow long sought measurements of the edge current profile dynamics during an ELM. Such measurements with a multi-channel magnetic probe array show a complex, multimodal pedestal collapse and the subsequent ejection of a current-carrying filament.

ACKNOWLEDGMENTS

Graduate school has been a life-changing experience, and I appreciate all the support, mentoring, and guidance that has allowed me to persevere through it. It is amazing to think of how I have progressed from an eight year-old child, who almost had to repeat first grade, to where I am now. To all who helped me along this journey, thank you. This path began in primary and secondary school, where I had some amazing teachers: Mrs. Donohue (Calcium Primary School, NY); Mr. Fukuda (Leilehua High School, HI), Mr. Burt (Osbourn Park High School, VA) and Mrs. Liebman (Osbourn Park High School, VA.) In college, Dennis Whyte (MIT), Andrew Zwicker (PPPL), and Soren Harrison challenged me to do quality research and encouraged me to apply to graduate school.

In graduate school, I have been fortunate to have Professor Raymond Fonck as an advisor. Ray has always challenged me to do more and in doing so made me a better scientist. I have learned much about tokamaks, diagnostics, science and politics under his tutelage. However, I most appreciate how he has always been willing to talk about whatever, whenever.

The Pegasus group is a lively and helpful research team. I would like to thank Mike Bongard for his guidance throughout this work. Mike taught me much of what I know about tokamak operations and equilibrium reconstructions. He also helped me to become a more precise scientist. Josh Reusch only recently joined the group, but his positive approach, new ideas, and encouragement were always appreciated. Ben Kujak-Ford was helpful when I broke something (which was often and usually late at night) or when I could not find something (also often and usually above my head.) Ben Lewicki taught me much of what I know about electronics and troubleshooting. Greg Winz taught me much of what I know about vacuum technology. His help in the development of the HFS fueling systems was crucial and very much appreciated.

In my time in graduate school, I have seen many undergraduate and graduate students pass through this group. However, I want to acknowledge the core group of graduate students during my tenure here: Jayson Barr, Galen Burke, Edward Hinson, Justin Perry, and Dave Schlossberg. I have enjoyed working with all of you, and I look forward to seeing your careers progress. I would also like to acknowledge Mike, Jayson, Galen, Justin, Dave, Grant Bodner, and Matt Kriete for data and analysis in this dissertation. These students along with Nate Woodruff, Amir Jaber, Shane Swager, Nikki Schoenbeck, Lara Peguero, Rianna Preston, Terrence Townsend, Mindy Bakken, Dinh Truong, and many others have all made this a positive place to work. My other friends in Madison have made this an enriching place to live.

My family and friends have always offered support, laughter, and good ideas whenever I needed them. Vina Nguyen has always been there for me, no matter what was going on in her life. My extended family have all been very supportive. In particular, my grandparents helped me see the big picture. My parents continually encouraged me throughout my entire schooling. Without their support and love, I would not have the courage to be where I am today. Last but not least, my brother has always made me smile.

Table of Contents

Page

List of Figures

Figure Page

Figure Page

Figure Page

Figure Page

Figure Page

List of Tables

Chapter 1

Introduction and Motivation

This chapter introduces the tokamak and spherical tokamak, magnetic confinement devices, that are used to study plasmas physics and fusion energy. Relevant terminology used throughout this dissertation is introduced. Then the outline of this dissertation is provided.

1.1 The Tokamak

Magnetic confinement fusion is a possible long-term solution to our current worldwide energy crisis. Harnessing nuclear fusion energy would meet our growing worldwide energy demands for many thousand of years to come without generating greenhouse gas emissions or long-lived radioactive materials (>100 years.) Also, there is no possibility of a catastrophic accident in a fusion reactor. In a nuclear fusion reaction, two nuclei fuse into one nuclei and convert a small amount of mass into energy via $E = mc^2$. One fusion reaction releases 13.6 MeV of energy. Thus, one kg of deuterium releases $\sim 10^7\times$ more energy than 1 kg of coal. This is the promise of nuclear fusion — a long-term safe energy source without carbon emissions.

In order for a fusion reaction to occur, two positively charged nuclei must be brought within a nuclear diameter of each other. This is accomplished by providing sufficient energy to overcome their mutual Coulomb repulsion. In the stars, nuclei are concentrated close enough together to fuse by gravity. In lieu of making a star on Earth, magnets are instead used to confine the nuclei and prompt a fusion reaction. Magnetic confinement fusion has been studied worldwide since the 1950s in many different types of confinement devices.

Of the magnetic confinement configurations, the tokamak (an acronym derived from the Russian phrase "toroidalnaya kamera i magnitaya katushka," which translates as "toroidal chamber and magnetic coil"), is seen as the leading contender for the first burning plasma reactor due to its superior physics performance. The tokamak is a toroidal axisymmetric donut-shaped magnetic confinement device and as such the equilibrium magnetic field is independent of the toroidal angle.

A tokamak, with all the relevant fields is shown in Fig. 1.1. Toroidal current is induced in the plasma by a transformer linking the plasma, which creates a poloidal field that confines the plasma. This method, called Ohmic induction, also heats the plasma. A large toroidal field is generated by electromagnetic toroidal field coils. The poloidal electromagnetic field set, or equilibrium field coils, stabilizes the plasma and controls plasma shape. These two magnetic fields together create helical magnetic field lines that wrap around the plasma.

In conventional tokamaks, large aspect ratio tokamaks, the toroidal field is the dominant field. The toroidal field is a strong stabilizing field utilized to magnetically stabilize the plasma for a sufficient period of time for fusion reactions to occur. As the geometry of the plasma changes from that of a donut (large aspect ratio) to more of a cored apple (small aspect ratio), the poloidal and toroidal fields become comparable and other stabilizing effects due to geometry become important. These devices, called spherical tokamaks, will be discussed in Section 1.2.

1.1.1 Tokamak Concepts

To clarify the terminology used in tokamak research and in this dissertation a brief description of some basic concepts is presented; most of the definitions here are found in [4].

Flux surfaces and functions In order for the plasma to be in equilibrium, the force on the plasma must be zero at all points. For this to be accomplished, the magnetic force must balance the force from the plasma pressure. In an axisymmetric system, such as a tokamak, the magnetic field lines lie in closed nested toroidal magnetic surfaces as illustrated in Fig. 1.1 by the nested orange

contours. The outermost closed flux surface is commonly called the last closed flux surface. The general plasma force balance equation used to define the equilibrium is:

$$\vec{j} \times \vec{B} = \vec{\nabla} p, \tag{1.1}$$

where $\vec{j}$ is the current density in A/m^2, $\vec{B}$ is the magnetic field in T, and p is the pressure in Pa. From this equation, it can be derived that $\vec{B} \cdot \vec{\nabla} p = 0$ and $\vec{j} \cdot \vec{\nabla} p = 0$, which means that the magnetic surfaces are surfaces of constant pressure and that the current lines also lie in the magnetic surfaces.

The poloidal magnetic flux function, Ψ, is the amount of poloidal flux within each magnetic surface. Ψ satisfies:

$$\vec{B} \cdot \vec{\nabla} \Psi = 0, \tag{1.2}$$

and it is a constant for each surface.

Plasma shaping The dimensionless parameters commonly used to describe the geometry of a shaped (non-circular) tokamak plasma are: aspect ratio (A), elongation (κ) and triangularity (δ). Figure 1.2 [5, Fig. 1.2] defines these parameters on the poloidal cross-section of a highly-shaped spherical tokamak equilibrium at one location. The plasma major radius, R_0, is the distance from the axis of symmetry to the geometric center of the outermost closed flux surface. The horizontal and vertical minor radii are expressed by a and b, respectively. Elongation is equal to b/a. Aspect ratio is equal to R_0/a. Inverse aspect ratio is denoted ε.

Safety factor The safety factor, q, is named for its role in determining plasma stability against current-driven kink modes. As such, higher values of q lead to greater stability. For a toroidally axisymmetric device, the safety factor of a field line is the number of toroidal circuits it takes to complete one poloidal circuit. A general expression of q that can be used in a system with nested flux surfaces is:

$$q = \frac{d\Phi}{d\Psi}, \tag{1.3}$$

where the toroidal flux is $d\Phi = \oint (B_\Phi dx) ds$, B_Φ is the toroidal field, dx is the distance separating the two surfaces of interest, ds is the distance traveled in poloidal direction while traversing a

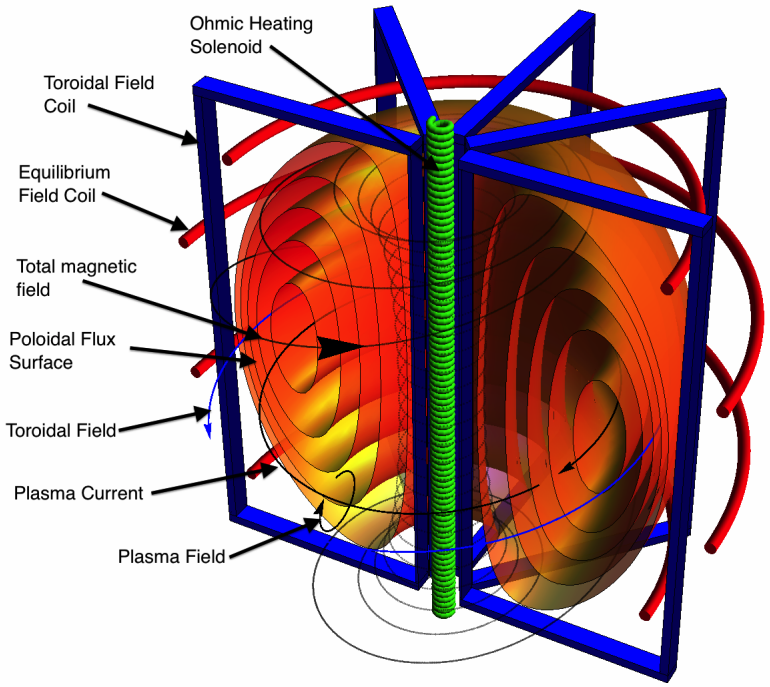

Figure 1.1: Basic tokamak schematic showing the main magnetic field coils (Ohmic solenoid in green, toroidal in blue and equilibrium in red), field lines, and poloidal flux surfaces (orange contours)

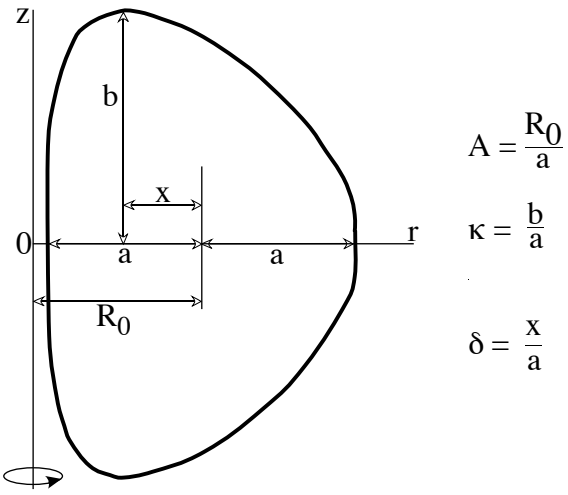

Figure 1.2: Schematic of the last closed flux surface of a highly-shaped plasma cross section, defining pertinent geometric parameters

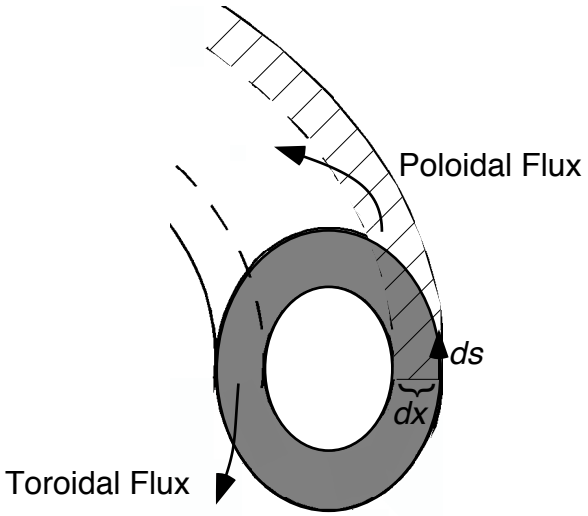

Figure 1.3: Tokamak schematic showing a toroidal flux, Φ, annulus and part of a poloidal flux, Ψ, annulus

toroidal angle $d\Phi$, the poloidal flux is defined as $d\Psi = 2\pi R B_p dx$, and B_p is the poloidal field. Figure 1.3 [5, Fig. 1.3] illustrates a flux annulus formed by this analysis. A large circular aspect ratio approximation for q is:

$$q(r) = \frac{rB_\phi}{R_0 B_p(r)}. \tag{1.4}$$

The q near the edge, q_ψ, is of particular interest for plasma stability. The large aspect ratio q_ψ for highly-shaped plasmas is approximated by the cylindrical q, which is given as [6]:

$$q_{cyl} = \frac{(1+g\kappa^2)}{2}\left[\frac{2\pi a^2 B_{\phi 0}}{\mu_0 I_p R_0}\right] \tag{1.5}$$

where $g = (1 + 2\delta^2 - 1.2\delta^3)$, I_p is the plasma current, and $B_{\phi 0}$ is the toroidal field at R_0. An estimation for q_ψ for a finite aspect ratio tokamak in terms of ε is [7]:

$$q_\psi = q_{cyl}\frac{1.17 - 0.65\varepsilon}{(1-\varepsilon^2)^2}. \tag{1.6}$$

Disruptions A tokamak disruption is a dramatic event that suddenly destroys the plasma confinement and terminates the discharge. There are two main causes of disruptions, low q_ψ and high

density. On large aspect ratio tokamaks $q_{cyl} \geq 3$ is typically taken as a figure-of-merit to prevent q disruptions. Small aspect ratio tokamaks typically require a higher q_ψ in order to avert disruptions. For example on Pegasus, a low aspect ratio tokamak, it was found that $q_\psi > 5$ is necessary to prevent q disruptions [8]. Density disruptions occur at or above an empirical density limit, called the Greenwald limit:

$$n_G = \frac{I_p}{\pi a^2}, \tag{1.7}$$

where n_G is the Greenwald density in $10^{20} m^{-3}$, I_p is in MA, and a is in m [9].

A subset of disruptions are vertical disruption events (VDEs), which is a loss of vertical position control. In a VDE, the plasma strikes the top or bottom of the vacuum vessel and then disrupts [10]. Vertical stability is usually characterized by the field index number, n^*, where

$$n^* = -\frac{R}{B_Z}\frac{\partial B_z}{\partial R}. \tag{1.8}$$

When $n^* > 0$, the plasma is vertically stable [5].

To prevent disruptions, tokamaks generally operate above the low-q disruption limit, below the Greenwald density limit, and with vertical position control.

Beta Beta, β, is a measure of the efficiency of the plasma pressure confinement by the magnetic field as given by:

$$\beta = \frac{p}{B^2/2\mu_0}. \tag{1.9}$$

The toroidal beta, β_t, is defined by:

$$\beta_t = \frac{\langle p \rangle}{B_T^2/2\mu_0}, \tag{1.10}$$

where $\langle\,\rangle$ denotes volume averaging. β_t is typically given as a percent. Achieving a high β_t is desirable since fusion power; P_F, goes as [11]:

$$P_F \approx B^4 \beta_t^2. \tag{1.11}$$

Troyon *et al.* [12] found that there is a limit to the value of β_t that a tokamak can attain and still remain stable to plasma pressure gradients. This limit is expressed via normalized beta, β_N, and it is defined by:

$$\beta_t = \beta_N \frac{I_p}{aB_t}, \tag{1.12}$$

where the quantity (I_p/aB_t) is called the normalized current, I_N, and β_N is expressed as:

$$\beta_N = \frac{\beta_t}{I_N}.$$

In the Troyon limit, β_N =2.8. The toroidal field utilization factor, I_p/I_{TF}, can be related to I_N with $I_N = 5AI_p/I_{TF}$.

The poloidal beta, β_p, is defined by:

$$\beta_p = \frac{\langle p \rangle}{\overline{B}_p^2/2\mu_0}, \tag{1.13}$$

where $\overline{B}_p$ is the average poloidal magnetic field. When $\beta_p \lesssim 1$, the plasma is confined by the poloidal field or by both the poloidal and toroidal field to an equal extent. The plasma is then paramagnetic with respect to the toroidal field. When $\beta_p > 1$, the plasma is confined by the toroidal field and thus diamagnetic with respect to the toroidal field. High values of β_p are desired, since they contribute to the plasma's ability to generate pressure-driven (bootstrap) currents, which reduce the external current drive requirement.

Confinement times and recycling To achieve fusion conditions in a tokamak it is necessary to confine the plasma for a sufficient time. The global energy confinement time, τ_e, is the rate at which energy is lost from the plasma to the environment and is described in steady-state by:

$$\tau_e = \frac{W_k}{P_H}, \tag{1.14}$$

where W_k is the plasma kinetic energy in J and P_H is the supplied heating power in W.

The particle confinement time, τ_p, is the amount of time particles are typically confined in the plasma before interacting with the plasma facing components. The effective particle confinement time, τ_p^*, is corrected for recycling and is described by [13]:

$$\tau_p^* = \frac{\tau_p}{1-R} = \frac{\bar{n}_e}{\frac{d\bar{n}_e}{dt}},$$

where $\bar{n}_e$ is the line-averaged plasma density. The recycling coefficient, R, is the ratio of those particles reentering the plasma after interacting with the walls over the particles leaving the plasma. [14]. A high recycling coefficient is described as $R \approx 1$, which is typical for most experiments. A low recycling coefficient is typically described by $R < 0.9$ [15].

Plasma Geometries There are two main categories of magnetic topologies: limited and diverted. In limited plasmas, the last closed flux surface is defined by a solid surface (the limiter.) Thus, neutral impurity atoms released from the surface can enter directly into the confined plasma. In a divertor, the last closed flux surface, the separatrix, is defined solely by the magnetic field and plasma surface interactions are remote from the confined plasma. A divertor is formed by using an external coil to introduce a local polodial field null at a particular location, defined as the X-point. The use of divertors can lead to increased physics performance due to its impurity and heat flow management, which has led to its widespread adoption. There are two main subtypes of diverted magnetic topologies: single null with a single X-point that is further differentiated into upper single null and lower single null and a double null with two X-points. These three magnetic plasma geometries are demonstrated in Fig. 1.4 [16, Fig. 1.4].

1.2 The Spherical Tokamak

Spherical tokamaks, STs, are unique experiments that can study tokamak physics relevant to much larger aspect ratio machines at a smaller cost and scale. STs have many possible benefits, including: lower required magnetic field energy for a given performance and high neutron fluxes. Thus, they are candidates for fusion materials test facilities [17]. They typically have $A \leq 2$ [18]. In contrast, most modern large aspect ratio tokamaks have $A \sim 3-5$. A comparison of equal-volume low aspect ratio and high aspect ratio tokamaks is shown in Fig. 1.5. This figure also demonstrates the relevant tokamak directions: the poloidal direction, θ, the toroidal direction, ϕ, and the major radius direction, R. The compact nature of the ST leads to a very small center column on the inboard side of the plasma, which allows for more efficient field utilization. More efficient use of

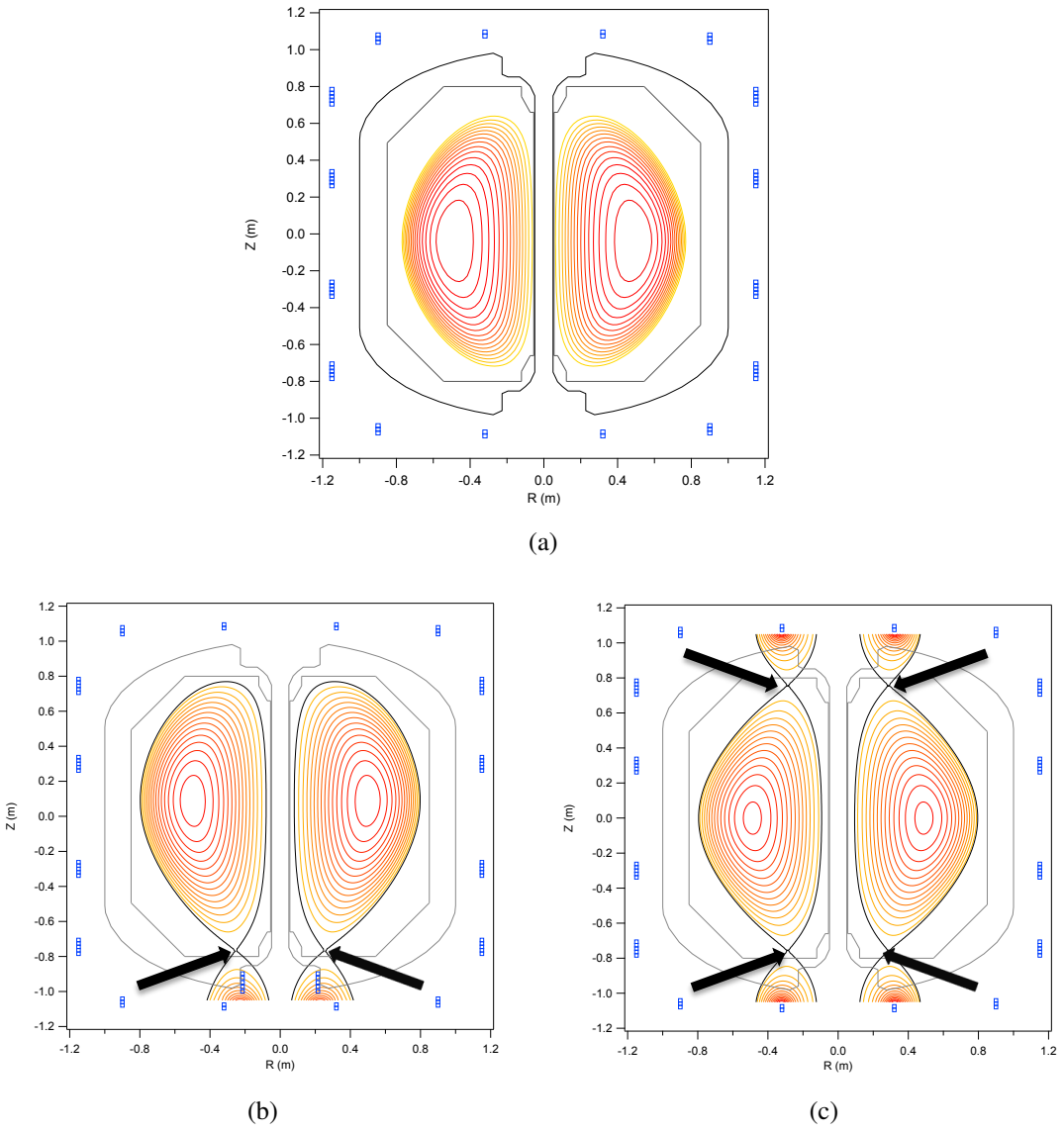

(a)

(b)

(c)

Figure 1.4: Different magnetic confinement geometries on Pegasus. (a): Limited configuration — inner wall; (b): Single null diverted configuration — lower single null plasma with one X-point; (c): Double null configuration — two X-points. The X-points are denoted by the arrows

the toroidal field allows for lower overall toroidal fields in STs, since their q_Ψ is increased over higher aspect ratio device's q_Ψ for a given toroidal field.

The high natural shaping of ST plasmas is advantageous in that high elongation leads to increased plasma current, as demonstrated by $I_p \sim \frac{1+\kappa^2}{2}$ for a given q_Ψ. Equilibrium studies have shown that STs are naturally elongated when compared with large aspect ratio tokamaks and thus less susceptible to vertical instabilities.

Another consequence of the ST geometry is that the arc length of the magnetic field line near the plasma boundary is significantly longer on the inboard side, high-field-side (HFS), near the central column than on the outboard, low-field-side (LFS), as demonstrated by Fig. 1.6 [19, Fig. 1.6]. These spatial regions correspond to locations with favorable and unfavorable magnetic curvature, respectively. Thus, on average this geometry enhances the STs resilience to magnetohydrodynamics (MHD) instabilities over conventional tokamaks. These field lines also make the ST have a strong on-axis paramagnetism in the low β_p operating regime [18].

Early numerical simulations projected MHD-stable equilibrium configurations with β_t values exceeding 20% at $A \lesssim 2$. To date, $\beta_t \sim 40\%$ has been achieved on the spherical tokamaks, START and NSTX, with β_N values of 5.9 and 7.2, respectively [20, 21].

The ultra-low aspect ratio torus (ULART) is an extreme in the ST parameter space. The conventional definition of an ULART is $A < 1.3$. The Pegasus Toroidal Experiment at $A \lesssim 1.2$ is a unique ULART in that it has the capability and flexibility to study AT relevant physics: non-solenoidal startup, high β_t operations, and the H-mode operating regime. In contrast, most ULARTs have had very low plasma current and temperature [18, 22].

1.3 H-mode Operating Regime

The high-confinement (H-mode) operating regime is a widely used confinement regime in current-day tokamaks. It is the planned operating of future burning tokamak reactors. This includes the international ITER tokamak, which will demonstrate energy out > energy in, a critical step to fusion energy production. ITER is scheduled to come online in the upcoming decade. Thus, elucidating the underlying physics behind H-mode and its instability, edge localized modes (ELMs), is critical to future projections of plasma performance and ultimately the viability of a

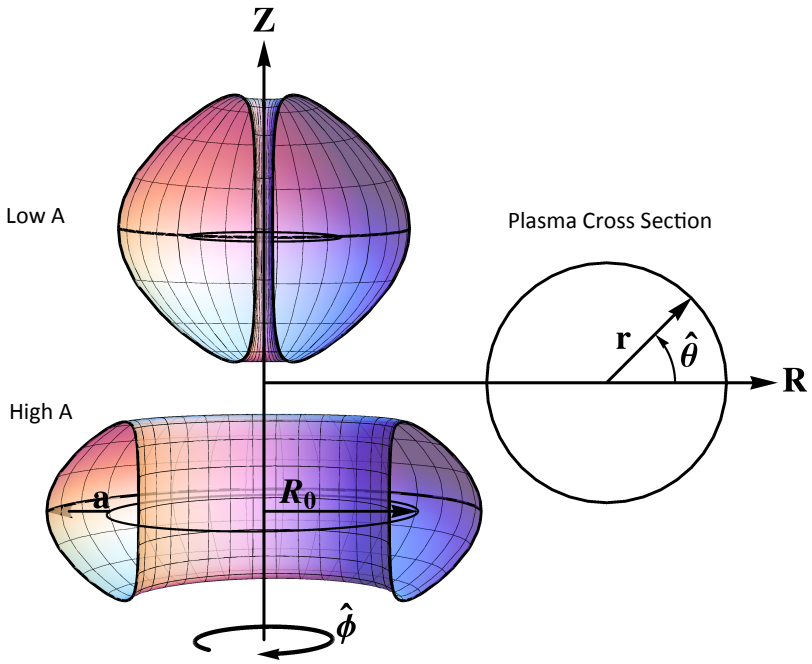

Figure 1.5: Comparison of equal-volume low aspect ratio (top left) and high aspect ratio (bottom left) tokamaks. On the right is a poloidal plasma cross-section demonstrating the relevant directions in a tokamak

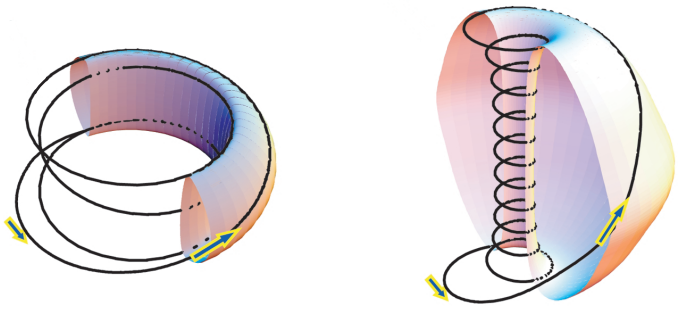

Figure 1.6: Field line windings of a conventional large aspect ratio tokamak with $q_\psi = 4$ (on left) and a ST with $q_\psi = 12$ (on right)

fusion reactor. Since its discovery, this equilibrium and stability properties of these plasmas have been extensively documented.

Much of this documentation remains empirical and is based on multi-machine studies. Therefore, variations in experimental parameters in the H-mode confinement regime provide critical contributions to testing theories of its behavior and validating ELM mitigation techniques. In particular, varying the toroidal aspect ratio A drastically changes the features of H-mode access, equilibrium, and stability. Reducing A from $\sim 3-5$ for conventional advanced tokamaks (ATs) to < 2 for spherical tokamaks results in increased shear, strong natural elongation, increased shaping of the plasma cross-section and up to a 10-fold reduction in the toroidal field required to stabilize a given plasma current channel. This can have a positive impact on the equilibrium and stability properties of the plasma by enabling operation at a very high plasma pressure, but it can also increase the net instability drive in the critical plasma edge region.

Comparing and contrasting the properties of H-mode plasmas in ATs and STs can thereby assist in the development of a first-principles H-mode physics model. Previously, H-mode studies have been conducted at $A > 1.3$ with some aspect ratio differences in H-mode behavior observed in the L-H power threshold and ELM characteristics. Recently, the Pegasus Toroidal Experiment at $A \lesssim 1.2$ entered the H-mode confinement regime for the first time. By operating at this near-unity aspect ratio, more striking differences in H-mode operations should become apparent that confirm trends observed at higher aspect ratio. This thesis seeks to begin this documentation of the H-mode operating regime at $A \sim 1.2$.

1.4 Outline of Dissertation

This dissertation is organized as follows:

- In Chapter 2, the present knowledge of the H-mode operating regime and the edge localized mode instability is discussed. The goals of this work are also presented.

- In Chapter 3, the experimental capabilities used to investigate the posed goals are described in detail.

- In Chapter 4, the experimental results are chronicled. This dissertation focuses on the first exploration of the H-mode operating regime at near-unity aspect ratio.
- In Chapter 5, the findings of this research are summarized and future research directions are suggested.

Chapter 2

Theory and Previous Work

This chapter discusses the present experimental and theoretical knowledge of the H-mode operating regime and the edge localized mode instability. It provides the framework for the dissertation goals addressed in this thesis, which are presented at the end of this chapter.

2.1 H-mode

Low confinement (L-mode) is the baseline operational regime of all tokamak magnetic fusion experiments. It is characterized by linear density and temperature profiles and relatively high levels of microturbulence, which enhance radial transport perpendicular to the magnetic field lines [11, 23]. In L-mode with the application of auxiliary heating, the confinement is found to continuously degrade as the power is increased [9]. L-mode in not seen as a viable operating regime for a fusion reactor. Thus, after the documentation of its poor performance in the 1970s, the prospects of nuclear fusion energy in a tokamak was bleak. However, in 1982 another tokamak plasma operating regime was discovered on the ASDEX tokamak in Germany [24].

In that new regime, called H-mode, a significant improvement (factor of 2) in energy and particle confinement compared to L-mode was observed [11]. The effect of auxiliary heating on confinement was weaker in H-mode than in L-mode and this regime was determined to be robust and reactor compatible [25]. The highest fusion power output occurred in an H-mode plasma [26]. Thus, H-mode is the planned operating regime for ITER and future fusion reactors.

A tokamak discharge will typically begin as an ubiquitous L-mode plasma and then spontaneously transition to a H-mode plasma, if a critical heating power $P_H > P_{LH}$ (power threshold)

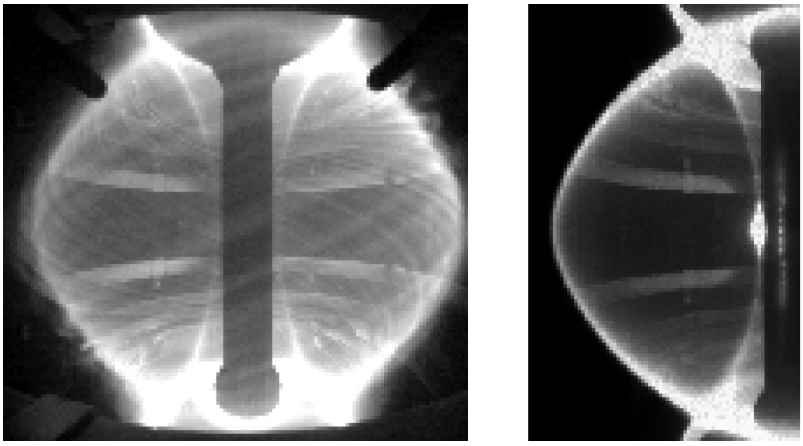

(a) (b)

Figure 2.1: MAST fast camera images of L-mode (a) and H-mode (b) plasmas

is provided [26]. H-mode has been attained in numerous tokamaks, in both diverted (double and single null geometries) and limited configurations [1, 25].

H-mode has several uniform characteristics seen across tokamaks; they are discussed here. An image comparison of L-mode and H-mode plasmas in the MAST tokamak is shown in Fig. 2.1 [27, Fig. 2.1]. The L-mode plasma has a noisy and turbulent edge, whereas the H-mode plasma has a sharp quiescent edge.

A parameter comparison of L-mode and H-mode discharges in ASDEX is shown in Fig. 2.2 [24, Fig. 2.2] on the left and right side, respectively. The only difference in the externally controlled parameters between these two discharges is an increase in the neutral beam injected power from 1.6 MW in the L-mode plasma to 1.9 MW in the H-mode plasma. The dashed line in the H-mode discharge represents the time at which the L-H transition occurs. The figure includes for these two discharges: line-integrated density [Fig. 2.2(a)], external gas puff [Fig. 2.2(b)], atom flux (D_α signal) reflected from the divertor neutralizer plate [Fig. 2.2(c)], central electron temperature [Fig. 2.2(d)], and beta poloidal and neutral beam injection phase (hatched region) in [Fig. 2.2(e)]. Many key H-mode characteristics are demonstrated by this figure, such as: the increase in density in H-mode after the transition in [Fig. 2.2(a)]; the improved particle confinement in [Fig. 2.2(b)], represented by the reduction in the external gas fueling while the electron density increased; the sudden drop in the D_α level at the time of the transition in [Fig. 2.2(c)]; the presence of ELMs in

[Fig. 2.2(c)] indicated by the sharp spikes in the D_α signal; and the improvement in the energy confinement represented by the central temperature increase in [Fig. 2.2(d)] and the increase in the beta poloidal in [Fig. 2.2(e)][24].

H-mode is characterized by a steep edge gradient in the density and temperature profiles (and thus pressure profile), as shown in Fig. 2.3 [11, Fig 2.3], where rho is the normalized minor radius (r/a). These profiles are from a DIII-D discharge with an L-phase and an H-phase. The L-mode profiles are linear, whereas in the H-phase the profiles are characterized by a steep gradient in the edge.

The change in the profiles between these two regimes is due to the formation of a steep H-mode edge gradient, called an edge transport barrier. At the transition from L-mode to H-mode, an edge transport barrier forms and allows the thermal confinement in the core plasma to improve by keeping the energy and particles in the plasma [28]. This improvement in confinement is illustrated in Fig. 2.3 by the increase in the H-mode profile values over the L-mode values.

The edge pressure always increase after the H-mode transition. However, whether the density or temperature increases depends upon the recycling conditions [29].

H-mode plasmas have a considerable drop in turbulence and radial transport levels as compared to L-mode levels [11]. An example of this turbulence reduction is demonstrated by Fig. 2.4 [30, Fig. 2.4]. In this figure, the density fluctuations are measured using a reflectometry diagnostic on DIII-D at different spatial channels with different critical densities. The dashed line represents the L-H transition. For all channels, the turbulence level is reduced in the H-phase compared to the L-phase.

It is believed that the formation of the pedestal is caused by the reduction in turbulent cross field transport inside the edge transport barrier. This reduction is believed to be caused by a sheared $E \times B$ flow in the pedestal, which reduces radial transport [31].

Related to this, another typical characteristic of the L-H transition is the formation of a strong gradient in the radial electric field, E_r, just inside the pedestal, as shown in Fig. 2.5(a) for the same discharge as in Fig. 2.3 [11, Fig. 2.5a]. The L-mode E_r is near-zero, whereas the H-mode plasma has a sharp E_r well in the edge. The poloidal and toroidal rotation contribute to the net radial electric field, so they are commonly measured as well. An example of the change in the

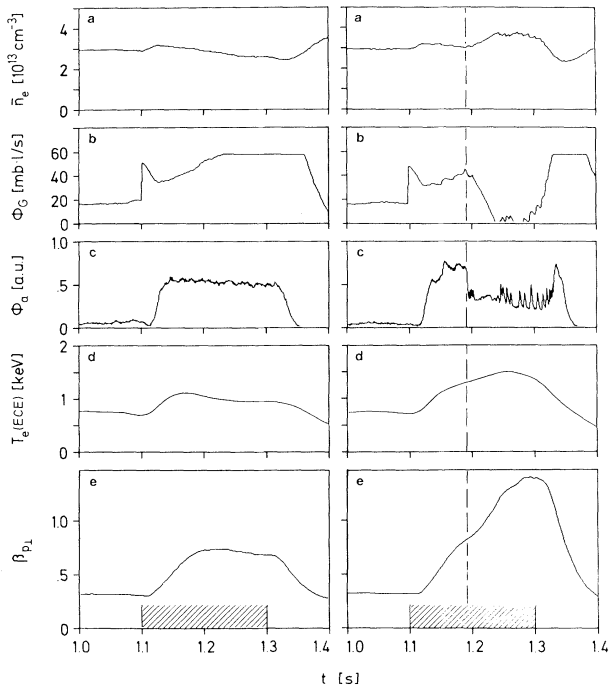

Figure 2.2: L-mode (on left) and H-mode discharge parameters (on right) on ASDEX including: line-integrated density (a), external gas puff (b), atom flux (D_α signal) reflected from the divertor neutralizer plate (c), central electron temperature (d), and beta poloidal and neutral beam injection phase (hatched region) in (e)

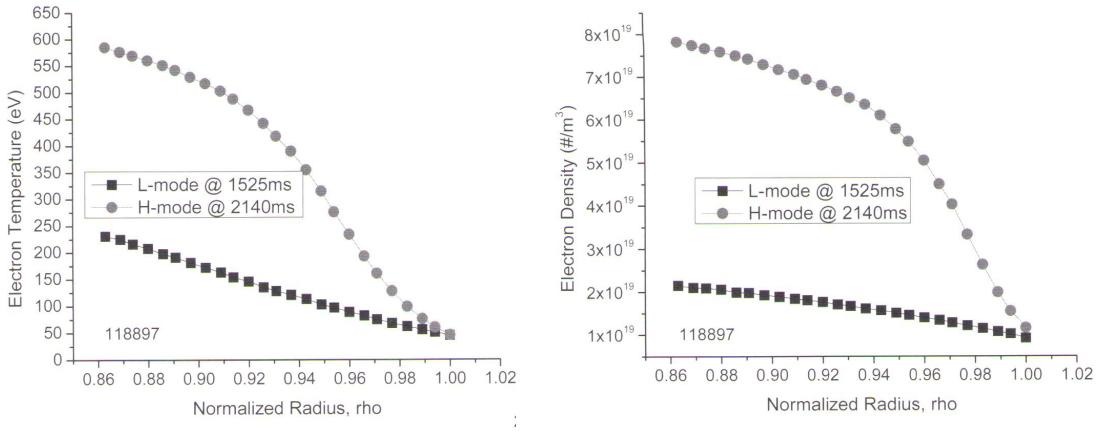

Figure 2.3: L-mode (black squares) and H-mode (grey circles) edge temperature (on left) and density (on right) radial profiles in DIII-D

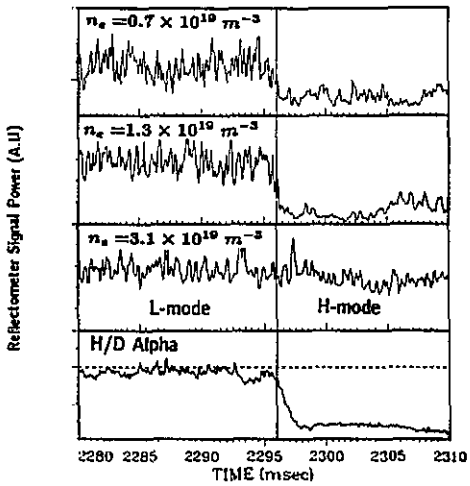

Figure 2.4: Measurement of density fluctuations before and after a H-mode transition on DIII-D using reflectometry for various spatial channels

poloidal rotation between L-mode and H-mode is shown for the same discharge as in Fig. 2.3 in Fig. 2.5(b) [11, Fig. 2.5b]. This figure shows the change in the carbon poloidal rotation from L-mode to H-mode on DIII-D. In L-mode, the rotation increases from the core to the edge, but in H-mode there is a formation of an edge well in the poloidal rotation.

Measurement of toroidal rotation can be complicated, since most tokamaks inject external momentum via beams. However, measurement of intrinsic rotation (without an external momentum input) is possible in some devices. An example of the change in the toroidal rotation between L-mode and H-mode Ohmic NSTX plasmas is shown in Fig. 2.5(c) [32, Fig. 2.5c]. This figure demonstrates that intrinsic rotation is often observed to be increased in H-mode plasmas compared to L-mode plasmas. Understanding intrinsic toroidal rotation is important, since ITER will intrinsically rotate. Also rotation can affect instabilities on the microscopic and macroscopic level [32].

Thus, there are many critical observations that indicate a L-H transition, such as: sharpening of the plasma edge; increase in density without an increase in fueling (and in some cases a decrease); improvement in particle confinement; sharp drop in D_α signal; presence of ELMs; improvement in energy confinement; formation of a pressure pedestal and an edge transport barrier; reduction

in turbulence levels; gradient in radial electric field; and observation of change in poloidal and/or toroidal rotation.

Verifying H-mode plasmas at near-unity aspect ratio have similar characteristics as those observed at higher aspect ratio is the first step in commencing H-mode studies at this aspect ratio.

2.1.1 Power Threshold

The H-mode state is achieved when a heating power above a certain threshold, P_{LH}, is applied to the plasma. This power can be provided by: heating with neutral beam injection, electron cyclotron heating, ion cyclotron heating, lower hybrid heating, and Ohmic heating. The H-mode can also be achieved by biasing the plasma using an external electrode or by biasing a limiter [25].

Understanding the physics behind the L-H transition and the ability to predict the power threshold is important for future fusion reactors and ITER. Most experimental evidence supports the theory that the sheared electric field suppresses turbulence, allowing the transition. However, the underlying mechanism than generates the radial electric field and triggers the L-H transition is unknown [9]. While the transition is still under investigation due to its complexity and occurrence in the small edge region, theoretical modeling is underway to capture these dependencies and explain the L-H physical processes.

Many L-H transition theories [33] exist. In the predator-prey model, the transition is predicted to depend on the relationship of the edge turbulence (prey) and the $E \times B$ flow shear (predator). In this framework, turbulence is driven by increased heat flux across the plasma edge. These increased turbulence levels nonlinearly drive the flow shear through Reynolds stress. When this drive becomes dominate, the turbulence will then be suppressed [34]. While many models show some agreement with experiments, only a recent mathematical model provides a testable P_{LH} formula. This model [3] shows promising comparisons with experiments and is discussed later in this section.

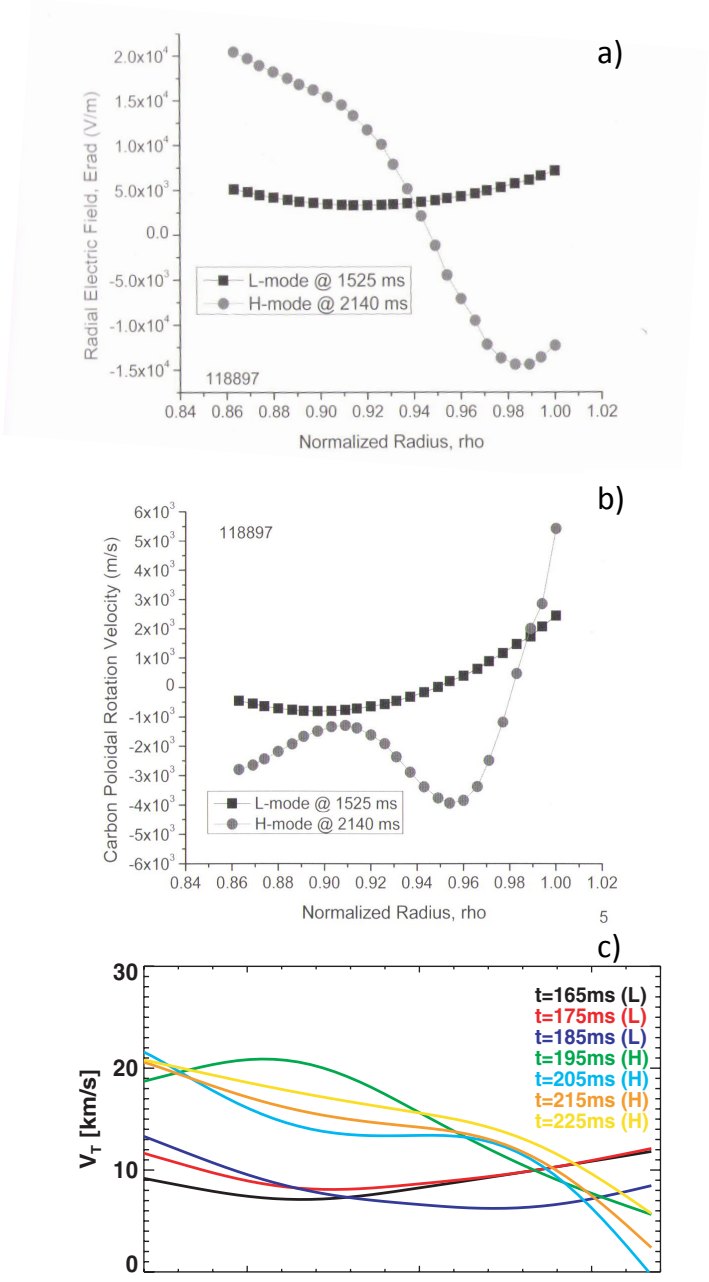

Figure 2.5: E_r and poloidal and toroidal velocities between L-mode and H-mode plasmas (a): Measured radial electric field in the edge of DIII-D L-mode and H-mode plasmas, (b): Measured carbon poloidal rotation in DIII-D edge of L-mode and H-mode plasmas, (c): Intrinsic toroidal rotation in Ohmic NSTX L-mode and H-mode plasmas

In lieu of an accepted theoretical or mathematical prediction of the L-H threshold power, inter-tokamak empirical scalings are used instead. Many parameters are known to influence the transition. However, there are a few critical parameters that universally quantitatively affect the transition: plasma electron density, magnetic field, plasma size, geometry and working gas. These dependencies are represented in the most recent scaling:

$$P_{LH\_ITPA08} = 0.0488\, n_{20}^{0.717}\, B_T^{0.803}\, S^{0.941}, \tag{2.1}$$

where P_{LH_ITPA08} is the power predicted to induce an L-H transition in MW, B_T is the vacuum toroidal field at the magnetic axis in T, n_{20} is the line-averaged density in $10^{20}\, m^{-3}$, and S is the plasma boundary surface area given by [35]:

$$S = 4\pi^2 aR\sqrt{\frac{1+\kappa^2}{2}} \tag{2.2}$$

in m^2. The data used to construct this scaling is constrained to only include deuterium single null diverted plasmas in the favorable ion ∇B drift direction, where this $\overrightarrow{B} \times \nabla B$ ion drift points towards the X-point. The scaling is derived from the International Tokamak Physics Activity (ITPA) threshold database, which includes data from Alcator C-Mod, ASDEX, ASDEX-U, CHS, COMPASS-D, DIII-D, JET, JFT-2M, JT-60U, MAST, NSTX, PBXM, TCV, and TUMAN-3M [2]. However, only data from C-Mod, ASDEX-U, DIII-D, JET, JFT-2M, and JT-60U tokamaks is used to construct the ITPA08 scaling. Figure 2.6 [2, Fig. 2.6] compares the experimental power threshold on many of these tokamaks with the L-H power requirements predicted by this scaling. As seen in the figure, the ITPA08 scaling accurately describes the power threshold for many high-A tokamaks.

The ITPA08 scaling is currently used to predict and understand current confinement devices' power threshold requirements. However, its main purpose is to predict the power threshold for ITER. When ITER first goes into operation, it will have ~ 73 MW of power available. Based on the ITPA08 scaling, to access H-mode at half of its nominal density and at its nominal density, it will require ~ 52 MW and ~ 86 MW of power, respectively. Thus, it will probably not have enough power initially to access H-mode at higher density. The 95% confidence band for the lower density is $28-96$ MW. So ITER might not have enough power to access H-mode at half of

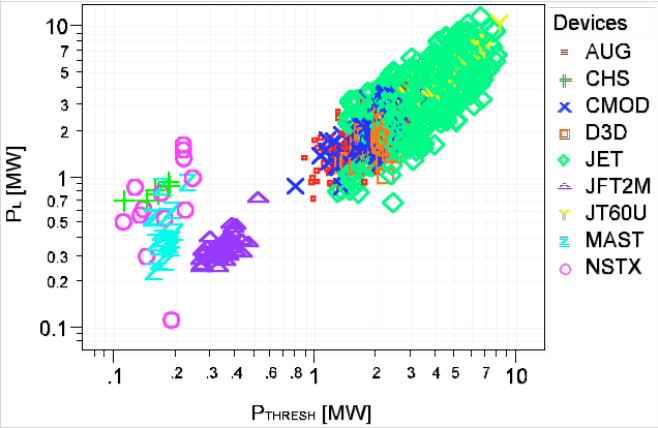

Figure 2.6: Experimental P_{LH} compared to P_{LH_ITPA08} predictions for various tokamaks

its nominal density. More accurately estimating the power threshold with empirical scalings is a critical issue for ITER [2].

The wide confidence band in the power threshold predictions for ITER is due to the high root-mean-square error of Equation 2.1. The error is quite large at 30.8%. This could partly be attributed to the observed experimental scatter in the P_{LH}. For example on ASDEX-U, the threshold had a residual scattering of 10% with an identical discharge on a day-to-day basis (the influence of recycling/wall conditions was removed from the study [9]).

The dependence of field and surface area on the power threshold is well-described by the ITPA08 scaling. While the dependence of density, geometry, and working gas on P_{LH} is informed by the ITPA08 scaling, their dependencies are still being fully explored. It has been observed experimentally that P_{LH}, instead of increasing almost linearly with density, has a U-shaped non-monotonic dependence on density.

This feature has been observed on Alcator C-Mod, ASDEX-U and JET [36]. An example of this behavior on Alcator C-Mod is shown in Fig. 2.7 [36, Fig. 2.7]. This figure provides the threshold power on Alcator C-Mod versus density for various magnetic fields and plasma currents. It is apparent from this graph that there is a certain density, n_e^{min}, where a minimum in the power threshold is observed. As the density deviates from n_e^{min}, the power required to access H-mode increases. At densities above n_e^{min}, a similar density dependence as in the P_{LH_ITPA08} scaling is recovered. This figure also illustrates that n_e^{min} required to access H-mode increases with increasing

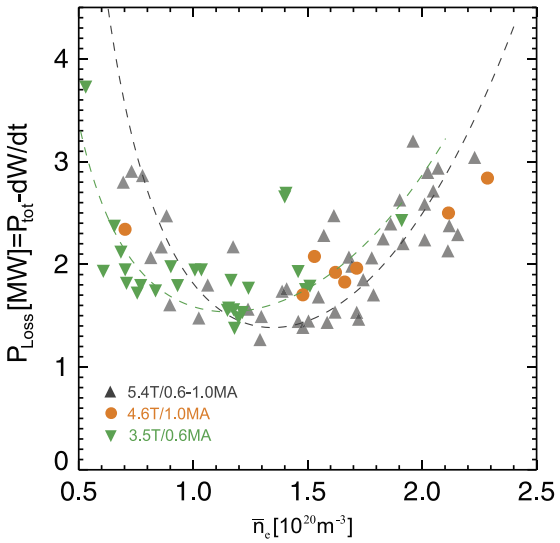

Figure 2.7: H-mode power threshold dependence on density on Alcator C-Mod at various B_T and I_p

magnetic field [36]. This observation is a point of concern for accessing H-mode in ITER when it operates at low density, since it will operate at high field [2].

Many different threshold dependencies on geometry have been observed in various tokamaks. Experiments have shown that diverted discharges have a lower threshold than limited plasmas by a factor of $1.5-3$ [37, 38]. The type of diverted discharge, single or double null, also affects the power threshold. The lowest power threshold is typically found in favorable diverted single null discharges, so this constraint is used for the ITPA scalings. On DIII-D, the threshold power increased by a factor of two when the drift direction was varied from pointing towards the null to away from the null. Usually, a double null plasma has a threshold power between the two single null discharges. However, both NSTX and MAST have determined that their threshold is lowest in the connected double null configuration (when the two X-points lie on the same flux surface [39, 40].) The diverted L-H threshold power can also vary depending on plasma shape or divertor geometry, which is thought to be caused by the influence of neutral density at the plasma boundary [9, 31].

The ITPA08 scaling is derived only from deuterium discharges. However, it is important to understand the effect of mass on the power threshold, since it is important for general tokamak

operations as well as future operations on ITER. ITER will use hydrogen and/or helium as the working gas in the non-nuclear phase and tritium in the nuclear phase [41, 42]. As discussed earlier, achieving H-mode in the early ITER operations, before full power is available at half of the nominal density in deuterium is marginal. It is not known if it will be possible to achieve H-mode in hydrogen or helium, thus the need for experimental work now. The L-H power threshold in hydrogenic gas has been observed experimentally to go as $P_{LH} \propto 1/M$, demonstrating that the $P_{LH_{Hydrogen}} > P_{LH_{Deuterium}} > P_{LH_{Tritium}}$ [43]. However, the dependence of the power threshold on helium is less clear, since different machines have observed different dependences. ASDEX-U has shown that the threshold is 30% lower for helium [42] than deuterium, but on DIII-D it is 30-50% higher in helium [41].

Although some parameters have a clear quantifiable effect on the power threshold, other characteristics of the discharge and machine are also known qualitatively to affect the L-H threshold. These parameters include: wall conditioning and recycling, gas fueling location, and aspect ratio [26, 43, 44]. It has been observed experimentally that a clean plasma, rather than a dirty one with impurities, gives a lower threshold. The density and distribution of neutrals have a strong influence on the L-H transition conditions, a reduction in recycling leads to lower threshold powers. Thus to maintain good wall conditions and lower recycling, vessel boronization and helium glow-discharge cleaning are typically used to obtain the lowest threshold powers [26, 31, 43, 44].

The location of gas fueling significantly influences the L-H threshold. COMPASS-D was the first tokamak to use HFS fueling for H-mode access. On COMPASS-D, H-mode was typically achieved after terminating the LFS gas puff. However, the use of HFS refueling allowed the transition to occur with the gas valve open at lower densities and lower threshold powers. On MAST, neither maintaining nor terminating the LFS fueling allowed routine access to H-mode. After installing a HFS fueling system, MAST was able to routinely access H-mode in both limited and diverted double null discharges without prior wall loading (deuterium deposition on the plasma facing components before the discharge.) NSTX has also found HFS fueling facilitates H-mode access at lower power thresholds. Thus, the location of gas fueling, particularly in ST tokamaks, is a important factor in facilitating H-mode access, sometimes at a lower power threshold [31].

The power threshold in low-A tokamaks has been found to be rather large when compared to the ITPA08 scaling relationship, as demonstrated by Fig. 2.6. Both MAST and NSTX do not agree well with this scaling. A study was conducted in 2004 to attempt to include the aspect ratio effect in a power threshold scaling. The power threshold formula of the time was [43]:

$$P_{LH\_ITPA02} = 0.06 n_{20}^{0.7} B_T^{0.7} S^{0.9}. \tag{2.3}$$

When comparing the required power for MAST ($A \approx 1.45$) and NSTX ($A \approx 1.32$) with the predictions from this formula, MAST requires 1.6 more power than this scaling and NSTX requires 3.7 times more. Based on data from STs and ATs, a new scaling was derived [43]:

$$P_{LH\_ITPA04} = 0.072 \mid B \mid_{out}^{0.7} n_{20}^{0.7} S^{0.9} \left(\frac{Z_{eff}}{2}\right)^{0.7} F(A)^{\gamma}, \tag{2.4}$$

where $\mid B \mid_{out} = \left(B_{tout}^2 + B_{pout}^2\right)^{0.5}$, $B_{tout} = B_T \frac{A}{A+1}$, $B_{pout} = \frac{\mu_0 I_p}{2\pi a}(1+\varepsilon)$,

$$F(A) = \frac{0.1A}{1 - \left(\frac{2}{1+A}\right)^{0.5}}, \tag{2.5}$$

and $\gamma = 0.5 \pm 0.5$. The scaling was based on the assumption that the difference in the power threshold at low-A was due to the trapped particle fraction. The trapped particle fraction is higher at low aspect ratio. This scaling better matched NSTX and MAST data with a factor of 1 and 2 agreement with their respective experimental power thresholds. However, it still needs to be verified due to the high variability of γ and limited data at low-A. Thus, more experimental data at low-A is required to accurately understand the power threshold's dependence on aspect ratio [43].

While empirical power threshold scalings exist and offer some insights into the underlying physics behind the transition, these conflicting results clearly demonstrate its insufficiency. The ITPA08 power threshold scaling adequately describes the dependence on toroidal field and surface area. It does not demonstrate the actual density dependence seen, but rather only the dependence above n_e^{min}. The data used for the scaling is limited to only include data from the deuterium discharges in the favorable single null direction. Many other factors are known to influence the transition and are ignored by this scaling. In particular, the effect of aspect ratio is discounted and often removed from data. Thus, the usage of empirical scalings, such as the ITPA08 scaling, is

very limited. The need for a theoretical model and more experimental data, particularly at low aspect ratio, is clear.

2.1.1.1 FM^3 Mathematical Model for the L-H Power Threshold

The FM^3 model [3] is the first testable power threshold expression provided by a theory or mathematical model. The model agrees well with the ITPA08 power threshold scaling. Two experimental P_{LH} results are possibly explained by the model: 1) prediction of the location of n_e^{min} and 2) the dependence of geometry (limiter/divertor) on the power threshold.

The FM^3 mathematical model postulates that the H-mode transition occurs when the plasma turbulence competes with shear Alfvén waves near the last closed flux surface at a position r_*. This assumption derives from the widespread acceptance that drift-Alfvén wave turbulence driven by radial pressure gradients is the dominant radial transport channel in L-mode edge plasmas. It has been observed experimentally that there is a strong coupling of the two waves (drift and Alfvén), when their characteristic times become comparable. The FM^3 authors postulated that when this happens a new channel becomes available and an inverse energy cascade occurs. This inverse energy cascade leads to the formation of zonal flows, which then follow a standard paradigm of zonal flow–drift-wave interaction. The paradigm is that the zonal flows are generated by the drift-wave nonlinearity. Then zonal flows react back on the turbulent flow by tilting the turbulent eddies, reducing their perpendicular transport but not their poloidal correlation length. This paradigm is similar to some experimental observations of the relationship between turbulence and zonal flows in triggering the L-H transition.

Using this initial assumption of the transition occurring when the edge parallel Alfvénic time is comparable to the perpendicular transport time, a criterion for the L-H transition is:

$$Wa_{L-H} = \frac{\tau_{\parallel}^{A}}{\tau_{\perp}^{Q}} \sim 1, \tag{2.6}$$

where Wa_{L-H} is the Wagner number at L-H transition and $\tau_{\parallel}^{A}(r_*)$ is the Alfvénic time at the radial location (r_*) of the transition as expressed by:

$$\tau_{\parallel}^{A} = \frac{L_{\parallel}(r_*)}{V_A(r_*)}. \tag{2.7}$$

$L_{\parallel}$ is the parallel connection length defined as $L_{\parallel} \approx \pi q R$ and V_A is the Alfvénic velocity. $\tau_{\perp}^{Q}$ is the perpendicular electron energy transport time at (r_*) over a radial correlation length of a turbulent eddy and given by:

$$\tau_{\perp}^{Q} = \frac{L_{\perp}^{corr}(r_*)}{V_{\perp}^{Q}(r_*)}. \tag{2.8}$$

$L_{\perp}(r_*)$ is the radial correlation length and $L_{\perp}(r_*) \approx \sqrt{L_p \rho_s}$, where L_p is the mean pressure gradient length in the edge region, ρ_s is the plasma sound speed, and $V_{\perp}^{Q}$ is the radial velocity of electron energy transport. L_p is proposed to scale as $L_p \propto a q_* A^{-1/2} \propto R\varepsilon q_{cyl}^{1/2} A^{-1/2}$ where R is the major radius, ε is the inverse aspect ratio, A is the ion mass, and q_* is the safety factor at the radial location at the L-H transition and q_* is assumed to depend on q_{cyl} by $q_* \propto \sqrt{q}_{cyl}$. q_* is assumed to scale with a square-root dependence of the plasma current due to the presence of the stochastic layer.

Substituting in

$$V_{\perp}^{Q} = \frac{P_{\perp}}{\left[\frac{1}{2} S_{\perp} \times \frac{3}{2} p_e\right]}, \tag{2.9}$$

where $P_{\perp}$ is the power crossing the flux surface, $S_{\perp}$ is the surface area of that flux surface defined here to be equal to $S_{\perp} \approx 4\pi^2 R^2 \varepsilon \sqrt{\kappa}$, and p_e is the electron pressure, and then solving for $P_{\perp}$ gives:

$$P_{LH} \approx \frac{3}{4} p_{e_*} S_{\perp} V_{A_*} L_{\perp}^{corr*} / L_{\parallel}^{*}. \tag{2.10}$$

Variables denoted with a * are defined to occur at the radial location of the L-H transition.
Substituting in the approximations above, P_{LH} is shown to be proportional to:

$$P_{LH} \propto \left(n_{e*} B_T \kappa / q_*\right)^{\frac{1}{2}} (R\varepsilon)^{\frac{3}{2}} Z^{\frac{1}{4}} A^{-\frac{1}{2}} T_{e*}^{\frac{5}{4}}, \tag{2.11}$$

where Z is the ion charge.

The two-point model of scrape-off-layer (SOL) transport [45] is then invoked to determine T_{e^*}, which gives:

$$T_{e*} \approx \left[\left(\frac{P_{LH}}{S_{\|} \gamma \zeta n_{e*}} \right)^{\frac{7}{3}} + \frac{7}{4} \frac{P_{LH} L_{\|}^{SOL}}{\kappa_{0e} S_{\|}} \right]^{\frac{2}{7}}, \tag{2.12}$$

where $S_{\|}$ is the cross-sectional surface area, γ is the total sheath energy transmission coefficient, $\zeta = \sqrt{Z/(Am_p)}$ where m_p is the proton mass, $L_{\|}^{SOL}$ is the SOL parallel connection length, and κ_{0e} is the Spitzer-Harm conductivity. The two separate terms in Equation 2.12 represent two distinct regions of SOL transport. The left term dominates in the sheath limited regime and the right in the conduction limited regime. The transition between these two regimes occurs at a critical value of the SOL collisionality, ν_{SOL}. This transition occurs at $\nu_{SOL} \sim 15$, with the conduction limited regime occurring at $\nu_{SOL} >> 15$ and the sheath limited regime at $\nu_{SOL} << 15$.

Substituting in the left term of Equation 2.12 into Equation 2.11, for the conduction limited regime gives:

$$P_{LH} \propto (n_{e*} B_T)^{\frac{7}{9}} (S_{\perp} \varepsilon)^{\frac{8}{9}} \kappa^{\frac{1}{18}} A^{-\frac{1}{2}} Z^{\frac{2}{3}} q_*^{-\frac{7}{9}} q_{SOL}^{\frac{5}{9}} \nu_{SOL}^{-\frac{5}{9}}. \tag{2.13}$$

And substituting in the right term of Equation 2.12 into Equation 2.11, for the sheath limited regime gives:

$$P_{LH} \propto n_{e*}^{-2} B_T^3 S_{\perp}^{-\frac{1}{2}} \varepsilon^{\frac{9}{2}} \kappa^{\frac{3}{4}} A^2 Z^{-\frac{9}{4}} q_*^{-\frac{3}{2}} \nu_{SOL}^{-5}. \tag{2.14}$$

Equation 2.13 represents the high density asymptotic scaling and is in general agreement with the ITPA08 scaling, as demonstrated by Fig. 2.8 [3, Fig. 2.8]. In the left figure, the experimental power threshold is compared against the power threshold predicted by the ITPA08 scaling. On the right, the experimental power threshold is compared against the threshold predicted by the FM^3 conduction equation. Relative agreement between the two figures is observed. Equation 2.14 represents the low density asymptotic scaling.

At the intersection of the two asymptotic scalings in density space, a minimum in P_{LH} is found. FM^3 predicts this critical density by inserting Equation 2.12 into Equation 2.11 and differentiating with respect to density. The critical density predicted by the FM^3 model roughly agrees with JET [3] and C-Mod's [46] experimental observations of their P_{LH} minimum in density space.

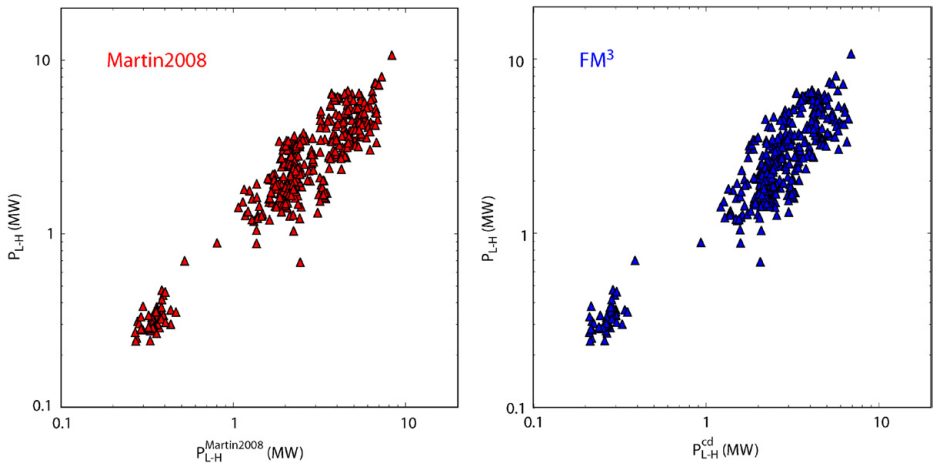

Figure 2.8: Experimental P_{LH} compared to ITPA08 (on left) and FM^{3}conduction (on right) scalings for various high-A tokamaks

Another approach that can be taken to determine this critical density is solving for the density at which the collisionality is approximately 15, as shown here:

$$\nu_{SOL} = L_{\parallel}^{SOL}/\lambda_{ei} = 15, \tag{2.15}$$

where $L_{\parallel}^{SOL}$ is the SOL parallel connection length and λ_{ei} is the collisional mean free path. By substituting in $\lambda_{ei} = 8.5x10^{15}\,(T_e^*)^2\,/n_e^*$ [4], Equation 2.15 becomes:

$$\nu_{SOL} = \frac{3.7\times10^{-16} R q_* n_*}{(T_{e*})^2} = 15. \tag{2.16}$$

Thus the critical density, n_*, in units of $10^{19}\,m^{-3}$ is:

$$n_* = \frac{4.06\times10^{-3}\,(T_{e*})^2}{R q_*}. \tag{2.17}$$

Using Equation 2.13, FM^3 predicts that the difference in P_{LH} between limited and diverted configurations is due to the edge safety factor and that:

$$P_{LH}^{LIM}/P_{LH}^{DIV} \approx \left(q_*^{LIM}/q_*^{DIV}\right)^{-\frac{7}{9}}. \tag{2.18}$$

At high-A, generally $q_*^{DIV} > q_*^{LIM}$, which is consistent with the higher observed P_{LH} in limited plasmas compared to diverted plasmas.

The L-H power threshold has many observed behaviors with machine parameters, but no single underlying theory to explain these dependencies. Thus, collecting more experimental data, particularly where data is sparse, will be helpful in developing an underlying physics model of the L-H transition. The power threshold at low-A is observed to be higher than expected on NSTX and MAST, with no accepted explanation. Exploring the power threshold at even lower aspect ratio should provide some insight into the threshold physics. Comparing experimental data with modeling, such as the FM^{3}model, will also help improve our understanding of the L-H power threshold.

2.1.2 Edge Localized Modes

In the H-mode edge transport barrier, strong pressure and current gradients are formed. These gradients contain substantial free energy that can drive new intermittent MHD instabilities in the edge plasma, called edge localized modes (ELMs) [47]. ELMs are transient event that eject particles and energy onto the plasma facing components. An image of an ELM on the MAST tokamak is shown in Fig. 2.9 [48, Fig. 2.9]. The image has filamentary structures associated with the ELM.

ELMs constrain the overall achieved confinement by constraining the pressure gradient, since total confinement and core transport are directly linked to the height and gradient of the temperature and pressure pedestal [49]. An example of a pressure pedestal evolution through an ELM cycle on DIII-D is shown in Fig. 2.10 from (1) just after an ELM to (8) right before an ELM. After the transition into H-mode and in-between ELM events, the pedestal height continues to increase until an ELM occurs. The ELM then reduces the pedestal height and pedestal width [50, Fig. 2.10]. This cycle of the pressure profile evolving then repeats with each ELM event.

Without ELMs, in H-mode the improved confinement leads to a continual increase in density and an accumulation of impurities. If $n_e = (0.7-0.9)\,n_G$ is achieved through the use of gas puff fueling, a H-L back transition will occur [9]. High impurity accumulations can also terminate the H-mode discharge [26]. Thus, a continual increase in density and impurities is undesirable, and these levels need to be regulated [9]. ELMs can beneficially regulate the density and impurity levels through the expulsion of edge plasma [49].

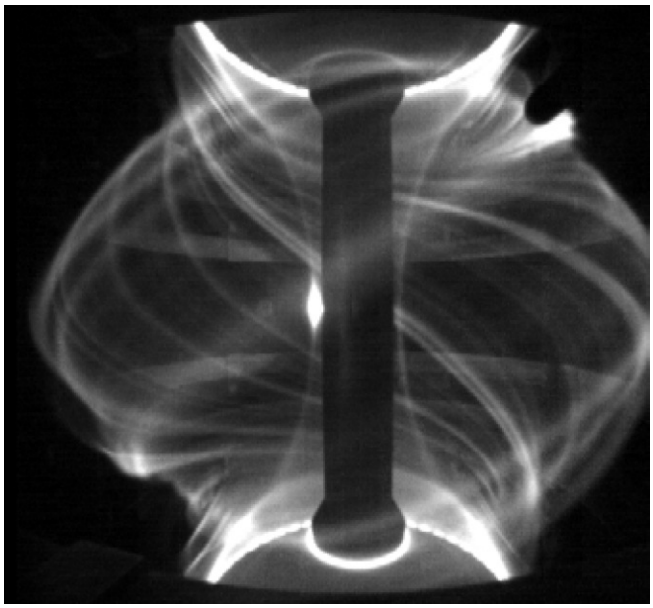

Figure 2.9: Fast camera image of an ELM on MAST

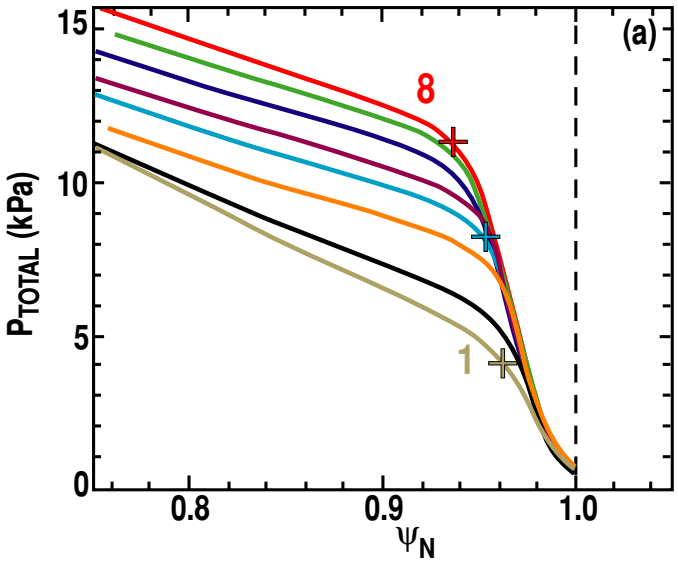

Figure 2.10: Pressure pedestal evolution on DIII-D during an ELM cycle, from just after an ELM (1) to just before the next ELM (8)

However, this violent repetitive edge plasma expulsion can lead to damaging high transient heat loads on plasma facing components. ELMs are nominally benign on current tokamaks, but they are expected to limit the lifetime of plasma facing components on next-step machines, such as ITER [48]. Thus, ELMs are beneficial and necessary in their particle regulation but detrimental in their high transient heat loads, impurity influxes, and limiting of plasma performance. Research is ongoing on ELM operating regions to create a scenario with their particle regulation but acceptable heat loads.

The pedestal height and width are linked to ELM triggering. The leading theory to explain the physical processes that limit the pedestal height and subsequently trigger ELMs is peeling-ballooning theory [51]. This model hypothesizes that ideal MHD instabilities — peeling (edge localized external kink), driven by the edge current, and ballooning modes, driven by the pressure gradient — are destabilized by the sharp pressure gradient and large bootstrap current [52, 53]. The relationship between the pressure gradient and the bootstrap current is illustrated by this equation:

$$j_{BS} \sim -q\frac{\varepsilon^{1/2}}{B_\theta}T\frac{dn}{dr}, \tag{2.19}$$

where j_{BS} is the bootstrap current, T is the temperature and $\frac{dn}{dr}$ is the derivative of the density in the radial direction [4] and also shown in Fig. 2.11 [54, Fig. 2.11]. In this figure, the strong pressure gradient in the plasma edge drives a very strong bootstrap current in the edge.

The ideal MHD instabilities driven by pressure and current gradients are strongly coupled in the ELMing region. For example, Fig. 2.12 [54, Fig. 2.12] shows the peeling-ballooning (P-B) stability diagram plot for a plasma in the edge region of a JET-like equilibrium [54]. Peeling modes are the limiting instability at high J_{ped}, low p'_{ped}, while ballooning modes are unstable at low J_{ped}, high p'_{ped}. Coupled peeling-ballooning modes are the limiting instability in the high J_{ped}, high p'_{ped} region. Exact boundaries are sensitive to the details of a particular equilibrium configuration. Plasma shape is important, since strong shaping can decouple the effect of magnetic shear generation from the presence of edge current and increase the ELM-free operating space, as shown in the figure [53].

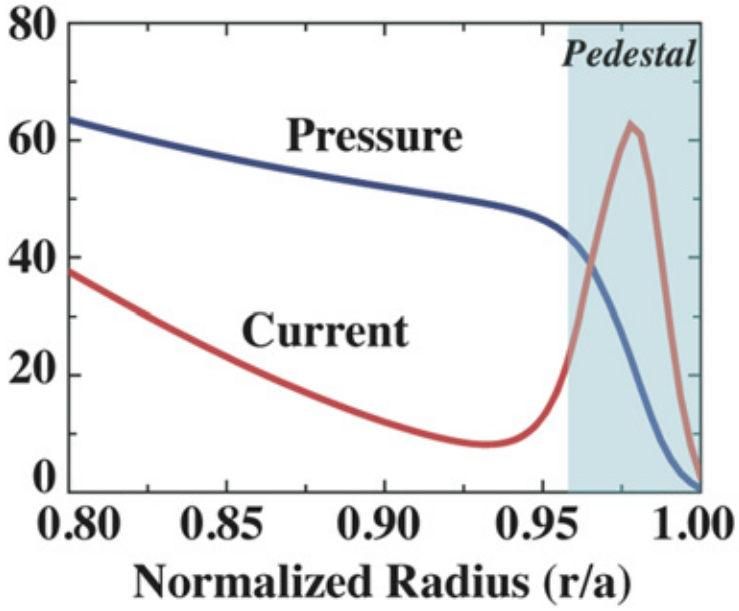

Figure 2.11: Illustration of typical edge H-mode pressure and current profiles with the edge barrier region shaded

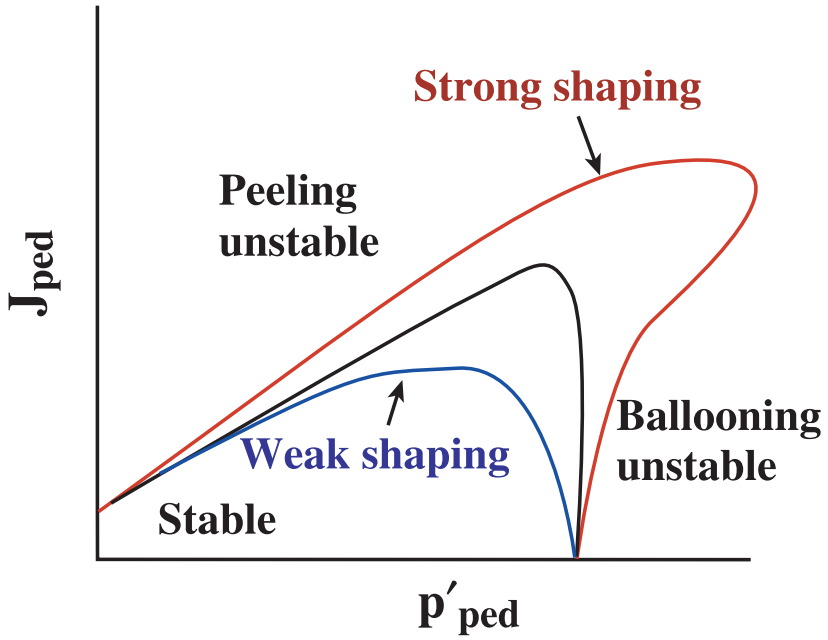

Figure 2.12: Peeling-ballooning stability space for a JET equilibrium

Experimentally these MHD modes are identified by their toroidal mode number n. Long-wavelength peeling modes have low $n \lesssim 3$, short-wavelength ballooning modes $n \gtrsim 30-50$, and intermediate-wavelength peeling-ballooning modes have $3 \lesssim n \lesssim 30-50$ [55].

While peeling-ballooning stability provides a constraint on both the pedestal height and width, it is insufficient by itself to determine these two unknowns. In the EPED model, a nearly local kinetic ballooning mode constraint (KBM) is also in conjunction with a non-local peeling-ballooning mode constraint in order to predict the pedestal height and width at which an ELM occurs. The kinetic ballooning mode drives strong turbulence in the pedestal, thus limiting the pedestal growth. The KBM provides a second constraint on the pedestal height and width, typically that the pedestal width goes as $\beta_{p,ped}^{0.5}$. Utilizing the peeling-ballooning mode stability and kinetic ballooning mode onset, the EPED model predicts the pedestal height and width. An example of this collaboration is shown in Fig. 2.13 [47, Fig. 2.13] for a DIII-D discharge. The intersection of the peeling-ballooning and kinetic ballooning mode constraints define the pedestal height and width at at which an ELM event occurs. This is in rough agreement with the experimental measurement.

A complete pedestal model is not currently available, so multi-machine empirical scalings are used. These scalings suggest different parameter dependence for the density and temperature pedestal width. For both widths, a similar dependence on machine size, poloidal magnetic field, and pedestal electron temperature, T_e, and density, n_e, was found. However, the influence of ion temperature, T_i, and toroidal magnetic field are different for the two pedestal widths. In dimensionless form, the density pedestal width was found to scale with $\rho_{i*}^{0.6}$ (normalized ion gyroradius) and the temperature pedestal width with $\beta_{p,ped}^{0.5}$ [56]. An average pedestal width can be constructed by taking the average of the density and temperature widths. This average pedestal width was found to scale differently with $\beta_{p,ped}$ at low-A and high-A, as shown in Fig. 2.14 [57, Fig. 2.14]. At high-A, on C-Mod and DIII-D, the average pedestal width was proportional to $\beta_{p,ped}^{0.5}$. Whereas at low-A on NSTX, the average width scaled with $\beta_{p,ped}^{0.9}$ [57]. The widths were found to not scale with collisionality [58].

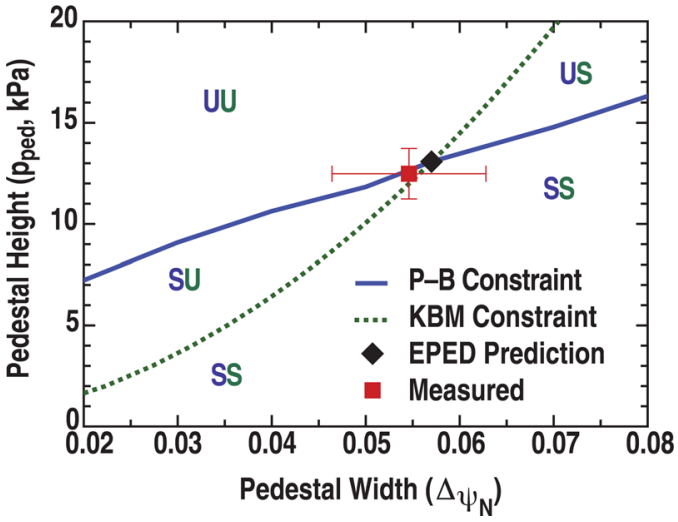

Figure 2.13: EPED model predictions of the pedestal height and width (black diamond) at which an ELM occurs, determined from the intersection of P-B (solid blue line) and KBM (dotted green line) constraints. The measured pedestal height and width, at which an ELM occurs, is represented by the red square. The different stability regions are represented by a S for stable and U for unstable and refer to P-B (first character) and KBM (second character)

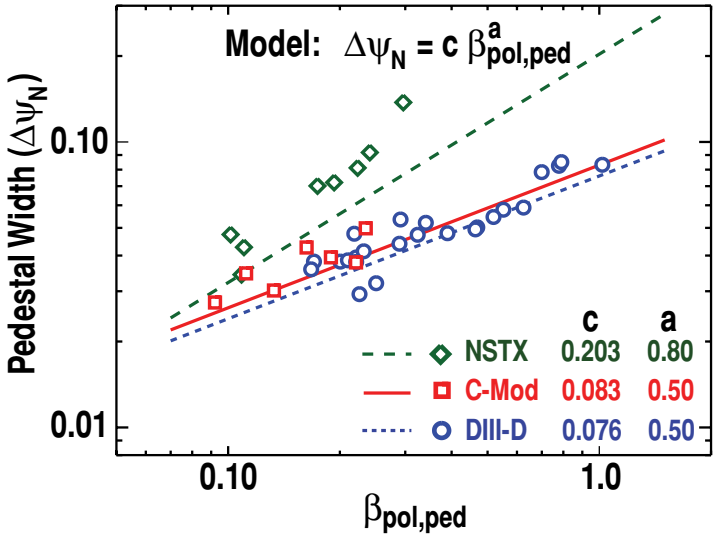

Figure 2.14: Average pressure pedestal width dependence on $\beta_{p,ped}$ on NSTX, C-Mod, and DIII-D

Nonlinear simulations, such as NIMROD, JOREK, and BOUT, are used to project ELM power deposition levels in next-step devices [59]. Their experimental validation requirements measurement of edge pressure and current profiles with high spatial and temporal resolution. While the edge pressure profile has been available through an ELM, the edge current profile has not [60].

ELMs are characterized experimentally by repetitive spikes in the D_α emission, which indicates a particle loss from the edge plasma to the plasma facing components (typically a divertor plate). The particle loss is accompanied by an energy loss with each ELM, on the order of 1 to 15% of the stored energy in the edge transport barrier [50, 59]. The ELMs cause a drop in the edge n_e and T_e pedestals over a very short time (typically of the order of 200 μs), which can extend up to as much as 20% of the plasma radius from the edge inwards. These pedestals will then build up again until the ELM cycle repeats [59].

A variety of ELM experimental categorizations exist. They are distinguished by the fractional energy loss $\Delta W_{ELM}/W$, dependence of inter-ELM frequency with input heating power, density dependence, and the presence of a magnetic precursor [9].

Type I ELMy H-mode is the most common high confinement regime in today's tokamak. It has the highest energy confinement of any regime and its τ_e is given by the IPB98(y,2) scaling, described in the following section. Due to its high performance, it is the planned operating regime for ITER [9]. These ELMs have the highest energy loss per ELM at $10-15\%$ of the pedestal energy. The damage inflicted by these ELMs on the plasma facing components is expected to be intolerable for a next-step device [61]. They typically expel approximately 4% of the particle inventory [50]. ELMs may also cause a return to L-mode, usually this behavior is associated with Type I ELMs [9, 62]. The frequency of these ELMs increases with increasing heating power. Some machines measure a magnetic precursor for Type I ELMs, while most machines do not. Toroidal mode numbers for Type I ELMs on both ATs and NSTX are intermediate-n [63, 64, 65]. Type I ELMs are generally accepted and experimentally confirmed to be triggered by intermediate-n peeling-ballooning modes [9].

Type III ELMs are another commonly seen ELM type in H-mode plasmas. Their energy confinement time is typically $10-30\%$ lower than the Type I ELM regime's energy confinement [9].

In comparison, Type III ELMs lose 1 to 5% of the pedestal plasma energy or particles and typically occur at a higher frequency than Type I ELMs. As the power is increased in the Type III ELM regime, the frequency of the ELMs decreases. These ELMs generally have magnetic precursors [50]. At high-A, it has been observed that Type III ELMs have high-n toroidal mode numbers [65]. However, on NSTX, Type III ELMs are observed to have low toroidal mode numbers, $n \leq 3$ [64]. Applying peeling-ballooning theory to Type III ELMs has determined that some Type III ELMs might be caused by the low-n peeling instability [9].

Transferring between the Type I and Type III ELM regimes can be accomplished by changing the heating power or the collisionality. Type I ELMs occur at higher heating power, $\sim 1.5 - 2 \times P_{LH}$, and Type III ELMs occur at lower heating power just over the power threshold [9]. Transferring from the Type III ELM regime to the Type I ELM regime through the variation of heating power is demonstrated in Fig. 2.15 [50, Fig. 2.15]. In this figure, Type III ELMs occur at $P_{NBI} \leq 1.4$ MW, and Type I ELMs occur at $P_{NBI} \geq 2$ MW. The Type I ELMs can be identified by their lower frequency and larger amplitude D_α spikes and their increase in ELM frequency with heating power. Whereas, Type III ELMs have a higher frequency and lower amplitude D_α spikes and a decrease in ELM frequency with heating power.

Pedestal collisionality can also be used to distinguish between the regimes with Type III ELMs typically occurring at higher density or lower temperature than Type I ELMs. This observation is demonstrated in Fig. 2.16 [1, Fig. 2.16]. L-mode plasmas occur at the lowest pedestal temperature. Type III ELMs occur at both higher pedestal temperatures and higher densities than L-mode plasmas. Type I ELMs then occur at even higher pedestal temperatures and comparable densities (but not quite as high) to Type III ELMs [50]. High density is achieved in the Type I ELMing regime by manipulating these plasmas to be more triangular and to have a peaked density profile [9]. The main properties of these two ELM types are summarized in Table 2.1

While Type I ELMy H-mode is the planned operating regime for ITER due to its high confinement, the ELM damage to the plasma facing components damage is seen as intolerable. Research

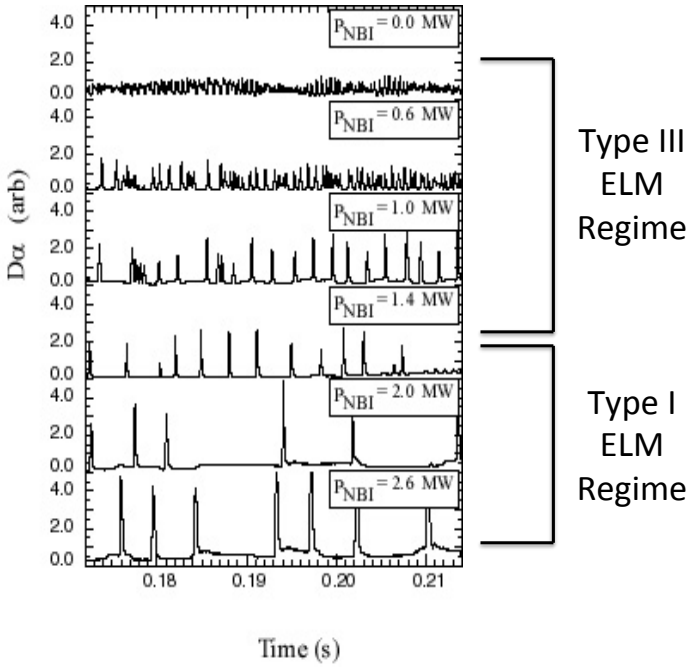

Figure 2.15: Frequency dependence of Type I and III ELMs on NBI heating power on MAST, illustrated by D_α emissions

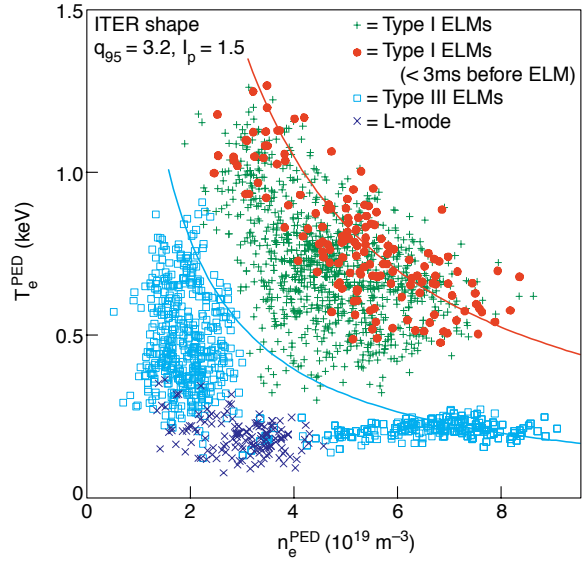

Figure 2.16: DIII-D pedestal densities and temperatures in L-mode and H-mode (Type I and Type III ELMs) plasmas

	Type I ELM	Type III ELM
Energy Confinement	$H_{98} \sim 1$	$H_{98} \sim 0.7 - 0.9$
Energy Loss per ELM	10–15% of pedestal energy	1–5% of pedestal energy
Magnetic Precursor	Not common, intermediate-n	High-A: high-n, NSTX: low-n
Access	$1.5 - 2 \times P_{LH}$, lower ν	$\sim P_{LH}$, higher ν
Frequency Dependence	Lower f, $\uparrow$ in f_{ELM} with P_{heat}	Higher f, $\downarrow$ in f_{ELM} with P_{heat}

Table 2.1: Type I and III ELMs characteristics

is being conducted to further understand Type I and Type III ELMs to find a mitigated high performance H-mode operating regime. Key to this research is the validation of nonlinear ELM simulations. However, these simulations require the measurement of the edge current profile, which has not yet been available.

Differences in ELM behavior, such as the toroidal mode number, have been observed in different aspect ratio tokamaks. By studying ELMs across a wide variety of characteristics, more insights should be learned that will help further understand ELM behavior and triggering.

2.2 Confinement Quality and Scalings

The physical processes that determine heat and particle transport in fusion-relevant plasmas are complex. Non-linear simulations have been conducted to accurately calculate the energy confinement time. However, these simulations are involved, time-intensive, and not yet fully validated by experiment [66]. Thus the description conventionally used of the global energy confinement time, τ_e, is based upon empirical scalings drawn from relevant datasets within specific operating regimes [1].

Typically, these scaling laws are given as empirical scalings of the form:

$$\tau_e = C M^{\alpha_m} I_p^{\alpha_I} R^{\alpha_R} a^{\alpha_a} \kappa^{\alpha_\kappa} n^{\alpha_n} B_T^{\alpha_B} P^{\alpha_P} \tag{2.20}$$

where τ_e is the global energy confinement time in seconds, M is the average isotopic mass number, I_p is the plasma current in MA, R is the major radius in m, a is the minor radius in m, κ is the elongation at the plasma surface, n is the line-averaged plasma density in units $10^{20} m^{-3}$, B_T is the

toroidal field in T, P is the total plasma heating power in MW, and the α's are the exponents for the fit [67].

2.2.1 L-mode Scalings

In the L-mode operating regime, there are a variety of scaling laws. There are two types of L-mode energy confinement regions: the linear Ohmic confinement regime (LOC) and the saturated Ohmic confinement (SOC) region. In the LOC region the confinement time is found to increase linearly with density until a critical density is reached. A typical LOC scaling is the neo-Alcator scaling:

$$\tau_{e,neo} = 0.7nq\kappa R^2 a, \tag{2.21}$$

where q is the safety factor at the plasma surface. Above this critical density in the SOC region, the confinement time remains constant with density. This critical density has been determined experimentally on ATs to be:

$$n_{ecrit} = \frac{0.65A_i^{0.5}B_T}{qR}, \tag{2.22}$$

where A_i is the ion mass number in AMU [1]. For the saturated Ohmic confinement regime, there are two scaling laws that are commonly used as benchmarks. The most widely-used scaling law, the ITER89P, determines its empirical scaling from the following machines: ASDEX, DIII, ISX-B, JET, JFT-2M, JT-60, PDX, and TFTR. The energy confinement time goes as [67]:

$$\tau_{e89P} = 0.048\, M^{0.5} I_p^{0.85} R^{1.2} a^{0.3} \kappa^{0.5} n^{0.1} B_T^{0.2} P^{-0.5}. \tag{2.23}$$

A comparison of the energy confinement in several tokamaks with this scaling is shown in Fig. 2.17 [67, Fig. 2.17]. The ITER89P scaling matches the various machine energy confinement times well. Energy confinement times are frequently compared with τ_{e89}, usually by the confinement enhancement factor:

$$H_{89} = \frac{\tau_e}{\tau_{e89}}. \tag{2.24}$$

H-mode plasmas typically have a H_{89} of around 2. Another more recent scaling law, ITER97L was the first scaling law to have both a total and thermal energy confinement scaling, as follows:

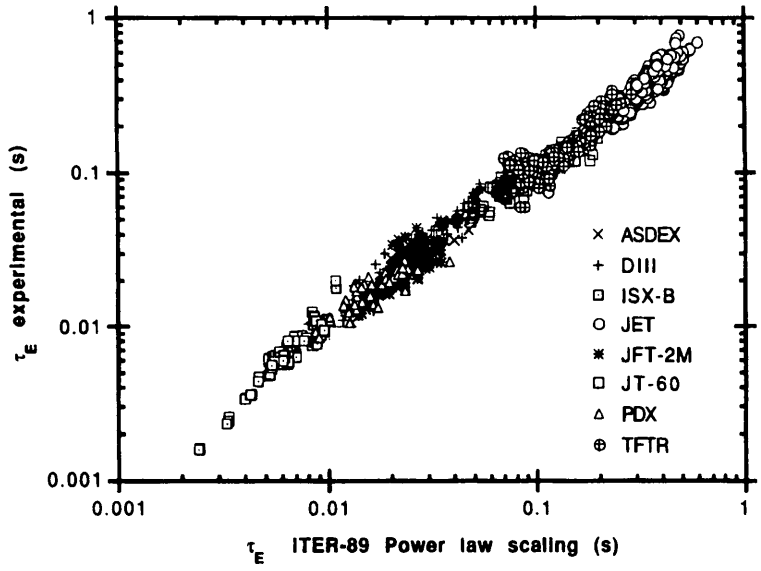

Figure 2.17: Comparison of various machines' L-mode energy confinement with ITER89P L-mode scaling

$$\tau_{e97L} = 0.037 M^{0.26} I_p^{0.74} R^{1.38} a^{0.31} \kappa^{0.67} n^{0.24} B_T^{0.2} P^{-0.57}$$

and

$$\tau_{e97Lth} = 0.023 M^{0.20} I_p^{0.96} R^{1.89} a^{-0.06} \kappa^{0.64} n^{0.40} B_T^{0.03} P^{-0.73} \tag{2.25}$$

where n is in units $10^{19}\, m^{-3}$. The scalings were drawn on data from the following machines: ASDEX, C-Mod, DIII, DIII-D, FTU, JET, JFT-2M, PBX-M, PDX, T-10, Textor, TFTR, and Tore Supra [68].

As should be noted, none of these scalings contain ST data. However, these scalings have been compared against the STs, NSTX and START. NSTX Ohmic plasmas exhibited confinement trends similar to those at higher aspect ratio. For low to moderate density on NSTX, the confinement time was found to increase with density and then saturate and decrease. Presumably this behavior represents the transition from the LOC to the SOC regime on NSTX. These trends are shown in Fig. 2.18 [69, Fig. 2.18] against the 89P scaling [69]. START's L-mode energy confinement was found to follow the ITER97L scaling relatively well, as demonstrated by Fig. 2.19 [21, Fig. 2.19], which plots the START energy confinement versus the ITER97L scaling [21]. Thus, spherical tokamaks exhibit similar L-mode confinement to those observed by higher aspect ratio machines.

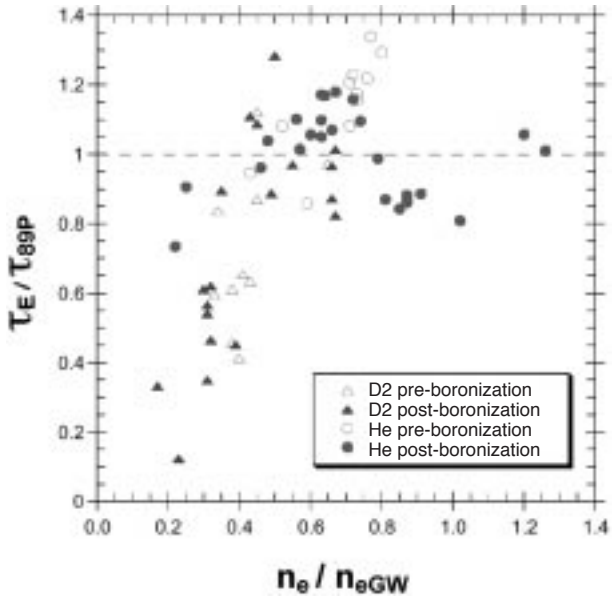

Figure 2.18: Comparison of NSTX's L-mode Ohmic energy confinement time in deuterium and helium plasmas with the ITER89P scaling at various Greenwald densities

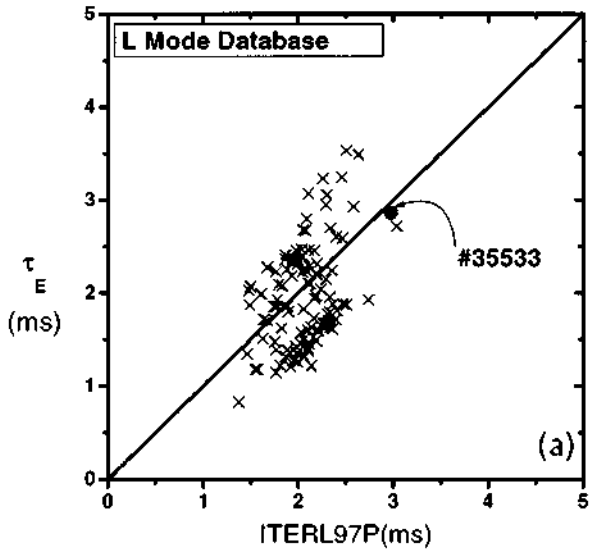

Figure 2.19: Comparison of START's L-mode energy confinement time with ITER97L Scaling

2.2.2 H-mode Scalings

In the H-mode operating regime, there are also a variety of scaling laws. These scaling laws are used to characterize ELM-free, ELMy, and both ELM-free and ELMy plasmas. A typical ELMy plasma scaling is the ITER97H, as shown:

$$\tau_{e97H} = 0.029 M^{0.20} I_p^{0.9} R^{1.84} a^{0.19} \kappa^{0.92} n^{0.40} B_T^{0.2} P^{-0.66}$$

where n is in units $10^{19} m^{-3}$. START's L-mode confinement data was found to match the ITER97H scaling [70]. Also on START at high-β_t, the H-mode energy confinement was comparable to the ITER97H scaling [71].

More commonly-used H-mode scaling laws were published in the 1999 ITER Physics Basis [1]. They are the IPB98 scalings and are valid for both ELMy and ELM-free regimes. Scalings of note are the IPB98(y,1) and IPB98(y,2), which are:

$$\tau_{eIPB98(y,1)} = 0.0503 M^{0.13} I_p^{0.91} R^{1.48} a^{0.57} \kappa^{0.72} n^{0.44} B_T^{0.15} P^{-0.65} \tag{2.26}$$

and

$$\tau_{eIPB98(y,2)} = 0.0562 M^{0.19} I_p^{0.93} R^{1.49} a^{0.58} \kappa^{0.78} n^{0.41} B_T^{0.15} P^{-0.69} \tag{2.27}$$

where n is in units $10^{19} m^{-3}$. The machines used for these scalings are: Alcator C-Mod, ASDEX, ASDEX-U, Compass-D, DIII-D, JET, JFT-2M, JT-60U PBX-M, PDX, and TCV. The IPB98(y,2) scaling is widely used and is the recommended reference scaling for the ITER design [9]. H-mode energy confinement times are usually compared with the confinement enhancement factor from the IPB98(y,2) as:

$$H_{98} = \frac{\tau_e}{\tau_{eIPB98(y,2)}}. \tag{2.28}$$

The machines in these scalings did not include any STs. However, MAST found that their thermal energy confinement time generally agrees with the IPB98(y,2) scaling. While on NSTX, they found that the global and thermal confinement factor H_{98} can vary from 0.6 to 1.4.

NSTX has incorporated MAST, START, and NSTX into a database shared with ASDEX-U, Alcator C-Mod, COMPASS, DIII-D, and JET. Using this data, a new H-mode energy confinement time scaling relationship was developed:

$$\tau_{elow_A} = 0.111 I_p^{0.80} R^{1.17} a^{0.95} n^{0.39} B_T^{0.32} P^{-0.66} \tag{2.29}$$

where κ and M were constrained to 1.6 to 2.4 and n is in units $10^{19}\, m^{-3}$. This scaling has: a weaker dependence on I_p and a stronger dependence on B_T than the IPB98(y,2) scaling [72]. The trends in spherical tokamak with a weaker dependence on I_p and more linear dependence on B_T than conventional aspect ratio tokamaks are further demonstrated when analyzing only ST data; MAST has derived a scaling law using only their data [73]:

$$\tau_{elow_A-MAST} = 0.189 I_p^{0.56} B_T^{1.4} P^{-0.73}. \tag{2.30}$$

NSTX data also has a stronger than linear dependence on the toroidal magnetic field as compared to the IPB98(y,2) scaling. These discrepancies in the ST's energy confinement dependence on B_T could be explained by their operation at an order of magnitude lower magnetic field than conventional tokamaks and thus an order of magnitude higher on β_t [72, 73]. A recent study on NSTX explored the dependence of the energy confinement time on B_T and I_p at different collisionalities using different wall conditioning. Operations at lower collisionality via lithium discharge cleaning had similar I_p and B_T dependencies on energy confinement to that seen at high-A, whereas operations at higher collisionality had similar I_p and B_T dependencies to Equation 2.30 [74]. Thus, the high-A dependence of I_p and B_T on the energy confinement was recovered on NSTX by decreasing the collisionality.

The discrepancy in the H-mode energy confinement scalings at low-A with the conventional aspect ratio energy confinement scalings demonstrates the problems with using empirical formulas, the need for a physical model, and the motivation for more experimental data at low-A. Experimental data at low-A is particularly needed to explore the energy confinement dependence on I_p and B_T.

2.3 Goals of this Dissertation

The H-mode operating regime is a well-known tokamak operating regime and is the planned operating regime of ITER. However, some key physics issues, such as the H-mode power threshold and ELM behavior, are not completely understood and call for more experimental data. More experimental data, particularly at parameter extremes, should help develop an underlying theory of the L-H transition and ELM triggering.

H-mode has been well-documented at $A > 1.3$, with some differences in H-mode and ELM behavior observed with aspect ratio. This thesis is the first work at documenting the H-mode operating regime at near-unity aspect ratio $A \lesssim 1.2$. This work addresses the following topics:

1. Describe the general characteristics of H-mode plasmas in Pegasus.
   (a) How is H-mode accessed?
   (b) How do the properties differ from low confinement (L-mode) plasmas?
2. Describe the H-mode operational space.
   (a) How does the L-H power threshold depend on density and geometry?
   (b) How does the L-H power threshold at near-unity aspect ratio compare to the ITPA08 scaling?
3. Describe the ELM characteristics and dynamics.
   (a) What ELM types are observed and what are their properties?
   (b) How does the current profile change during an ELM?

Chapter 3

Pegasus Toroidal Experiment

This chapter describes the experimental capabilities used to answer the posed goals of this dissertation. A brief summary of the Pegasus experimental device is given, followed by a description of the upgrades that allowed and/or improved H-mode access. Useful diagnostics are then described; these include light, magnetic, and electrostatic diagnostics. Next, key computing tools used in this dissertation are briefly detailed, including: the KFIT equilibrium code and the ShapeFIT fast boundary reconstruction code. Finally the chapter, briefly describes the H-mode operational space on Pegasus.

The Pegasus Toroidal Experiment [75] is a university-scale spherical tokamak at the University of Wisconsin–Madison designed to explore the physics of ultra-low aspect ratio. Pegasus is the lowest aspect ratio tokamak in the world at $A \lesssim 1.2$, thus bordering the unique physics region between spheromaks and tokamaks. This boundary is illustrated in Fig. 3.1(a), which plots the toroidal field utilization factor for various magnetic confinement devices versus aspect ratio. As demonstrated by the figure, Pegasus straddles the region between the high-I_N spheromaks and the low-I_N tokamaks. The two methods for achieved high β_t in magnetic confinement devices are high β_N and/or high I_N as illustrated in Fig. 3.1(b). Typically, high β_t plasmas are accessed through high β_N as accomplished by START and NSTX. In contrast, Pegasus utilizes high I_N to access high β_t operations.

A schematic of the facility, including many of the main features is shown in Fig. 3.2. A list of Pegasus physics parameters is given in Table 3.1. Key parameters to note include: $A = 1.15 - 1.3$, $I_p \leq 0.21$ MA, $B_T < 0.2$ T, and pulse length, $\tau_{shot} < 0.25$ s. Ultra-low aspect ratio plasmas are possible in Pegasus due to its slender, $r_{CS} = 5.5$ cm, centerstack. The centerstack consists of a

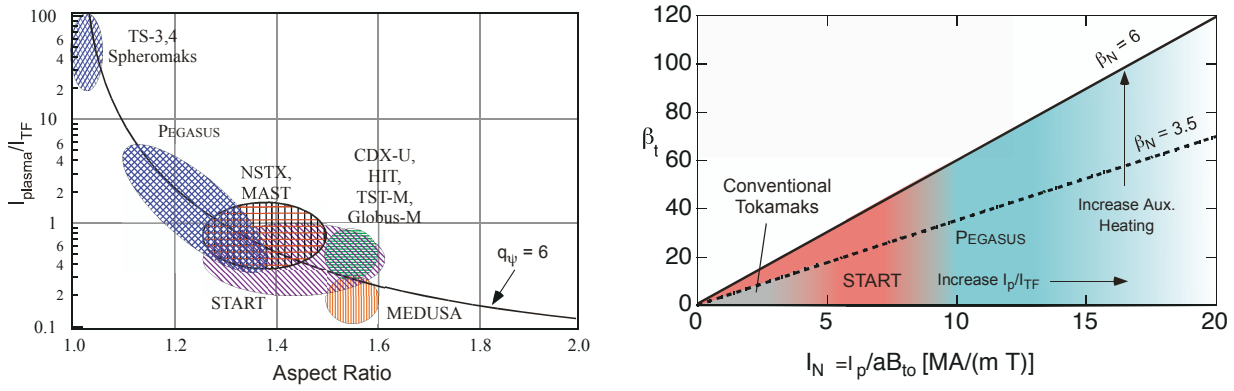

(a) (b)

Figure 3.1: (a): TF field utilization vs aspect ratio for various magnetic confinement experiments; (b): β_t access space for various magnetic confinement experiments

twelve-turn, low-inductance toroidal field set that provides $\sim 0.16\,T$ field on-axis, an unique high strength Ohmic solenoid capable of 20 T operation constructed for Pegasus by the National High Magnetic Fields Laboratory [76], cooling channels, and a variety of magnetic diagnostics. The current available Volt-seconds to drive the solenoid is $\sim$ 30 mV–s, limited by available power supplies. There are eight external poloidal field coil sets that provide vertical equilibrium field, essential for plasma stability, as well as plasma shaping. The divertor coil set has recently been augmented and a new radial coil set has been added. They will be described in further detail later in this chapter.

All electromagnetic coil sets on Pegasus are feedback-controlled with pulse-width modulation control electronics and driven by modular, solid-state switching power supplies that employ IGBT (Insulated Gate Bipolar Transistor) or IGCT (Insulated Gate-Commutated Thyristor) switches [5]. These power supplies and their associated controller technologies [77] provide programmable current control to individual coil sets with millisecond time response [16].

Achieving ultra-high vacuum (UHV) with low impurity levels, between plasma discharges is critical for good plasma operations. In order to attain UHV, Pegasus utilizes cryogenic pumping and titanium gettering. The cryogenic pump has a pump rate of 5000 $Torr \cdot L/s$ and removes N_2, O_2, and H_2O molecules. Gettering is the sublimation of chemically active metal onto the walls.

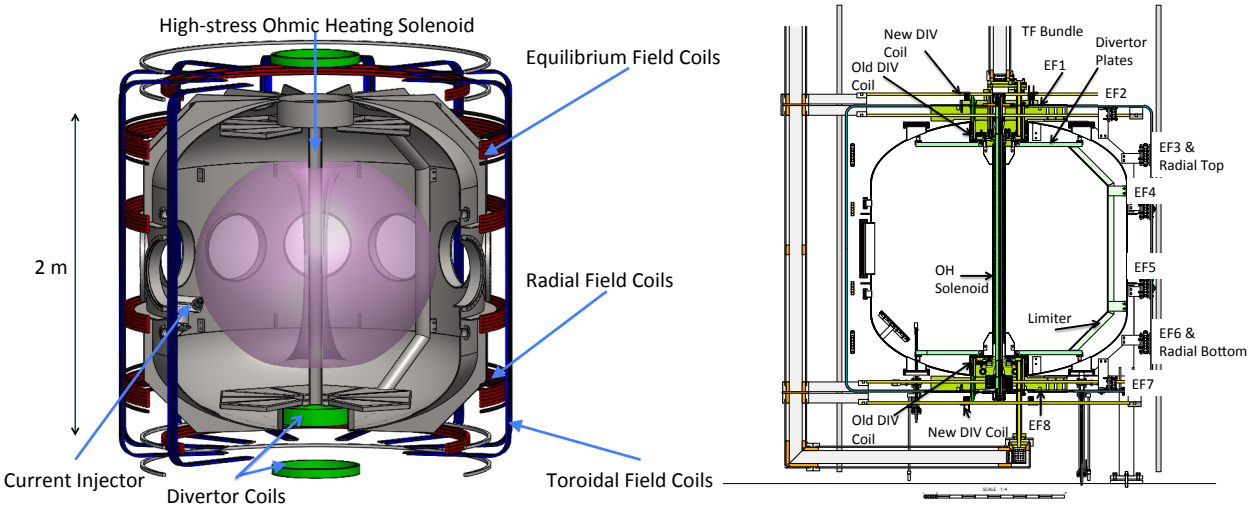

(a) (b)

Figure 3.2: Pegasus Toroidal Experiment. (a): Facility drawing; (b): Poloidal view, showing all coil sets

Parameter	**Achieved**
A	1.15 – 1.3
R [m]	0.2 – 0.45
κ	1.4 – 3.7
I_p [MA]	≤ 0.21
B_T [T]	< 0.2
I_N [MA/m-T]	6 – 12
RB_T [T-m]	≤ 0.06
τ_{shot} [s]	≤ 0.025
β_t [%]	≤ 25

Table 3.1: Achieved Pegasus physics parameters

The titanium metal removes excess H_2 from the vacuum chamber [78]. The titanium gettering covers over 80% of the plasma facing components; 0.045 to 0.15 grams of Ti are sublimated per hour. Due to the short-pulse length of the discharge, the titanium is not passivated before or during the plasma shot. The vacuum vessel is located 15 cm outside of the plasma limiter, which reduces the recycling of neutral particles from the plasma wall. The typical base pressure overnight and between shots is $< 4 \times 10^{-8}$ Torr.

There are two major research thrusts on Pegasus. The first is studying advanced tokamak physics at small aspect ratio, which this thesis describes in more detail. The other is performing non-inductive startup and growth using local helicity injection [79]. This is a crucial issue for spherical tokamaks since there is very limited available flux in the Ohmic solenoid to drive the plasma current, as well as heat the plasma. Local helicity injection is performed through the use of current injectors. The current injectors operated on Pegasus are upgrades from the current injectors developed by MST [80], which were based on the implementation at Budker Institute of Nuclear Physics in Novosibirsk [81]. Up to four injectors are in use currently in Pegasus operations. The injectors include a three plasma injector assembly and a one plasma injector assembly. A full description of the current injectors is available in [79, 82, 83]

Operations utilizing the current injectors include: injectors alone, injector startup then transitioning to Ohmic drive, injector preionization with an Ohmic startup, and Ohmic background plasmas with injected helicity current. At the present time, these injectors are capable of creating a plasma with up to ~ 150 kA of plasma current, thereby, saving precious Volt-seconds for further Ohmic drive.

3.1 H-mode Upgrades

3.1.1 HFS Gas System

Fast gas valves are used to inject working gas before and throughout a plasma discharge. Prior to this work, only LFS gas valves were used to fuel Pegasus plasmas. The LFS gas valves are located at four locations on Pegasus, with the majority of the gas valves consisting of piezoelectric gas valves, specifically PV-10s. PV-10s have a sub-millisecond time response and are not affected

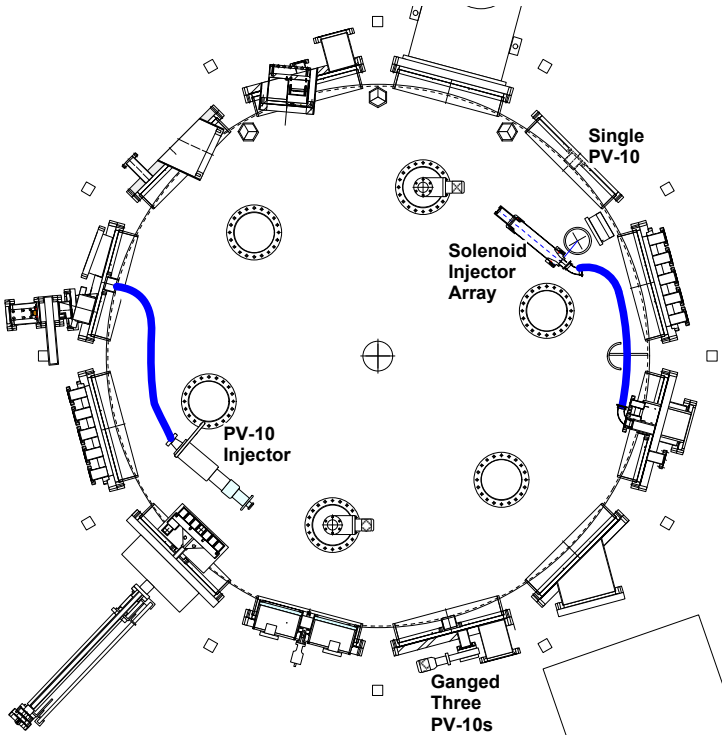

Figure 3.3: Location of Pegasus LFS fueling systems

by the tokamak's magnetic fields. The locations of these LFS fueling valves are shown in Fig. 3.3. Two sets of PV-10s are located at the vacuum wall ($R = 100$ cm), far away from the plasma. The other two LFS fuelers are contained in the two current injector sets, which are located at $R = 75$ cm. One of the injector sets has a PV-10, but the other injector array uses solenoid valves.

In order to increase fueling flexibility, a HFS gas fueling system was developed. This system was originally installed on Pegasus in 2012. That system consisted of a PV-10 gas valve located under a bottom divertor plate and an ~ 84 cm long 1.17 mm inner diameter capillary tube that provides fueling at $Z = -30$ cm on the centerstack.

However, the HFS valve throughput was affected by the titanium gettering. The gettering is believed to heat the valve. PV-10s are known to be susceptible to temperature changes. Throughout the run day, the throughput from the valve would continually decrease, presumably as its temperature was increasing. This effect is shown in Fig. 3.4. This figure compares the tank neutral pressure from a LFS gas puff [Fig. 3.4(a)] and a HFS gas puff [Fig. 3.4(b)] at the beginning of the day (when the titanium gettering was just initiated) to the end of the day (when the titanium

gettering had been on for over 6 hours). The peak neutral pressure from the LFS gas puff does not change over the course of the day. However, at the end of the day, increased wall pumping from the titanium removed the puff faster than the beginning of the day. In contrast, the neutral pressure from the HFS gas puff decreased by 15% from the beginning of the day to the end of the day. The HFS gas valve was at its nominal operating voltage of 100 V for these two gas puffs. At lowers voltages, the heating effect from the gettering is more pronounced. This is illustrated in Fig. 3.5. At 70 V, its lowest operating voltage, the neutral pressure decreased by $\sim 2\times$ from the beginning to end of the run day. On one occasion, the use of gettering in the bottom of the machine made the valve nonfunctional, presumably due to overheating. In order to repair this valve, a vessel entry was required.

To improve the robustness of the valve and make it not susceptible to temperature changes from the titanium gettering, it has since been moved outside of the tank. It now has a longer tube of ~ 1.7 m, but it still goes to a location of $Z = -30$ cm. In order to increase and spread out the location of injected HFS gas, another external HFS gas valve and capillary tube system, of similar length, has also been added at $Z = 30$ cm. Both HFS gas systems can be used separately or in conjunction with each other; a plasma image with both systems activated is shown in Fig. 3.6. The bright spots on the centerstack reveal the location of the HFS fuelers.

A comparison of HFS-fueled and LFS-fueled discharges is given in Fig. 3.7 for discharges with the same waveform pre-programming. Both discharges are fueled from the LFS until 20 ms, where they diverge. This figure has the outboard neutral pressure [Fig. 3.7(a)] and the line-averaged density [Fig. 3.7(b)] for these two discharges. The density is shown until the end of the plasma current flattop, when the plasma rapidly reduces in size. During $20-29$ ms, the LFS-fueled discharge has a neutral pressure on average $\sim 1.7\times$ higher than in the HFS-fueled case. However, the LFS-fueled case only has a density $\times 0.3$ higher than in the HFS-fueled case. Thus, the HFS system requires less gas injected than the LFS system to create plasmas with comparable densities.

The HFS fueling systems have a slower time response compared to the LFS fueling systems due to their long capillary tubes. This difference in fueling system time response is shown in Fig. 3.8. For these no-power shots, the HFS and LFS valves were both actuated at 15 ms. Neutral pressure is detected by the fast ion gauge ~ 1.5 ms later for the LFS gas puff and ~ 3.5 ms later for

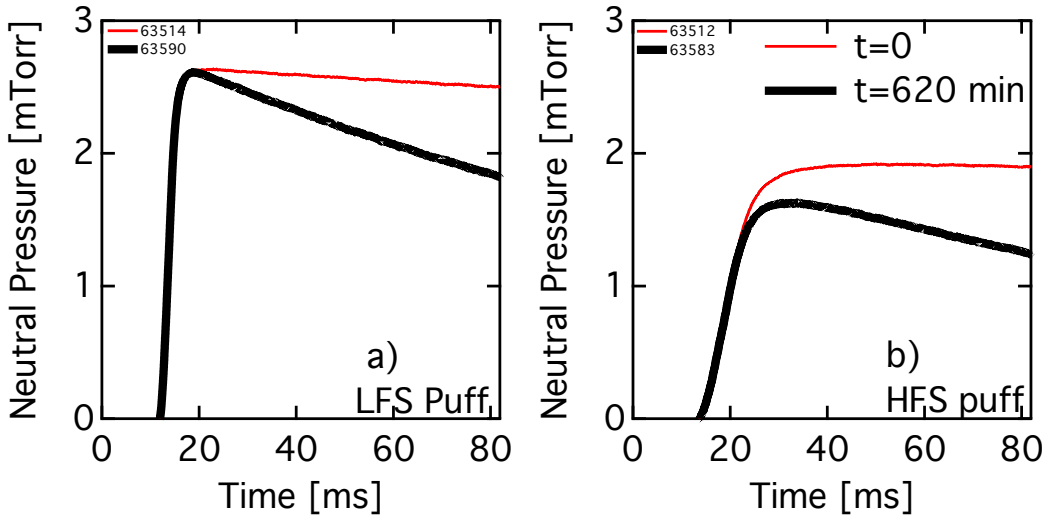

Figure 3.4: Change of LFS (a) and HFS (b) throughput over the course of a runday, presumably due to heating from titanium gettering

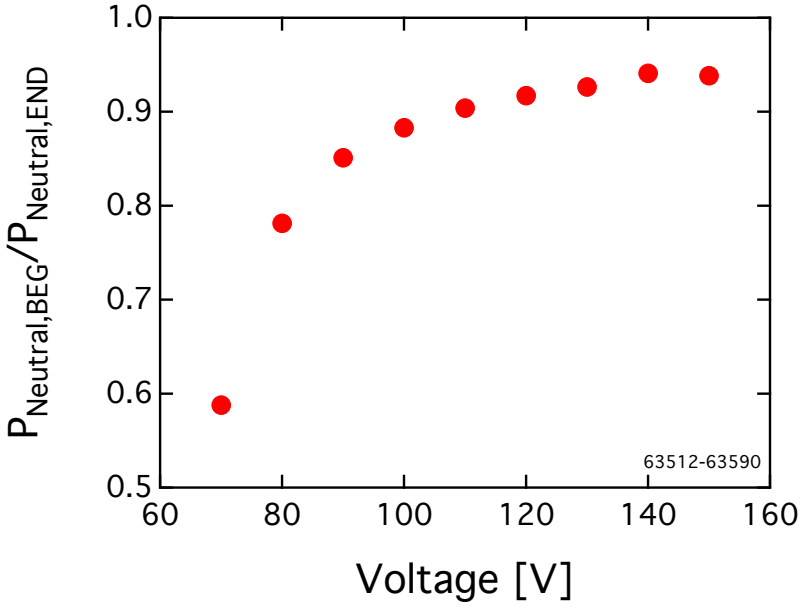

Figure 3.5: Change of HFS throughput at different valve voltages over the course of a runday, presumably due to heating from titanium gettering

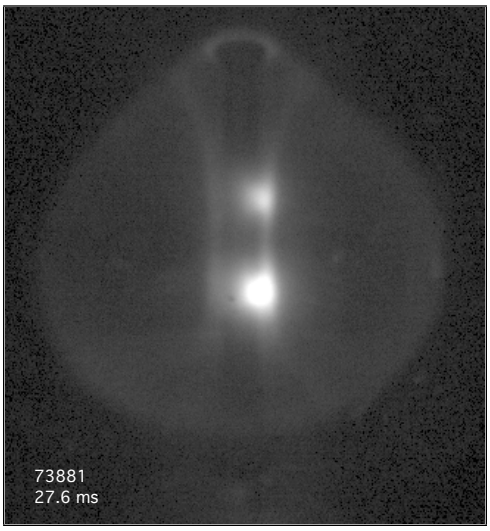

Figure 3.6: Camera image of Pegasus Ohmic plasma utilizing bottom HFS and top HFS fueling

the HFS gas puff. There is about about a 1.5 ms time of flight delay in the tank, explaining the time delay between the LFS valve actuation and pressure detection. Usually light is observed on the centerstack at the location of the HFS fuelers ~ 3 ms after the valve has been actuated. Thus, there is $\gtrsim 3$ ms time delay between HFS valve activation and gas arrival on the centerstack. This time delay is also dependent on the voltage applied to the valve. Also, once HFS fueling commences during a discharge, it is on for the remainder of the discharge since the tubes act as gas reservoirs.

Using the LFS and HFS fueling systems in conjunction with each other, regularly allows access to higher density. This is demonstrated in Fig. 3.9. For a plasma current of ~ 80 kA, $\bar{n}_e = 7 \times 10^{19} m^{-3}$ is achieved. This is $1.1\times$ higher than $n_G = 6 \times 10^{19} m^{-3}$.

The gas injected from the HFS fuelers into the discharge can be changed by varying the applied voltage or the length of time the voltage is applied to the PV-10. The top valve is operated from 120 to 180 V and the bottom valve is operated from 90 to 150 V. Varying the voltage linearly changes the total gas injected into the vessel, by as much as $10\times$, as demonstrated by Fig. 3.10(a). In this figure, the voltage is applied for 5 ms for each pulse. In Fig. 3.10(b), the pulse time of these valves is varied with the voltages held at 120 V and 140 V for the bottom and top valves, respectfully. The throughput increase linearly with pulse time for pulses > 1 ms.

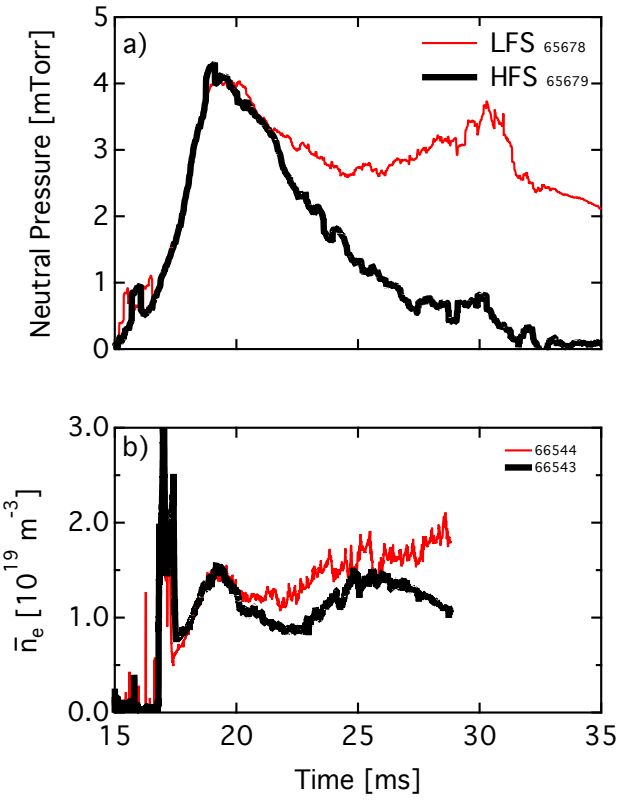

Figure 3.7: Comparison of similar limited LFS-fueled and HFS-fueled discharges. (a): Neutral pressure; (b): $\bar{n}_e$

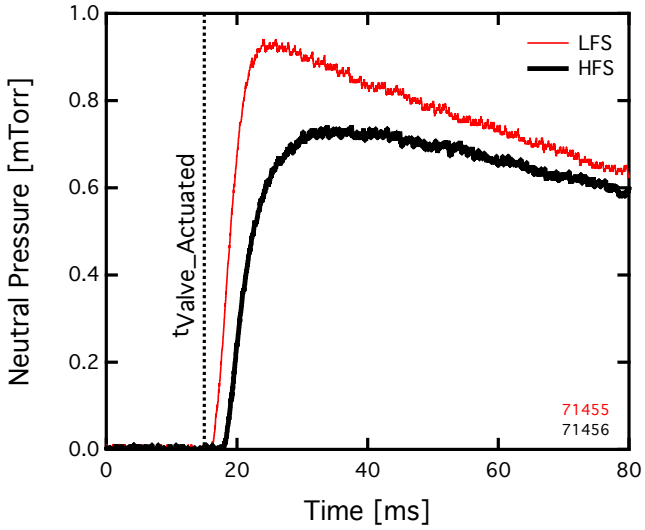

Figure 3.8: Time response of LFS and HFS fueling systems

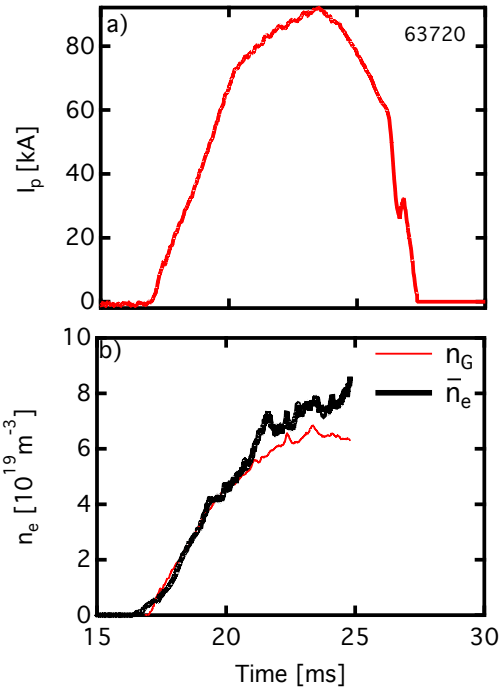

Figure 3.9: High density discharge in Pegasus. (a): I_p; (b); $\bar{n}_e$ and n_G

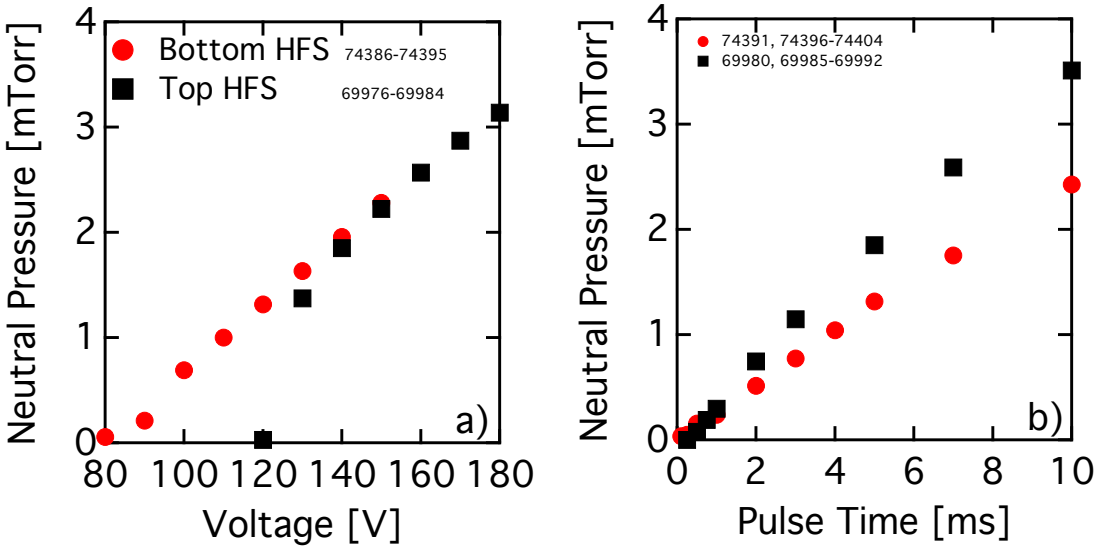

Figure 3.10: HFS valve characteristics. (a): Tank pressure vs. applied PV-10 voltage; (b): Tank pressure vs. PV-10 pulse time

3.1.2 Diverted Operations

H-mode was first achieved in Pegasus with the plasma limited on the centerstack. However, H-mode is conventionally studied in the diverted magnetic configuration. In order to create diverted plasmas in Pegasus, the divertor coil set was augmented to better match the available power supplies and plasma size. The old coil set (DIV1A and DIV2A) have 5 turns each. They are installed in the upper and lower dome assemblies at $R = 0.252$ m, $Z = \pm 0.948$ m, as demonstrated by Fig. 3.2. The new coils (DIVB1 and DIVB2) consist of 26 turns of 1/32" x 2" copper conductor with a spiral build. They are installed outside of the vessel on the dome at $R = 0.215$ m, $Z = \pm 1.188$ m.

Originally, when both sets were combined in series, the divertor coils provided up to 104 kA-turns by using one 4 kA IGBT power supply. This A-turns was predicted to fully divert a 300 kA double null plasma, as demonstrated by a predictive KFIT equilibrium reconstruction in Fig. 3.11. This reconstruction also illustrated improved diverted access with the EF1 and EF8 poloidal coils taken offline; so this modification was performed.

Both double-null or single-null diverted plasmas are possible in Pegasus. To date, the divertors have been operated in a double null configuration and upper single null configuration. Plasmas are typically operated in the upper single null direction to improve the coil response time and operate in the conventional H-mode diverted configuration. Using only the upper divertor coil, the ramp rate is ~ 840 kA/s. The upper single null configuration is in the favorable ion ∇B drift direction on Pegasus, as shown in Fig. 3.12. In the figure, which shows a top-down view of Pegasus, the toroidal field is oriented counterclockwise, with the gradient in $\vec{B}$ pointing inwards, making the ion ∇B drift direction point upwards.

During the initial tests of the augmented diverted set at $I_p \sim 100$ kA, plasmas appeared diverted on the fast camera. However, when these plasmas were reconstructed, they were determined to be centerstack-limited instead. Thus, more predictive reconstructions were performed to better understand the diverted operating space on Pegasus at $I_p \sim 100$ kA. These reconstructions illustrated that doubling the kA-turns in the divertor coils would improve diverted access at this plasma current. This modification was accomplished by adding another 4 kA IGBT bridge, for a total of 208 kA-turns. A sample predictive KFIT equilibrium reconstruction with 5.5 kA current in the upper diverted coils is shown in Fig. 3.13. This plasma is upper single null diverted. Experimental

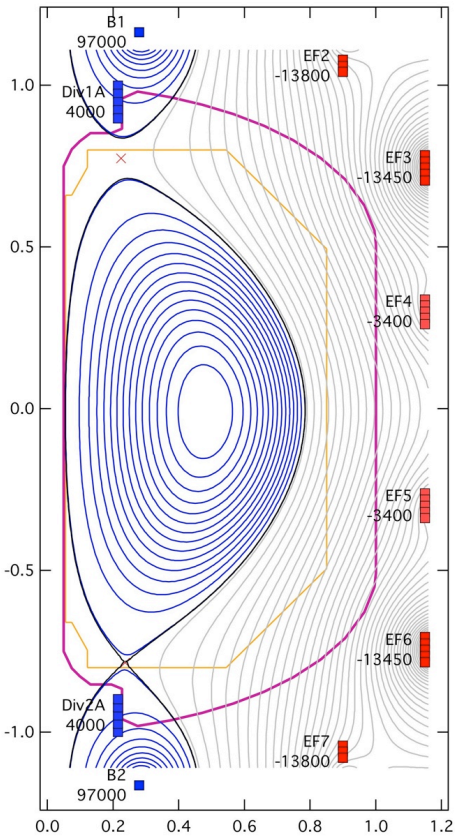

Figure 3.11: Predictive KFIT Equilibrium of a fully diverted 300 kA double null plasma in Pegasus utilizing the augmented divertor set (DIV1A, DIV1B, DIV2A, DIV2B)

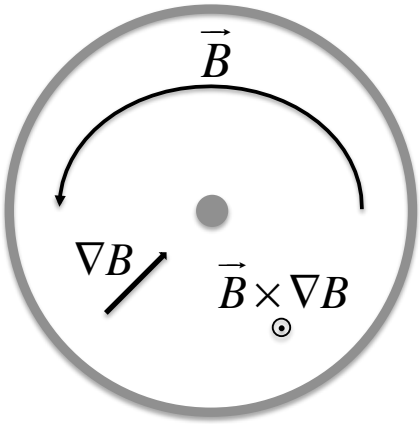

Figure 3.12: Ion ∇B drift direction on Pegasus, illustrated by top-down view of the machine

runs were conducted with this increased power capability. Diverted plasmas were then confirmed with KFIT as can be seen in Fig. 3.14. In this figure, both the camera image [Fig. 3.14(a)] and equilibrium reconstruction [Fig. 3.14(b)] show an upper single null diverted plasma.

In order to allow single null diverted plasma operations in Pegasus, vertical position control was added. This was accomplished by adding a radial coil set. The radial coil set consists of two sets of two coils each placed on the EF3 and EF6 coils at $R = 1.148$ m, $Z = \pm 0.813$ m, and $R = 1.148$ m, $Z = \pm 0.655$ m. The two sets are run anti-parallel and in series with an inductor. The radial field uses a single 4 kA IGBT bridge. The vertical field from this coil is oriented down to offset the upward plasma vertical motion. This motion is created by the top divertor coils and the magnetized floor rebar.

After diverted operation commenced in the upper single null configuration, it was found that these plasmas were more vertically unstable than limited plasmas and prone to vertical disruption events (VDEs). Upper and lower VDEs both occur, but upper VDEs are more common. Limited plasmas do not experience vertical disruption events. The vertical stability is typically characterized by the field index number, as defined by Equation 1.8. In limited Pegasus plasmas, $n^* = 0.2 - 0.4$ at the magnetic axis ($R = 0.4 - 0.5$ m, $Z = 0$ m). Thus, limited plasmas are stable to VDEs. Predictive equilibrium reconstructions were done to explore the vertical stability of diverted discharges in Pegasus. It was determined that n^* decreased when the divertor coils were enabled compared to limited plasmas. The reconstructions illustrated that vertical stability improved with bigger plasmas. Experimentally, to prevent VDEs, plasmas are made as big as possible and a divertor current of $< 7\,kA$ is used. Divertor currents above this level always result in a VDE.

A Pegasus discharge with a VDE is shown in Fig. 3.15. In the millisecond before this disruption, $n^* = 0.1$ at the magnetic axis. Thus, this plasma and other similar diverted discharges are marginally vertically stable. This result is consistent with some repeat discharges ending in VDEs and others remaining stable throughout the discharge. In the left figure, the plasma current and loop voltage for this discharge are shown. A sudden drop in the plasma current is seen at ~ 27.7 ms. Confinement is lost in less than 0.5 ms. Even though the loop voltage extends to ~ 29 ms the plasma does not recover after this event. A negative kick in the loop voltage is also seen at the

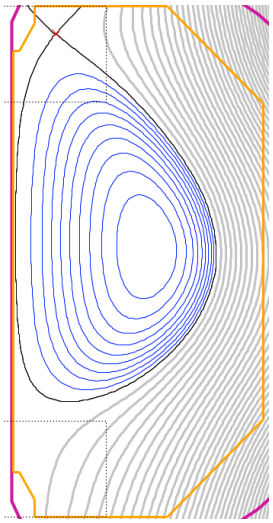

Figure 3.13: Predictive KFIT flux plot showing a diverted upper single null plasma at 5.5 kA of coil current

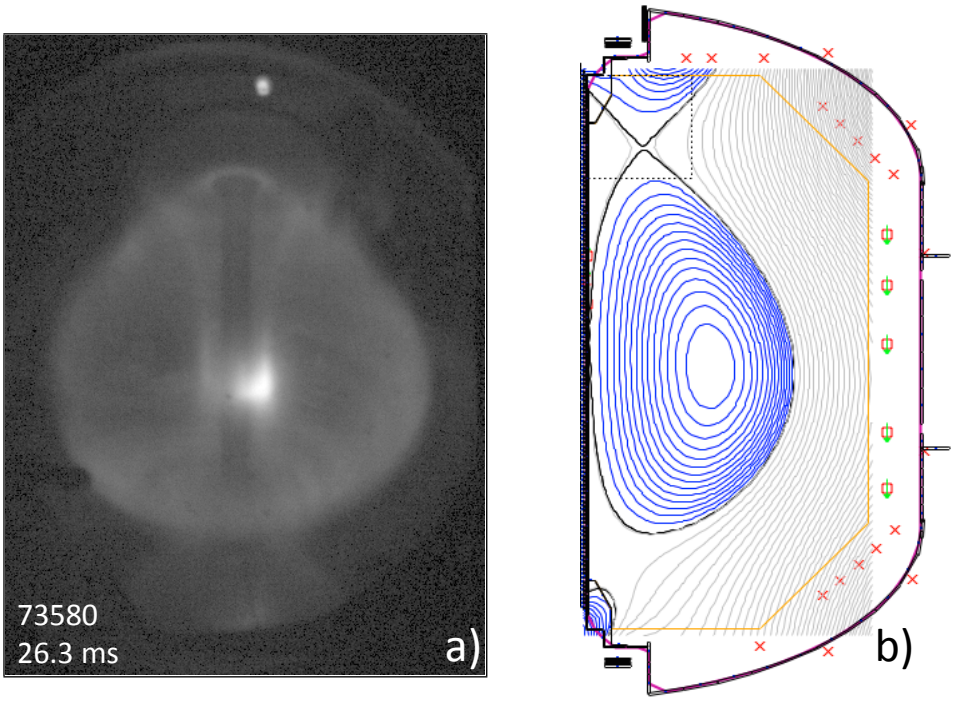

Figure 3.14: Camera image (a) and equilibrium flux plot (b) of upper single null diverted discharge

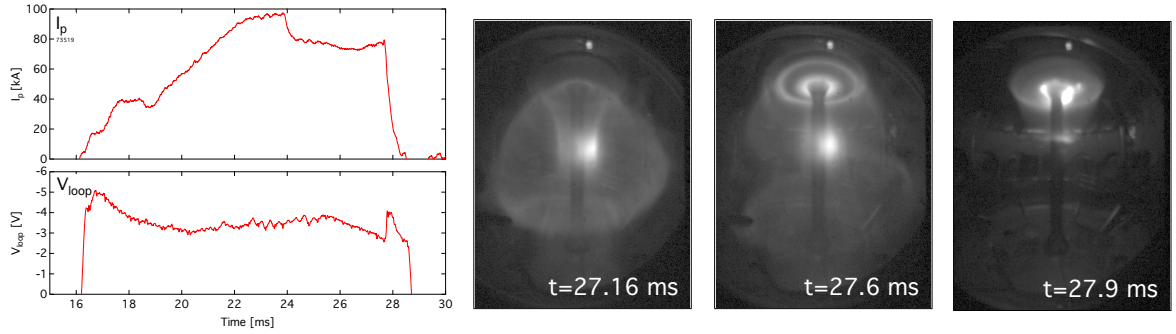

(a) (b)

Figure 3.15: Vertical Disruptions in Pegasus. (a): I_p and V_{loop} of shot with a VDE at $\sim$ 27.7 ms; (b): Camera Image of VDE

VDE time. A series of camera images: before, during and after this VDE, is shown on the right. The plasma quickly goes from being stable to hitting the top of the machine.

The plasma current and relevant poloidal fields for the diverted shot shown in Fig. 3.14 are displayed in Fig. 3.16. They are compared against a typical limited plasma to illustrate the required discharge programming differences between the two topologies. There are three main differences between these discharges: 1) the application of divertor current, 2) the lower achieved plasma current and 3) the change in the vertical fields.

The divertor current is ramped up gradually during the diverted discharge due to the limitation of the power supplies and to maintain vertical stability. The diverted current starts out with a precharge of 2.5 kA and then during the I_p flattop ramps up to 6.5 kA. The divertor precharge improves the breakdown null as compared to the limited discharge as can be seen in Fig. 3.17. This figure shows the respective nulls for these two discharge types calculated using a wall model. The limited plasma has a quadropole null, whereas the diverted plasma has a higher order hexapole null with a reduced vertical field. The plasma current is lowered in the diverted discharge due to anti-drive from the divertor. In order to prevent VDEs in diverted discharges, the radial field current is maximized and the vertical field from the lower vertical coils (EF67) are lowered.

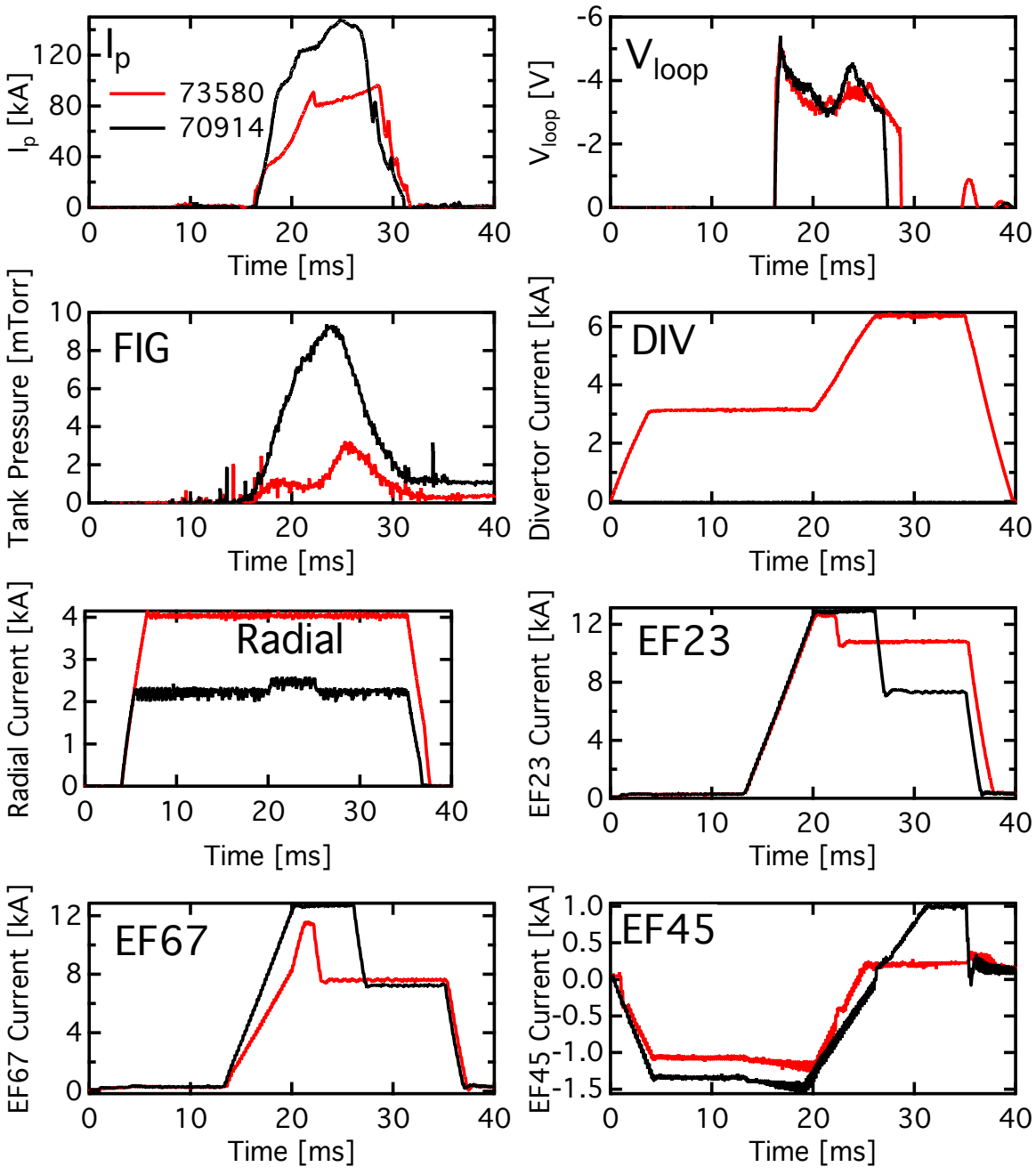

Figure 3.16: Diverted (in red) and limited (in black) discharge waveforms

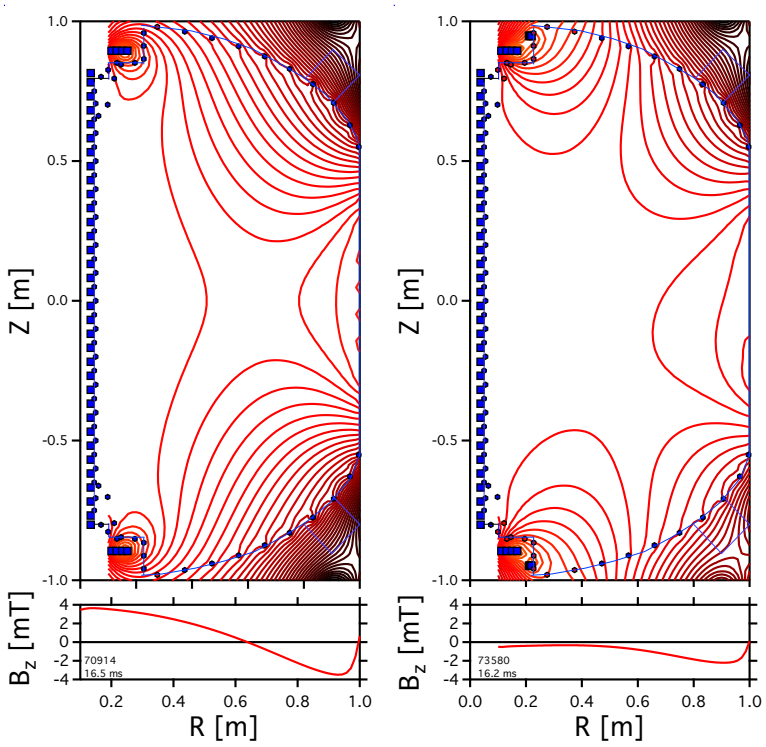

Figure 3.17: Breakdown null of limited (left) and diverted (right) plasmas in Fig. 3.16

3.2 Diagnostics

Pegasus has a suite of light, magnetic, and electrostatic diagnostics that are routinely utilized for these experiments, most of them are shown in Fig. 3.18.

3.2.1 Light Diagnostics

Fast Camera The fast cameras provide full-plasma views at high-temporal resolution that guide physics operations. Pegasus images the entire plasma during a shot through the use of a Vision Research Phantom v12.0 fast camera coupled with a fisheye lens as well as a macro lens. A Schott RG red filter that cuts on at 610 can also be installed to look only at D_α light. However, the majority of visible emissions is from D_α emissions; this is illustrated in Fig. 3.19. This data was taken with the visible light spectrometer during a local helicity injection discharge. The figure illustrates that the dominant visible emissions are from the Balmer series. This camera has a 1280 x 800 CMOS sensor with a bit depth of 12. Frame rate and resolutions are 6.2 kfps at the full 1280 x 800

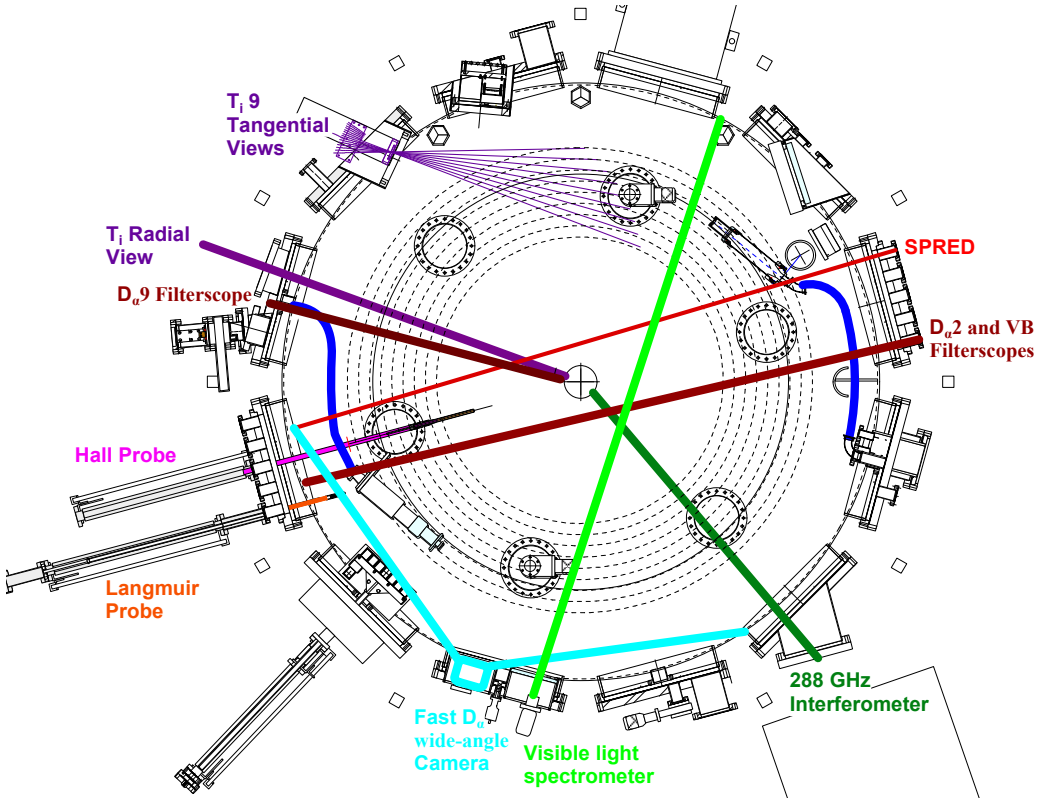

Figure 3.18: Pegasus diagnostics, looking down from the top of the machine

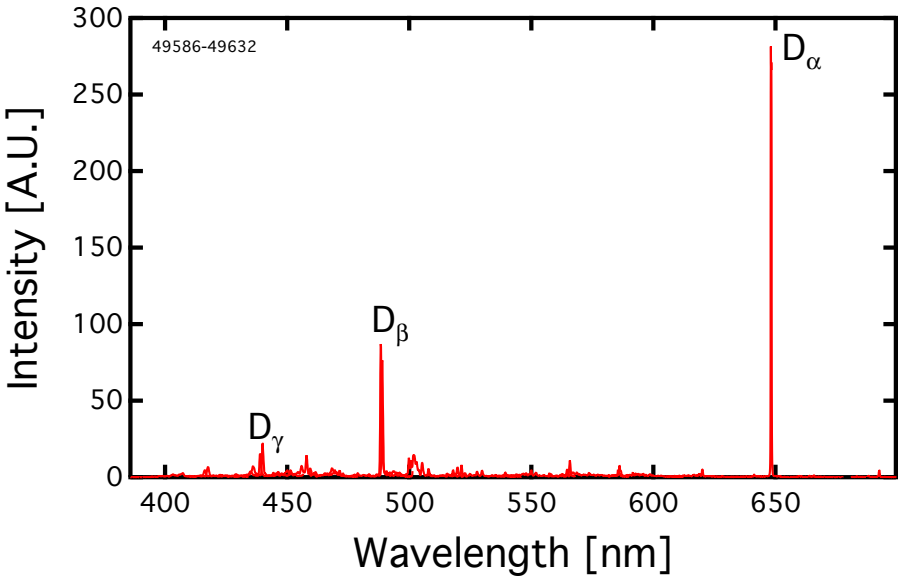

Figure 3.19: Visible emissions on Pegasus measured using a visible survey spectrometer

resolution, and up to 1 Mfps at a resolution of 128 x 8. A common resolution used to view the entire plasma during the shot is 28 kHz at 512 x 384.

Another camera, sometimes used to image the entire camera in a similar setup as described for the v12.0, is a MotionPro X4, manufactured by Integrated Designs Tools, Inc. It has a 512x512 monochrome CCD detector with 8-bit resolution, exposure times < 10 μs, and a nominal 5 kHz full framing rate.

Fast Filterscopes Pegasus currently has three fast filterscopes; two of the filterscopes have a D_α filter and the third has a Visible Bremsstrahlung filter. The two different D_α optical chords of the plasma are each imaged onto an optical fiber; one filterscope; $D_\alpha 9$, images the HFS fueling while the other filterscope, $D_\alpha 2$, does not. These filterscopes all have a near-radial view, with 3 μs resolution and are not absolutely-calibrated for intensity.

D_α and H_α radiation results from the collisional excitation of a neutral hydrogen or deuterium atom from the plasma facing components when it interacts with the plasma [84]. D_2 is used as the working gas on Pegasus, but H_2O is present as an impurity. The spectral lines are only 0.2 nm apart, making them difficult to distinguish from each other. The hydrogen ionization rate and plasma fueling by recycling can be deduced from total D_α/H_α line intensity, since the energy

required to excited the n=3 level of hydrogen is approximately the same as the ionization potential [84].

The D_α monitors also serve as a diagnostic for the presence of ELMs [50].

The Visible Bremsstrahlung continuum emissivity goes as [85]:

$$\varepsilon_{VB} = \frac{9.5 \times 10^{-13} \bar{n}_e^2 Z_{eff} \bar{g}_{ff}}{\sqrt{T_e}} \exp\left(\frac{-hc}{T_e \lambda}\right), \tag{3.1}$$

where ε_{VB} is the intensity of the Visible Bremsstrahlung in $photons/(nm \cdot cm^3 \cdot s)$, $\bar{n}_e$ is the line averaged electron density in m^{-3}, Z_{eff} is the effective particle charge, $\bar{g_{ff}}$ is the temperature-averaged free-free Gaunt factor, T_e is the electron temperature in eV, and λ is the wavelength in nm. A qualitative interpretation of density during the plasma discharge is provided when T_e is constant by analyzing the Visible Bremsstrahlung filterscope.

Visible light survey spectrometer A visible light Czerny-Turner spectrometer is used to conduct visible light surveys of Pegasus, an example of which is shown in Fig. 3.19. The spectral range of the spectrometer is from $400-800$ nm with 2 ms resolution. It has three diffraction gratings installed: 150 grove/mm, 1200 grove/mm, and 2400 grove/mm that provide the necessary spectral dispersion required for a particular experiment. Figure 3.19 was created by stitching together the spectrum from many repeat discharges. Typically the spectrometer observes $30-50$ nm at one time. The spectrometer is roughly spectrally calibrated.

Ion Doppler Spectrometer A multi-point, high-speed ion Doppler spectrometer [86] is used to measure radiation emitted by electrons undergoing atomic energy level transitions. This diagnostic relies on radiation emitted from impurity ions naturally present in the tokamak. The spectrometer has a spectral range from $200-700$ nm. The spectrometer channels include edge tangential views and a radial view. A shuttering mechanism is also used. Images are taken using a Phantom v310 camera with 200 μs resolution.

The spectrometer determines the impurity ion temperature and impurity toroidal rotation by measuring the Doppler broadening in ion impurity emission lines. Typical emission lines used for these experiments are OV at 278.101 nm with an ionization potential of 113.9 eV and CV at

227.091 nm with an ionization potential of 392 eV. The ion impurity temperature is determined from the broadening of its emission line, with the instrument profile removed and by using this formula:

$$T_i = \frac{FWHM \cdot M \cdot 1.7 \times 10^8}{\lambda_0}, \tag{3.2}$$

where T_i is the ion impurity temperature in eV, FWHM is the spectral full width half maximum for that spectral line, M is the mass number in amu of the emitting atoms, and λ_0 is the rest emission wavelength. Similarly, the shift in central wavelength from λ_0 along a line of sight is proportional to the bulk ion velocity in that direction. Thus, the velocity of ions is proportional to

$$v = c\frac{[\lambda - \lambda_0]}{\lambda_0}, \tag{3.3}$$

where c is the speed of light.

Thomson scattering System A Thomson scattering system [87] is currently under development on Pegasus. The system uses a frequency-doubled, Q-switched Nd:YAG laser operating with an energy of 2 J at 532 nm with a pulse duration of 7 ns FWHM. The laser fires once during the discharge and there are 12 spatial channels. Thomson scattering will provide spatial profiles of electron temperature and electron density. There are two available spectral gratings: the first is optimized for temperatures from 10 to 100 eV and the second from 100 to 1000 eV. Some preliminary data is available with the low temperature grating.

Microwave Interferometer A Michelson Heterodyne Microwave Interferometer is used to measure line-integrated electron density $n_e l$ during a plasma shot. The line-averaged electron density is determined by:

$$\bar{n}_e = \frac{n_e l}{p}, \tag{3.4}$$

where p is the path length of the interferometer. It is typically equal to $4a$. The interferometer has a double-pass radial view, 288 GHz mm wave radiation, and 100 μs resolution. The plasma cutoff density is 100 x$10^{19}\,m^{-3}$. The densities measured in Pegasus Ohmic plasmas range from $1-6\times10^{19}\,m^{-3}$.

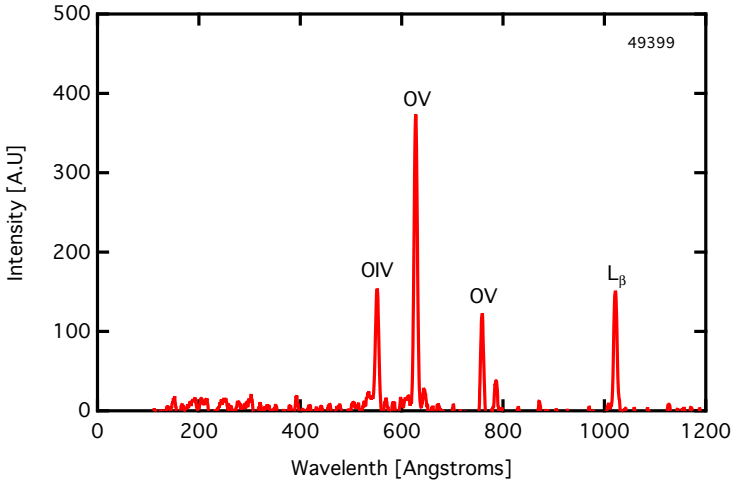

Figure 3.20: SPRED spectrum for a typical Pegasus Ohmic plasma

SPRED VUV Spectrometer The SPRED VUV [88] spectrometer is used to obtain a qualitative overview of the impurity content in the discharge. This data conveys when the impurity content in a given plasma is high and which impurities are contaminating the plasma; with this knowledge these situations can be circumvented or addressed. The spectrometer provides a crude estimate of electron temperature by comparing various line ratios. It measures relative intensity of spectral lines from 10 nm to 110 nm, with a 200 μs time resolution.

The imaging system has recently been improved by using a Tamron AF60mm f/2 1:1 macro lens and a full-frame camera (the X4.) A sample SPRED spectrum of a typical Pegasus Ohmic plasma is shown in Fig. 3.20.

3.2.2 Magnetic Diagnostics

Standard Magnetic Diagnostics Pegasus has a variety of standard tokamak magnetic diagnostics used to measure MHD instability signatures as well as constrain equilibrium reconstructions. These are shown in Table 3.2 [8]. These include: a plasma Rogowski coil to determine the plasma current; a diamagnetic loop to measure the toroidal flux, interior and exterior flux loops to find the poloidal flux, and arrays of Mirnov coils to obtain the local magnetic field and its fluctuations. The in-vessel locations of flux loops, Mirnov arrays, and nominal calibrated Mirnov orientations are shown in Fig. 3.21. Note the abbreviations for the magnetic diagnostics are given in Table

3.2. Central column flux loops are indicated at $r = 0$ for clarity, but they are actually installed at nominally $r = 5.5cm$.

High-n Toroidal Probe Array Pegasus also has a variety of magnetic probe arrays used to diagnose spatial dependence and spectral dependence of electromagnetic edge instabilities [16]. A scanning Mirnov coil array is used to diagnose edge instabilities and constrain equilibrium reconstructions. This array consists of seven-identically-size 2.62 cm $\times$ 2.30 cm Mirnov coils, oriented to measure B_z. Six coils are placed in a linear array, the distance from the center of one coil to the next is 30 mm, and a seventh coil has a purely radial offset from the first coil by 8.81 cm. The array can measure toroidal mode numbers up to 20.

Hall Probe A novel Hall probe array [89] is installed to measure the internal $B_Z(R,t)$ of Pegasus plasmas to diagnose the current profile, $J(\Psi,t)$. The probe consists of sixteen surface-mounted InSb Hall effect magnetic sensors in a linear array. The distance from the center of the first sensor to that of the last is 11.25 cm. It has high spatial and temporal resolution with a bandwidth of 25 kHz. The sensors gains are dependent on both temperature and perpendicular magnetic field to the sensor (radial and toroidal), requiring a series of two vacuum-field shots for in-situ calibration. In the presence of an elongated tokamak equilibrium, the array can be used to calculate the local toroidal current density profile. This is accomplished by using the following equation from Petty *et al.* [90]:

$$\mu_0 J_\phi = -\frac{B_z}{\kappa^2 (R-R_0)}\left(1-\frac{Z^2 R_0}{\kappa^2 R (R-R_0)^2}\right) - \frac{\partial B_z}{\partial R}\left(10\frac{Z^2 work}{\kappa^4 (R-R_0)^2}.\right) \tag{3.5}$$

The Hall Probe internal profile data can also be utilized as a measurement constraint in Pegasus equilibrium reconstructions.

3.2.3 Electrostatic Diagnostics

Langmuir Probe A triple Langmuir probe has been updated since 2011[16] and is shown in Fig. 3.22. It has a flat frequency response of up to 200 kHz. The assembly may be linearly translated with mm-level precision up to a major radius of 47 cm. The graphite shielding on the probe

Name/Abbreviation	Type	Measures	Number
PlasmaRog	Rogowski Coil	I_p	2
Diamag	Diamagnetic Loop	Φ	2
FL	Non-core Flux Loop	ψ_p	20
CFL	Centerstack Flux Loop	ψ_p	6
WL	Outboard Flux Loop	$\psi_p + \psi_{p,wall}$	6
P	Outboard Poloidal Mirnov Array	dB/dt, B, m	13
LR	Centerstack Poloidal Mirnov Array	dB/dt, B, m	7
HR	Centerstack Poloidal Mirnov Array	dB/dt, B, m	21
OT	Outboard Toroidal Mirnov Array	dB/dt, B, n	6
CT	Centerstack Toroidal Mirnov Array	dB/dt, B, n	5

Table 3.2: Pegasus internal magnetic diagnostics sets

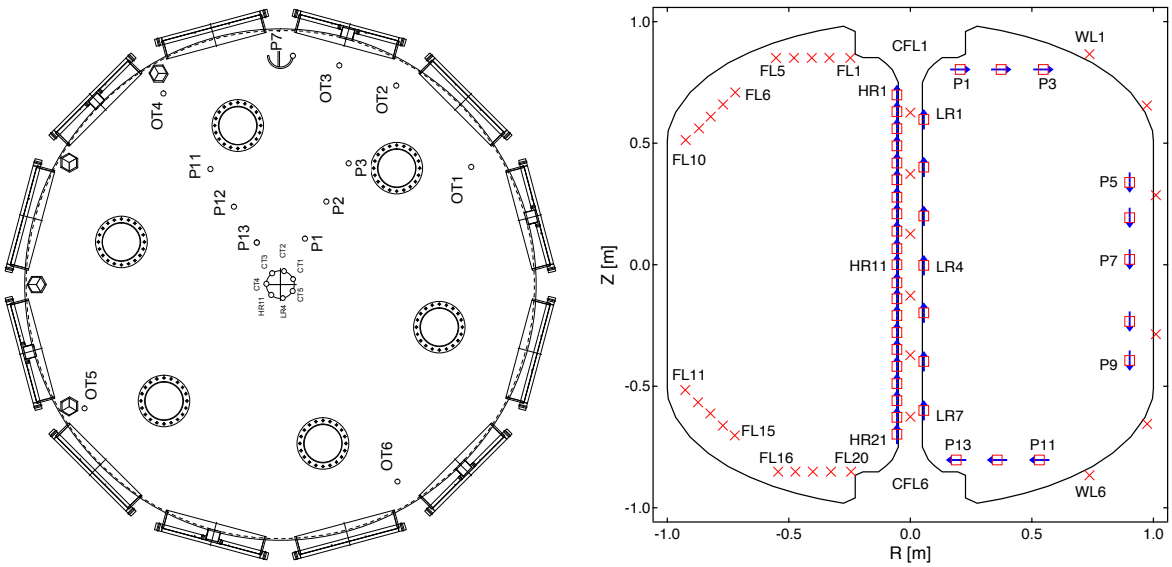

(a) Toroidal Mirnovs

(b) Poloidal Mirnovs and flux loops

Figure 3.21: Pegasus external magnetic diagnostic locations, as-built

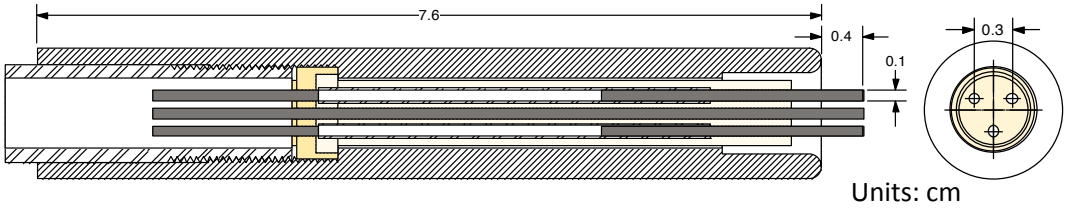

Figure 3.22: CAD drawing of the updated Langmuir probe head

has been extended to cover the leading 43 cm of the probe to prevent the probe from acting as a limiter, which it did previously with its previous material of stainless steel. Cylindrical tungsten probe tips with 7 mm height and 1 mm diameter and separated by 3.5 mm are used to sample the local plasma parameters.The distance between the probe tips has been increased from the previous design to reduce arcing the between the tips.

The Langmuir probe measures edge T_e, edge n_e, and edge fluctuations. A triple Langmuir probe has three probes: one tip provides the floating potential and the other two are biased with respect to each other. The two biased probes are used to measure temperature, the electron temperature can be determined from:

$$\left(1-\exp\left(e\left(V_1-V_f\right)/Te\right)A_1+\left(1-\exp\left(e\left(V_2-V_f\right)/Te\right)A_2=0, \tag{3.6}$$

where e is the electron charge, V_1 is the voltage from one of the biased probes, V_f is the floating potential, A_1 is the surface area of the first probe, V_2 is the voltage from the second biased probe, and A_2 is the surface area of the second probe. Since this equation is transcendental, it must be solved numerically. The density measurement requires all three probes as is illustrated by:

$$n_e=\frac{I_{sat}}{Aec_s}\exp\left(1/2\right), \tag{3.7}$$

where I_{sat} is the ion saturation current which is equal to the probe current, A is the surface area of the probe tip (ideally all probe tips are the same area), and c_s is the sound speed defined as $c_s=\sqrt{KT_e/M}$ where K is Boltzmann's constant and M is the ion mass.

3.3 Computing Tools

3.3.1 Equilibrium Reconstructions

Plasma equilibrium reconstruction is a routine tool to determine various parameters and profiles in toroidal plasmas by using a suite of magnetic measurements and boundary conditions to constrain numerical iterations of an equilibrium until the reconstructed equilibrium matches the plasma measurements. Reconstructions generate self-consistent solutions to the Grad-Shafranov equation. The Grad-Shafranov equation is a MHD equilibrium equation for an axisymmetric toroidal system, such as a tokamak. It is derived from Equation 1.1 and is given by:

$$\Delta^* \psi = -\mu_0 R^2 \frac{\partial p}{\partial \psi} - G\frac{\partial G}{\partial \psi}, \tag{3.8}$$

where Δ^* is the elliptical differential operator expressed by $\Delta^* = R\frac{\partial}{\partial R}\left(\frac{1}{R}\frac{\partial}{\partial R}\right) + \frac{\partial^2}{\partial Z^2}$, R is the major radius, $p(\psi)$ represents the plasma pressure, ψ is the poloidal flux function, and $G(\psi)$ is a current flux function that represents the toroidal magnetic flux. It is related to the poloidal current density by $G(\psi) = \frac{RB_\phi}{\mu_0}$. The Grad-Shafranov equation is a second-order partial differential equation. In order to solve this equation, numerical iterations must be performed [91]. The two free plasma profile functions that are solved for are $\frac{\partial p}{\partial \psi}$ are $2G\frac{\partial G}{\partial \psi}$.

Equilibrium reconstructions are performed on Pegasus by using the KFIT Grad-Shafranov solver in the programming language of Igor Pro. They are performed at a time of interest during the discharge. The reconstruction task is separated into two steps: numerical solution of the Grad-Shafranov equation and a χ^2 minimization technique that iterates to match equilibrium parameters with experimental parameters. A wall filament model for the vessel and coil currents is coupled into Grad-Shafranov solver to estimate the significant wall currents during a discharge. The two free functions are fit using a polynomial profile parametrization. These equilibria provide various plasma parameters and profiles of interests for a specific time point by using a set of measurements and boundary conditions to constrain numerical iterations of an equilibrium solution until the reconstruction equilibrium matches the actual plasma information [16].

Every reconstruction described here is constrained by the plasma current, non-core flux loops, wall loops, and toroidal flux calculated from diamagnetic loop. When possible, the outboard

poloidal Mirnov array midplane sensors (P5-9) and centerstack poloidal mirnov arrays (both LR and HR) are also used. Each reconstruction is constrained by at least one centerstack poloidal Mirnov sensor. Usually at least 30 magnetic constraints are used for each reconstruction.

A sample KFIT equilibrium output of a Pegasus Ohmic limited plasma is given in Fig. 3.23. The reconstructed plasma flux surfaces is shown on the left. The normalized q_ψ, current, and pressure profile are shown on the right. Some of the derived plasma parameters are displayed at the bottom.

Ohmic reconstructions on Pegasus are nontrivial and time intensive. This is largely due to internal tearing MHD modes, short pulse lengths, and large wall currents. The internal tearing mode is a result of the low required B_T at low aspect ratio; it is present in all Ohmic discharges above $I_p \sim 80$ kA on Pegasus. The discharges are rapidly evolving during the short pulse and are not equilibrated at the end of the discharge when the Ohmic drive is terminated. Due to the short pulse, strong wall currents $I(t)$ are induced in the vacuum vessel and must be accounted for when performing equilibrium reconstructions. Some discharges cannot be reconstructed due to these limitations.

Most reconstructions in this dissertation are performed by a series of Grad-Shafranov fits. First, a good guess that satisfies Grad-Shafranov equilibrium is necessary to begin the reconstruction fitting process. The first fit uses the plasma current, non-core flux loops, wall loops, and toroidal flux signal as measurement constraints. After good agreement is achieved between the fitted value and actual value of the measurements (sometimes with multiple fits), the second fit (or series of fits) incorporates the midplane sensors as constraints to the previous fit. The next series of fits includes: the addition of the centerstack poloidal sensors then, if necessary, other constraints such as divertedness. Sometimes these fits can be combined; however, it has been found that best reconstructions follow this iterative pattern.

A low as possible normalized chi square is preferred for a quality reconstruction, with $\chi_N \lesssim 2$ desired. However, χ_N is dependent on many discharge parameters, including: error assigned to the measurement; time in the discharge (earlier time points in discharge are harder to reconstruct due to the strong wall currents and typically have higher χ_N); MHD level in the discharge (more MHD means higher χ_N); plasma current (higher plasmas currents are easier to reconstruct and

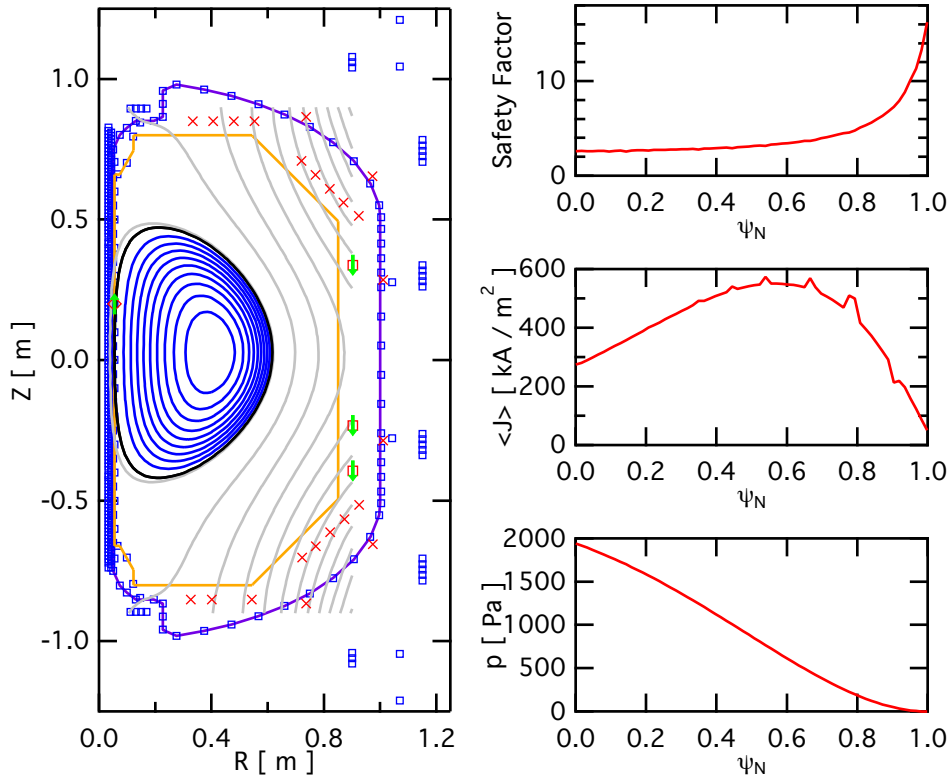

Equilibrium Parameters
Shot 66221, 34.80 ms

I_p	169 kA	R_0	0.336 m
β_t	0.081	a	0.281 m
ℓ_i	0.42	A	1.20
β_p	0.31	κ	1.6
W	2101 J	δ	0.44
B_{T0}	0.179 T	q_{95}	9.92

Figure 3.23: A sample KFIT equilibrium reconstruction of a Pegasus Ohmic Plasma showing: flux plot on the top left; q, current, and pressure profiles on the right and plasma characteristics on the bottom

typically have lower χ_N); type of magnetic constraints (each centerstack Mirnov used increases χ_N); and type of discharge (for example diverted discharges are more difficult to reconstruct and have higher χ_N.) The priority of agreement between measurement and derived value is: plasma current and toroidal flux, non-core flux loops and wall loops, midplane sensors, and centerstack poloidal mirnov arrays.

Previously, reconstructions were performed at a single time point during a discharge. For this work, multiple time points during a discharge are needed in order to calculate the energy confinement time and the H-mode power threshold. The time points of the reconstructions are spaced throughout at least a few millisecond time period. Ideally, these time points are later in the discharge, after an I_p flattop has been established and away from strong changes in the equilibrium fields.

A time-evolving reconstruction is performed similar to a single time point reconstruction. A solution is achieved for a single time point and then a new time time point reconstruction is begun. Sometimes a solution for a previous time point will be used as an initial guess for the next time point. The same constraints (measurements, fits, etc.) are used (when possible) for each time point in a time-evolving reconstruction.

Each single reconstruction calculates the magnetic and kinetic energy for a given time point. The change in the magnetic and kinetic energy are obtained by determining the linear slope of the magnetic and kinetic energy versus time.

Time-evolving reconstructions can be used to determine an L-H transition time. At the transition, a change in the slope of the total plasma energy W and kinetic energy W_k is typically observed, as shown in Fig. 3.24. For this diverted discharge, W_k and W are both constant during the L-phase. However, at the L-H transition both W_k and dW_k/dt increase compared to their L-mode values. The magnetic energy W_m has similar behavior to W and W_k during this discharge.

The H-mode power threshold is calculated by:

$$P_{LH} = I_p V_{loop} - dW/dt - P_{RAD,} \tag{3.9}$$

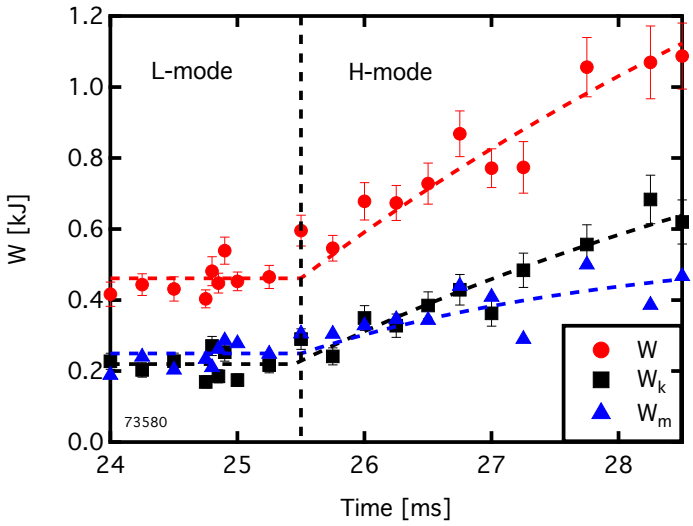

Figure 3.24: Plasma energy evolution of a diverted discharge with both a L- and H-phase

where V_{loop} is the loop voltage in V, $\frac{dW}{dt}$ is the change in the stored plasma energy in W, P_{RAD} is the irradiated power in W. Due to the short pulse, discharges are still evolving and dW/dt can be significant.

The formula used to calculate the energy confinement time is shown here:

$$\tau_e = \frac{W_k}{I_p V_{loop} - \frac{dW}{dt} - P_{RAD}}, \tag{3.10}$$

where W_k is the total kinetic energy in J.

3.3.2 ShapeFIT

A fast boundary reconstruction code has been recently developed for Pegasus plasmas. This code is used to provide shape information without an equilibrium reconstruction. It will be briefly described here, but more detail can be found in upcoming work by J. Barr [92]. The code is based off of work by C. Everson [93].

ShapeFIT treats the plasma currents as a series of filaments (> 4.) It is coupled to a wall current filament model and constrained by external magnetic measurements. To date, reasonable agreement has been found between KFIT equilibrium reconstructions and ShapeFIT, as shown in

Fig. 3.25. ShapeFIT calculates the geometric center R, center vertical position Z, minor radius a, elongation κ, triangularity δ, and aspect ratio A every 0.1 ms.

ShapeFIT has been instrumental in this work for determining the shape, line-averaged density, and toroidal field for many limited discharges in the L-H power threshold studies.

3.4 Pegasus H-mode Operational Space

The main parameters that determine whether or not H-mode is accessed, discussed in Chapter 2, are density, toroidal field, shape, geometry, working gas, power, wall-cleanliness, and fueling location.

The range of accessible density on Pegasus using HFS fueling is shown in Fig. 3.26. Density can be varied from $5 \times 10^{18} m^{-3}$ to $5 \times 10^{19} m^{-3}$, with $n_G \gtrsim 0.8$ possible. For the majority of these experiments, the current in the toroidal field was held constant at 288 kA-Turns, which usually equates to a field of ~ 0.16 T on-axis. Limited and diverted magnetic topologies are possible on Pegasus, as demonstrated by the equilibrium reconstructions of Pegasus plasmas in Fig. 3.27. The limited plasma is limited on the centerstack and the diverted plasma is in the upper single null direction. Deuterium was used as the working gas for these experiments.

The effect of the first six factors on the power threshold can be understood by using an empirical power threshold scaling, such as the ITPA04 (Equation 2.4) and ITPA08 (Equation 2.1) scalings. The power threshold predicted by the high-A ITPA08 scaling and the range predicted by the aspect ratio dependent ITPA04 empirical scaling is shown in Fig. 3.28 for Pegasus deuterium discharges with plasma currents up to 0.2 MA. The plasma parameters used to determine these scalings are: $R = 0.35$ m, $A = 1.19$, $B_T = 0.165$ T, $\kappa = 2$, and $n_G = 0.5$. At a typical operating $I_p \sim 100$ kA, the required power predicted for H-mode access is ~ 20 kW and ~ 53 kW for the ITPA08 and ITPA04 scalings, respectively. The available Ohmic input power is also shown in Fig. 3.28 for Pegasus. Typically, Pegasus has $\sim 10-20\times$ more power available than predicted as necessary to achieve H-mode by the ITPA08 scaling.

The Ohmic power is varied by directly changing the loop voltage waveform or indirectly the plasma current (plasma current is affected by both the loop voltage and poloidal induction.) An example of different loop voltages, plasma currents, and total Ohmic input power is shown in Fig.

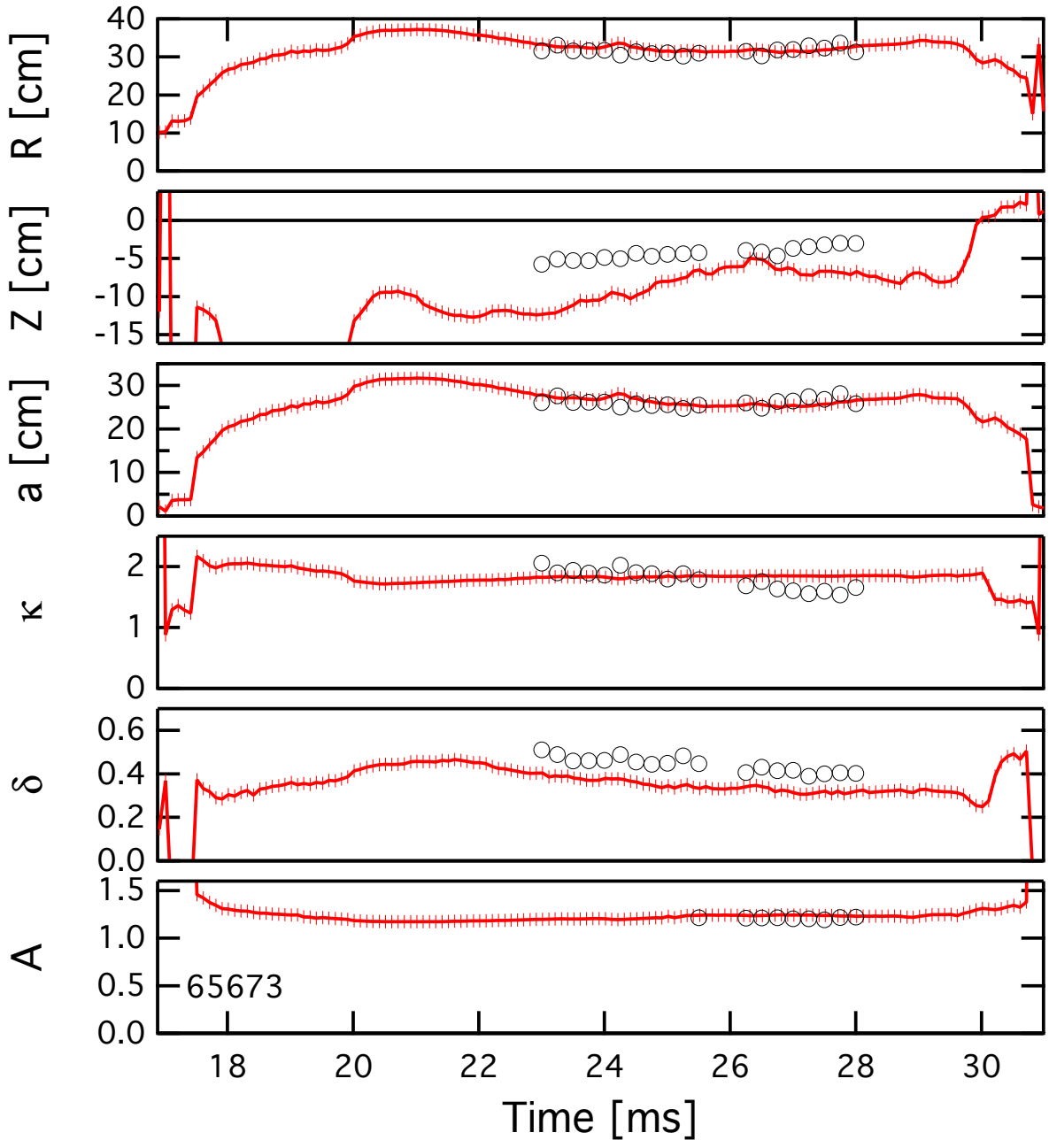

Figure 3.25: ShapeFIT shaping parameters (in red) compared to KFIT reconstructions (black circles)

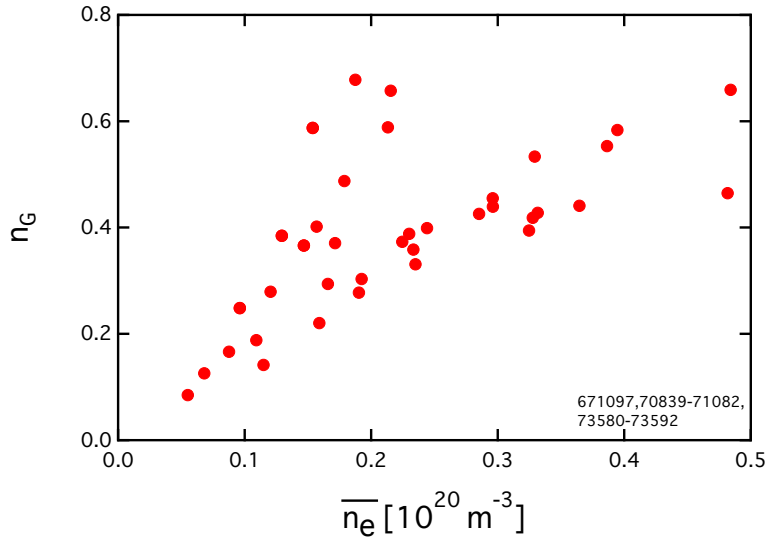

Figure 3.26: HFS-fueling density operational space

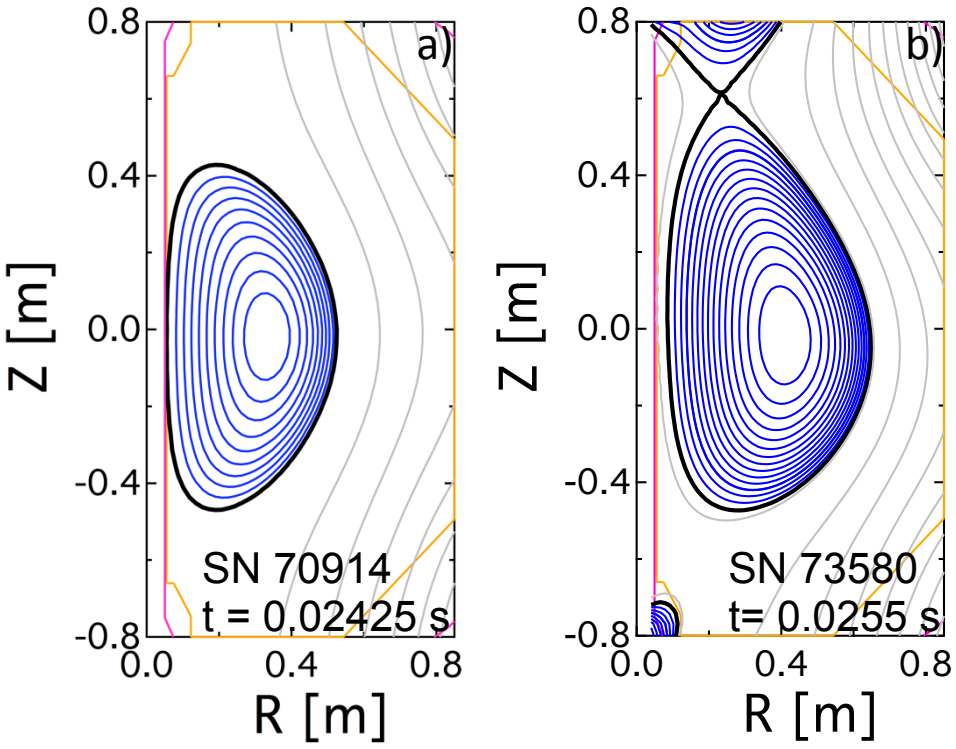

Figure 3.27: Flux plots of reconstructed limited (a) and diverted (b) Pegasus plasmas

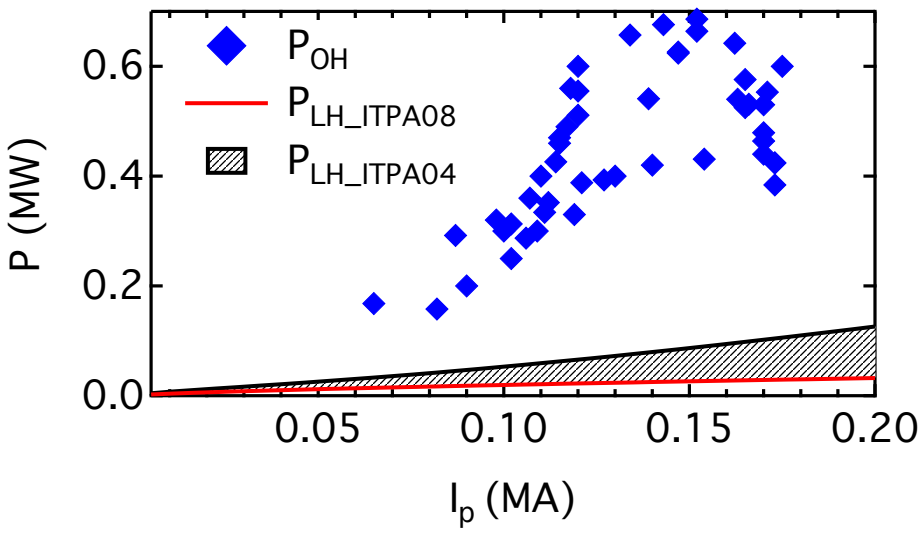

Figure 3.28: Power Predicted for H-mode Access on Pegasus by the ITPA08 scaling (in red) and the ITPA04 scaling (black shaded region) and the actual Ohmic input power (blue diamonds)

3.29. The plasma current achieved by Ohmic power alone is up to ∼150 kA. The total Ohmic input power is varied from 0.2 to 0.6 MW. The various toroidal fluxes for these discharges are also shown.

The use of titanium gettering, the separation of the plasma from the outer wall and short pulses allow Pegasus to routinely achieve UHV in between discharges. Previous work [94] studied the presence of impurities in the plasma and the wall recycling. Impurity levels, determined from SPRED spectra, in Ohmic discharges are low and dominated by oxygen and deuterium lines. The effective particle charge, Z_{eff}, is estimated to be ~ 1. The recycling coefficient is estimated to be less than 0.7.

Pegasus has both LFS and HFS fueling systems available. A comparison of the outboard neutral pressure in similar LFS-fueled and HFS-fueled discharges is shown in Fig. 3.7. As shown by the figure, the use of HFS fueling on Pegasus leads to a substantial drop in the neutral pressure during the plasma discharge at similarly achieved density.

Similar to other spherical tokamaks, the use of HFS fueling is critical to achieving H-mode on Pegasus. Even though sufficient power is available on Pegasus to access H-mode, LFS-fueled plasmas remain in L-mode. However, at the same power levels, HFS-fueled plasmas with little

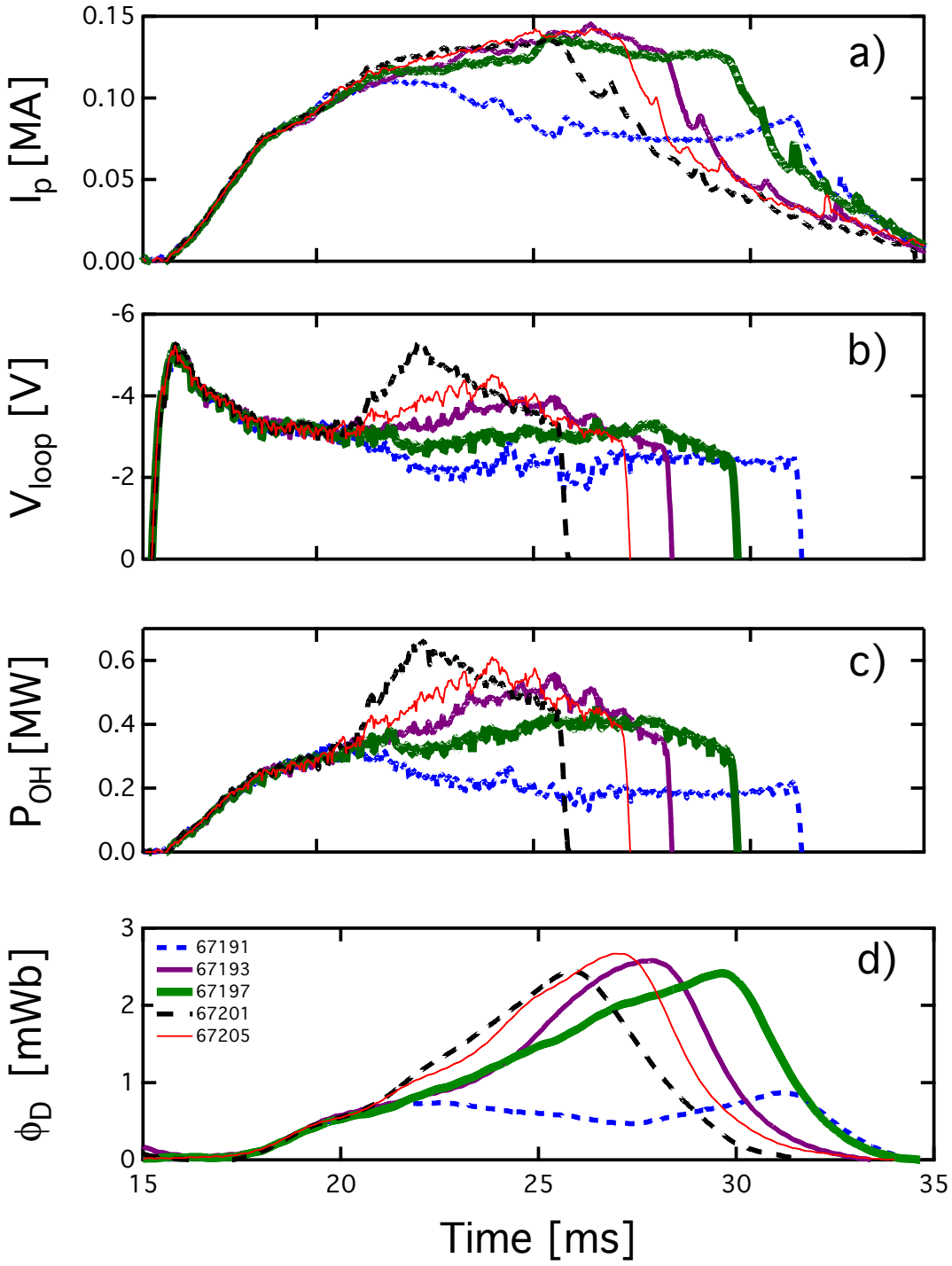

Figure 3.29: Pegasus P_{OH} operational space. I_p (a), V_{loop} (b), P_{OH} (c), and Φ_D (d)

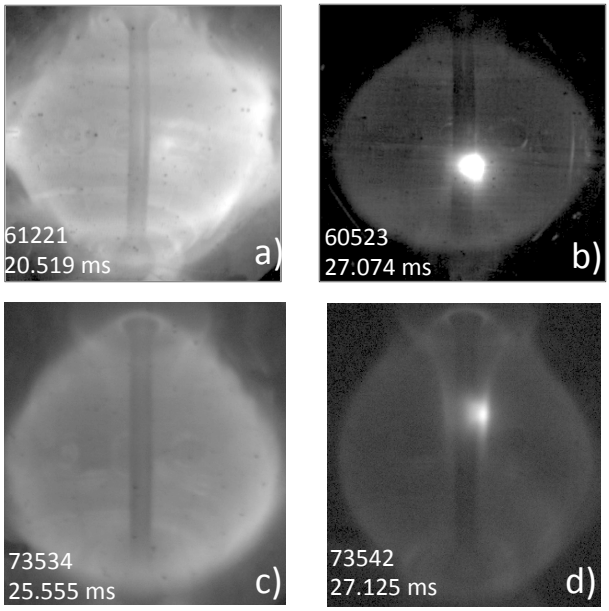

Figure 3.30: Fast camera images of limited Pegasus LFS-fueled L-mode (a) and HFS-fueled H-mode (b) and diverted LFS L-mode (c) and HFS-fueled H-mode (d) plasmas

or no LFS fueling access H-mode. A comparison of two limited discharges and two diverted discharges with these two fueling methods is shown in Fig. 3.30. The LFS-fueled plasmas remain in L-mode and have a bright, turbulent edge, whereas the HFS-fueled plasmas access H-mode. This plasma is characterized by a quiescent edge and a drop in the total signal. These four images are at the same contrast with an exposure time of 30 μs.

Chapter 4

H-mode at Near-Unity Aspect Ratio

This chapter details the first documentation of the H-mode confinement regime at near-unity aspect ratio $A \lesssim 1.2$ on the Pegasus Toroidal Experiment. Specifically, this work has three main components: 1) describing the general characteristics of H-mode plasmas and how they differ from L-mode plasmas; 2) describing the H-mode operational space, including the power threshold; and 3) describing the ELM characteristics and dynamics observed on Pegasus. This chapter discusses each of these components in detail.

4.1 H-mode Characteristics

The H-mode regime is routinely accessed on Pegasus at $A \lesssim 1.2$ using only Ohmic heating via HFS fueling and low edge recycling in both limited and diverted magnetic topologies. H-mode plasmas are easily distinguished from L-mode plasmas by a variety of hallmarks. Many of these H-mode characteristics are observed elsewhere, as described in Chapter 2. The features that define H-mode plasmas on Pegasus are discussed here; they include: formation of a quiescent edge, improvement in energy confinement, heating of electron and ion channels, increase of intrinsic toroidal rotation, and development of edge pedestals.

At the H-mode transition, a sharp and quiescent edge is formed. This standard H-mode signature is illustrated by the fast camera imaging in Fig. 3.30 of L-mode and H-mode plasmas. L-mode plasmas have a noisy turbulent edge, whereas H-mode plasmas have a quiescent edge and a drop in total visible emissions compared to L-mode plasmas, since D_α dominates visible emissions, as shown in Fig. 3.19.

The transition from a turbulent L-mode edge to a quiescent H-mode edge is observed in < 1 ms on the fast camera. An image time sequence of the L-H transition on Pegasus is shown in Fig. 4.1. These images are displayed at the same contrast levels. This image time sequence begins with a noisy and turbulent L-mode edge and a bright L-mode plasma. In the next image, the HFS fueler on the centerstack is engaged. Soon after HFS fueling initiation, a sharp edge begins to form and the visible emissions decrease. Finally, a complete quiescent H-mode edge exists. The visible emissions have dropped significantly from the last H-mode camera image compared to the first L-mode image. This quiescent H-mode edge is also observed in the development of edge pedestals in the current and pressure, which will be described later in this section.

Figure 4.2 compares features of limited L-mode and H-mode discharges at $A \lesssim 1.2$. The L- and H-mode discharges have comparable $I_p \sim 0.1$ MA [Fig. 4.2(a)]. These discharges utilized the same field pre-programming. The divergence in plasma current between these discharges is due to the difference in fueling and their resulting performance.

These two discharges varied only by fueling method, as shown by their fueling programming in Fig. 4.3. In both cases, LFS fueling is used for breakdown and during the plasma current ramp up. At the beginning of the plasma current flattop, the discharges bifurcate with the L-mode plasma remaining fueled from the LFS. LFS fueling is halted in the soon-to be-H-mode case. Next ~ 2 ms later, HFS neutral fueling is engaged in that discharge. At the initiation of HFS fueling, a L-H transition occurs.

In order to induce an H-mode transition on Pegasus, the plasma neutral fueling must be closely managed. Too much LFS fueling prevents or delays an H-mode transition, even with the HFS fueler activated. A time lag between the termination of the LFS fueling and introduction of the HFS fueling is necessary to induce a prompt transition, otherwise the transition is deferred or prohibited.

The difference in outboard neutral pressure with these two fueling methods is illustrated in Fig. 3.16 for these two discharges. The LFS-fueled discharge has an outboard neutral pressure of $3-4$ mTorr throughout the discharge. At the initiation of HFS fueling, the HFS-fueled discharge's outboard neutral pressure diverges from the LFS-fueled case and eventually achieves < 2 mTorr. Ultimately, the HFS-fueled H-mode discharge has an $\sim 2\times$ decrease in outboard neutral pressure

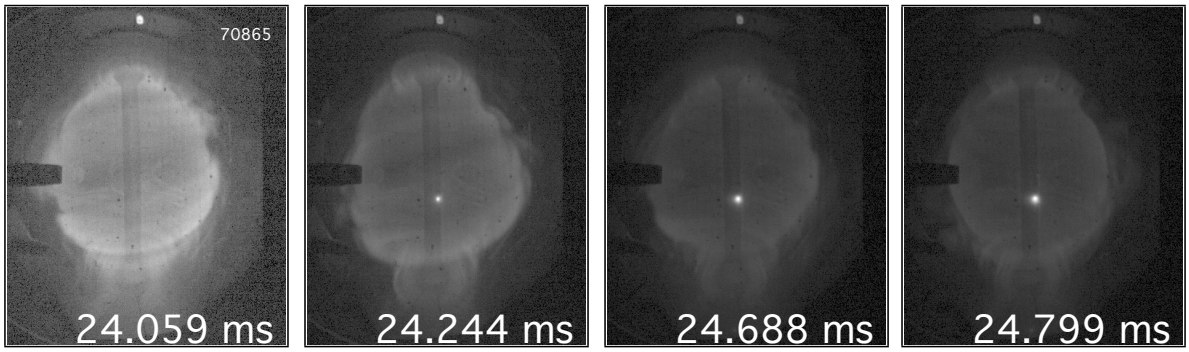

Figure 4.1: Fast camera time series of an L-H transition on Pegasus

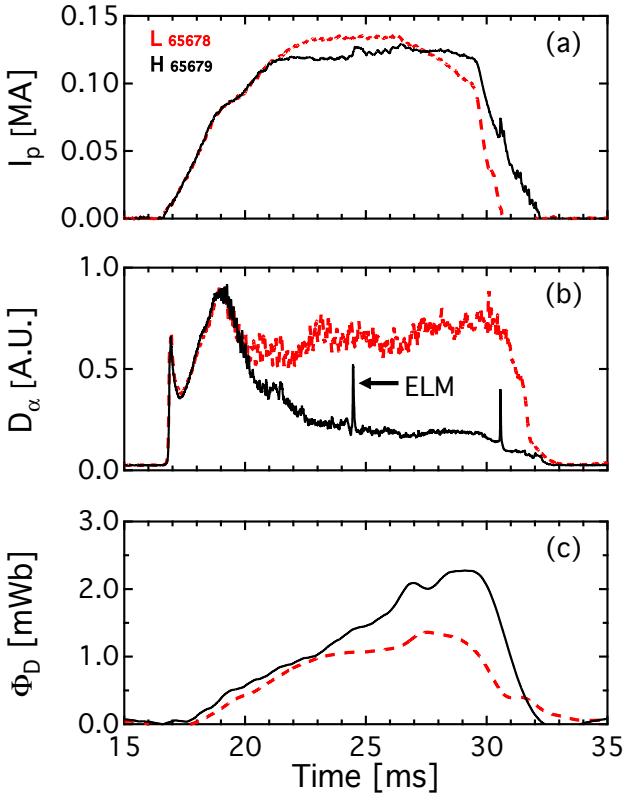

Figure 4.2: I_p (a), D_α signal (b), Φ_D of limited H-mode (black) and L-mode (red) discharges

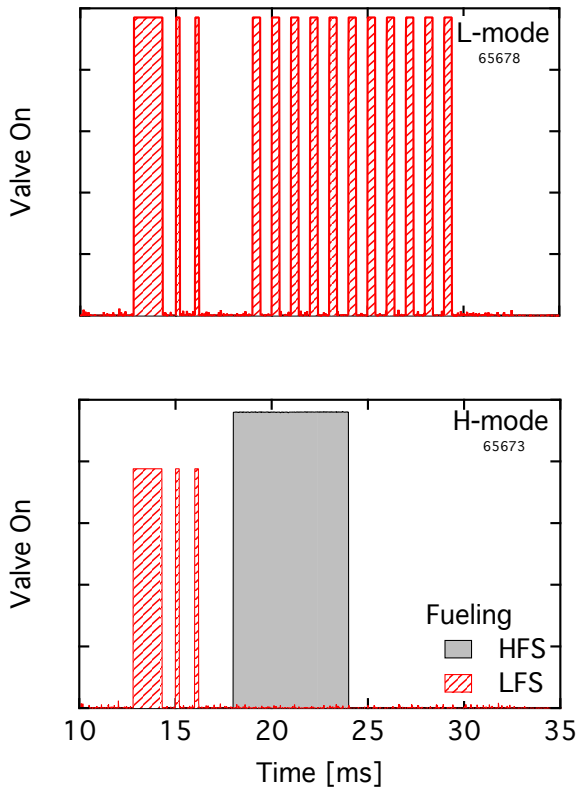

Figure 4.3: Fueling programming for Figure 4.2 discharges

compared to the LFS-fueled L-mode discharge. Thus, HFS fueling lowers the outboard neutral pressure compared to LFS fueling, which allows an H-mode transition to occur. The reduction in edge LFS neutrals presumably permits the edge temperature to rise, probably initiating the transition.

The plasmas had comparable density ($\bar{n}_e \sim 1 \times 10^{19}$ m^{-3}) and shape ($A \approx 1.22$, $\kappa \approx 2.4$, $\delta \approx 0.57$) at the time of the L–H transition, at ~20 ms. The transition to H-mode is indicated in Fig. 4.2(b) when D_α emissions drop and in Fig. 4.2(c) by the diamagnetic loop toroidal flux Φ_D diverging from $\Phi_D \sim 1$ mWb (L-mode) to $\Phi_D \geq 2$ mWb (H-mode). Another example of the bifurcation in Φ_D between L-mode and H-mode plasmas is shown in Fig. 3.29. In this figure, the lowest input power discharge remains in L-mode and has $\Phi_D \sim 1$, whereas the other four discharges all have H-mode transitions and achieve $\Phi_D \geq 2$. Values of Φ_D up to 4 mWb have been

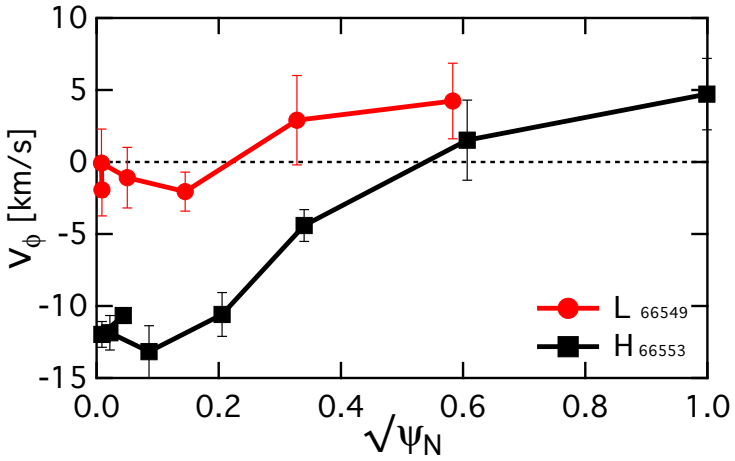

Figure 4.4: Radial intrinsic toroidal rotation profile for Figure 4.2 discharges

observed in H-mode plasmas, while L-mode values are typically $\Phi_D \lesssim 1.5$ mWb. A prominent spike in the H-mode D_α signal accompanies a large (Type I) ELM.

The intrinsic toroidal rotation profiles for the discharges in Fig. 4.2 was measured throughout the discharges using passive ion spectroscopy. Since these are Ohmic-only plasmas, they have no external momentum input. The spectrometer's tangential views were chordally-integrated to determine the intrinsic rotation at each spatial location. At each spatial location, the rotation was determined by using Equation 3.3. An OV emission line ($\lambda = 278.101$ nm) was used to measure the shift in the central wavelength between each tangential view and a radial chord. The rotation at each location was averaged from $27 - 28$ ms.

The toroidal rotation profiles for these two discharges are shown in Fig. 4.4 normalized to the polodial flux surfaces. The L-mode discharge has negligible toroidal rotation from $\sqrt{\psi_N} \lesssim 0.6$. Its edge toroidal rotation is unknown, since OV emissions are not observed in the edge probably due to a lower electron temperature. In contrast, the H-mode core plasma is rotating strongly in the counter-current direction with a speed of ~ 10 km/s. The toroidal rotation decreases away from the core plasma and is negligible in the edge. Thus, H-mode plasmas have increased intrinsic core rotation compared to L-mode plasmas.

By operating at near-unity aspect ratio, Pegasus has unique diagnostic access to the H-mode pedestal due to its low electron temperatures and short pulse lengths. The low electron temperatures are a result of the low required B_T at low aspect ratio. Detailed edge probe scans can provide radial profiles with both high spatial and temporal resolution. To date, the radial pressure and current edge profiles have been measured using insertable probes in limited L-mode and H-mode discharges. A camera image of a probe inserted into the edge of a Pegasus plasma is shown in Fig. 4.5.

The current profile was observed for the L-mode and H-mode discharges in Fig. 4.2 at 28 ms. A pronounced J_{edge} pedestal was measured in H-mode plasmas between ELMs using an array of shielded Hall effect sensors inserted into the edge plasma at $Z = 0$ cm. The internal B_Z probe measurements are shown in Fig. 4.6(a) with the corresponding derived J_{edge} profile [Fig. 4.6(b)] from Equation 3.5 in lab space. The nominal pedestal width contracts to $\sim$2 cm in the H-phase, from approximately double that in the L-phase.

Initial measurements of an H-mode pressure pedestal were obtained from multi-shot radial scans of an insertable triple Langmuir probe at $Z = 0$ cm. The plasmas were scanned from the scrape-off-layer to the top of the pedestal. The plasma currents for the L-mode and H-mode discharges that were used as target discharges for this scan are shown in Fig. 4.7. The two shots had comparable plasma currents of $\sim$ 100 kA, with the main difference between the discharges being the location of neutral fueling. The L-mode plasma was fueled exclusively from the LFS and the H-mode plasma was exclusively fueled from the HFS. The transition from L-mode to H-mode occurs at $\sim$ 20 ms.

Measurement of the edge pressure profile were complicated in these L-mode and H-mode discharges by the presence of a large scale low-m/n=1 tearing mode. This tearing mode was present at low frequencies of $5-30$ kHz, as shown in a magnetic fluctuation autopower spectrum of single Mirnov probe sensor in Fig. 4.8. The dominant mode was identified as $n = 1$ by performing a cross-phase spectral analysis of the measured signals from the high-n toroidal probe array (P8 probe) sensors. The n= 2 and $n = 3$ peaks in the autopower spectrum were harmonics of the original mode and occurred at double and triple the $n = 1$ frequency. Their mode numbers were also identified by performing a cross-phase spectral analysis.

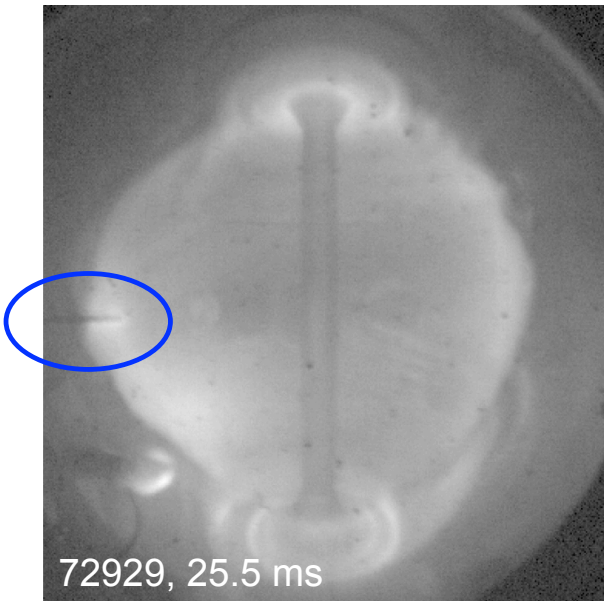

Figure 4.5: Camera image of probe inserted into Pegasus edge plasma

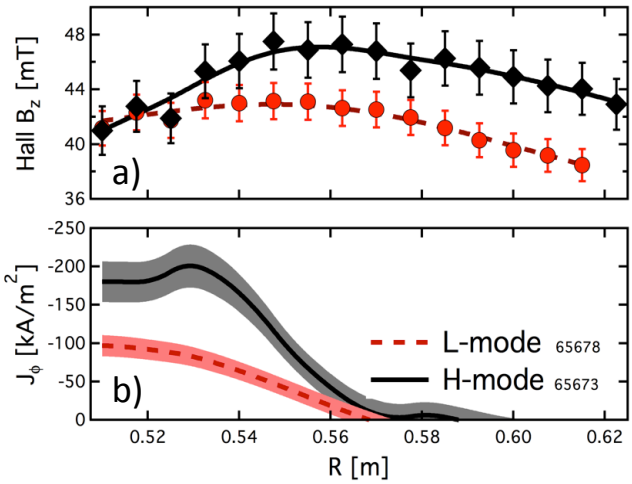

Figure 4.6: Pedestal formation in H-mode. Measured $B_Z(R)$ (a) and inferred $J_\phi(R)$ (b) in lab space for H-mode (solid, diamonds) and L-mode (dashed, circles) plasmas.

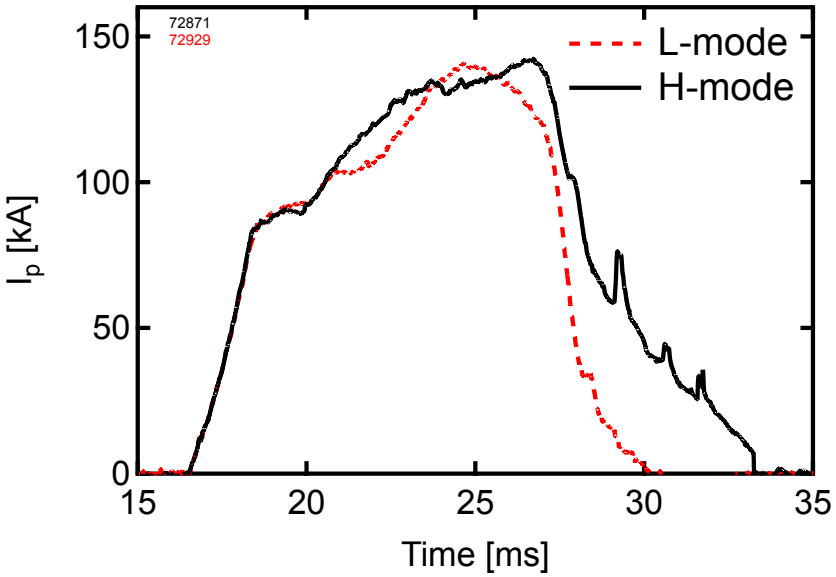

Figure 4.7: I_p for L-mode and H-mode discharges used in the Langmuir probe scan

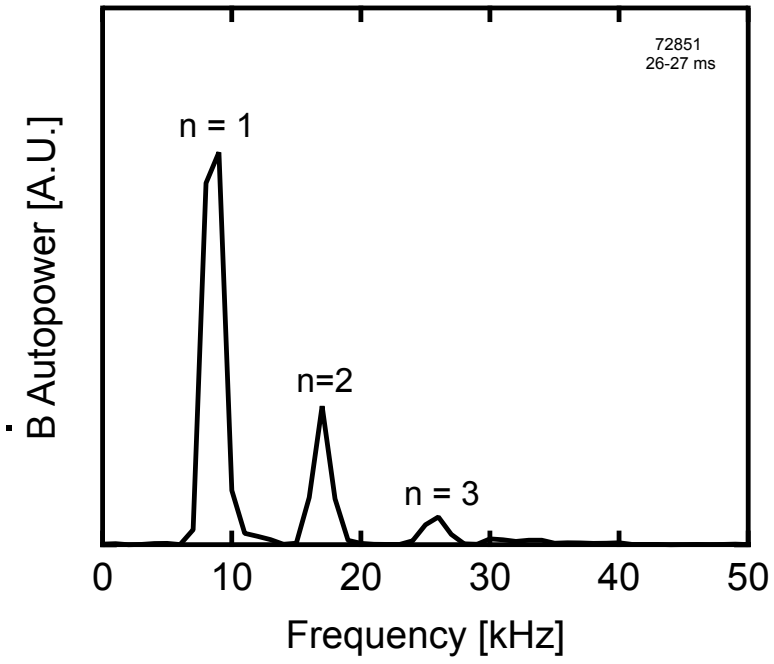

Figure 4.8: Magnetic fluctuation autopower spectrum and toroidal mode numbers for Figure 4.7 discharges

The very large internal tearing mode caused the plasma edge to move by several centimeters every ~ 100 μs, in phase with the MHD signal, as demonstrated in Fig. 4.9. This figure shows the high phase and low phase of the $\dot{B}$ signal, when the plasma expands and contracts, respectively. Not unexpectedly, the pressure profile also oscillates in phase with the MHD, as shown in Fig. 4.10. To account for this oscillation in the pressure measurements, the pressure profile was measured at a constant phase of the MHD signal from $26-27$ ms. Practically, the pressure at a given radial location was determined by averaging the valleys in the pressure measurement during this time period. An example of this technique is illustrated by the blue line in Fig. 4.10. This analysis technique was performed at each radial location for both the L-mode and H-mode discharge, creating a radial pressure profile for both discharge types.

These radial edge pressure profiles for the L-mode and H-mode discharges are shown in Fig. 4.11. The L-mode profile is best fit bilinearly, whereas the H-mode profile is best fit using a conventional modified hyperbolic tangent profile [95]. This data indicates a comparable pressure scale length of ~ 2 cm in these H-mode plasmas, which is consistent with the current scale length.

Ohmic H-mode operations are compatible with local helicity injection startup. An example of the evolution of this discharge type is shown in Fig. 4.12. In this discharge, local helicity injection with a bias current of 4.5 kA created an $I_p = 120$ kA startup plasma. This was successfully coupled to subsequent Ohmic drive. The HFS fueler was first engaged during the helicity phase of this discharge. Thus, when the Ohmic drive was initiated, the discharge immediately transitioned into H-mode. An equilibrium reconstruction during the H-phase of this discharge is also shown in this figure. This high-performing H-mode discharge achieved $I_p \sim 170$ kA and $W \sim 2.1$ kJ at the end of the discharge.

4.1.1 Energy Confinement and Heating

Energy confinement time is an important metric that defines the quality of a discharge. It can be calculated in a variety of ways, most accurately through time-evolving equilibrium reconstructions or a "Virial Analysis" as described in the Appendix. However, performing time-evolving reconstructions on Pegasus is nontrivial and time intensive, as discussed in Chapter 3.

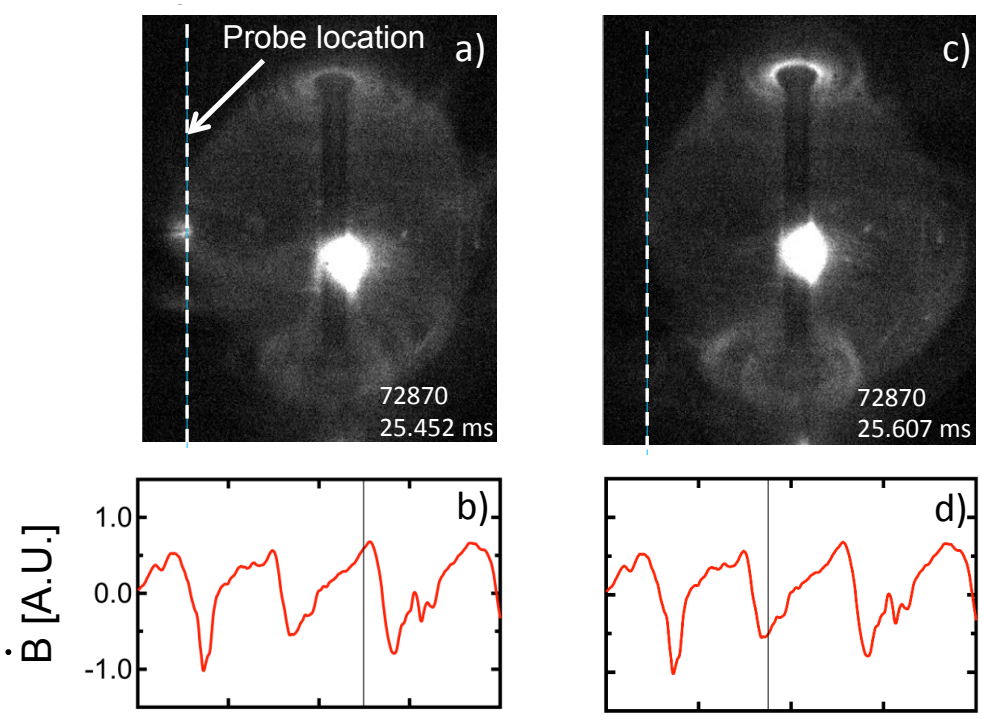

Figure 4.9: Plasma edge motion correlated with internal tearing mode activity. (a): Plasma edge expansion correlates with peak in $\dot{B}$ signal (b); (c) Plasma contraction correlates with valley in $\dot{B}$ signal (d)

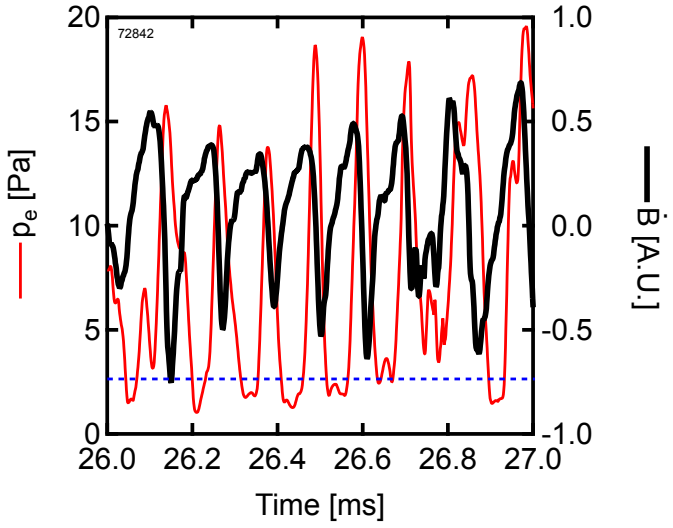

Figure 4.10: MHD signal correlated with edge pressure measurements from Langmuir probe

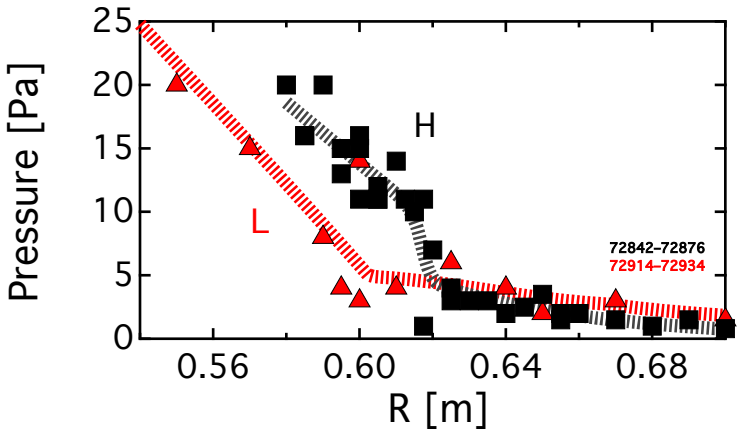

Figure 4.11: Radial edge pressure profile for Figure 4.7 discharges

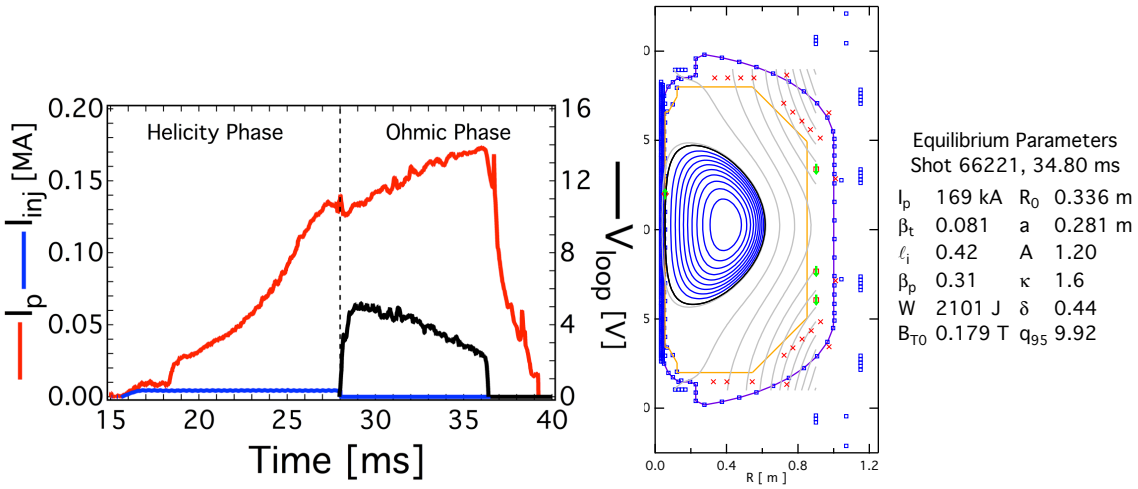

Figure 4.12: Left: Plasma current evolution of local helicity injection startup to subsequent Ohmic drive discharge; Right: H-mode equilibrium reconstruction during H-phase of discharge

Several discharges have been analyzed for time-evolving reconstructions for ≥ 3 milliseconds. A variety of Ohmic discharges were reconstructed, including: limited, diverted, L-mode, H-mode, and local helicity injection initiated startup. The energy confinement time of these discharges was calculated at the end of the I_p flattop, if possible, to allow the discharge as much time as possible to evolve. Due to the short pulse lengths, these discharges are not in transport equilibrium by the end of the discharge. Since the plasma energy typically increases throughout the discharge, as demonstrated in Fig. 3.24, measuring the energy confinement time at the end of the discharge provides the highest τ_e.

The energy confinement time in these discharges is calculated using Equation 3.10. The power radiated in these plasmas is assumed to be zero based on previous work [94]. Thus, to determine energy confinement time, Equation 3.10 reduces to

$$\tau_e = \frac{W_k}{I_p V_{loop} - \frac{dW}{dt}}. \tag{4.1}$$

Reconstructions are then needed to calculate W_k and dW/dt.

Examples of L and H reconstructions of a diverted discharge are given in Fig. 4.13. The plasmas had comparable plasma currents of $80-90$ kA and shape ($R \sim 0.35$ m, $\kappa \sim 1.8$, $\delta = 0.44$.) However, many differences are observed between these two time points. The H-phase reconstruction has a higher pressure than the L-phase. The total stored energy is also higher during the H-phase. The H-mode plasma has reduced heating power, $P_H = P_{OH} - dW/dt$, due to the higher dW/dt during the H-phase. During the H-phase the current profile is more peaked, represented by the change in l_i from 0.41 to 0.63.

To understand the change in the current profile between L-mode and H-mode plasmas, a predictive KFIT study was conducted. The plasma used in this study is shown in Fig. 4.14(a). The first part of the study held W_k constant and varied W_m. The value of Φ_D increased with W_m and l_i, as shown in Fig. 4.14(b). The current profiles for the equilibria in Fig. 4.14(b) are shown in Fig. 4.14(c). Thus, the increasing paramagnetism observed in Pegasus H-mode plasmas as compared to L-mode plasmas is indicative of the current profile evolving and becoming more peaked. The second part of the study held W_m constant and varied W_k, as shown in Fig. 4.14(d). As expected, increasing W_k decreases Φ_D, making the plasma more diamagnetic.

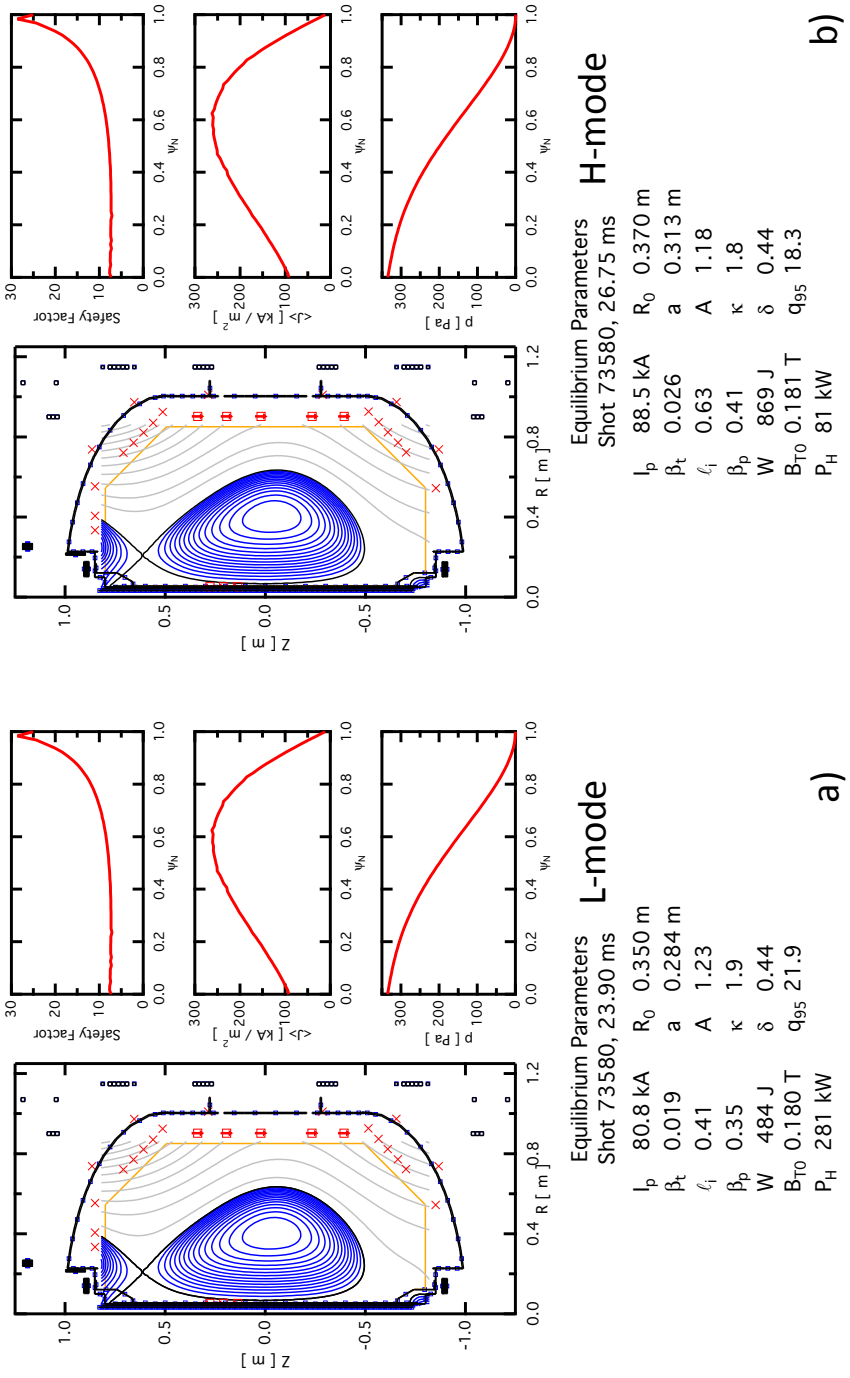

Figure 4.13: Reconstruction outputs of L-phase (a) and H-phase (b) of discharge 73580

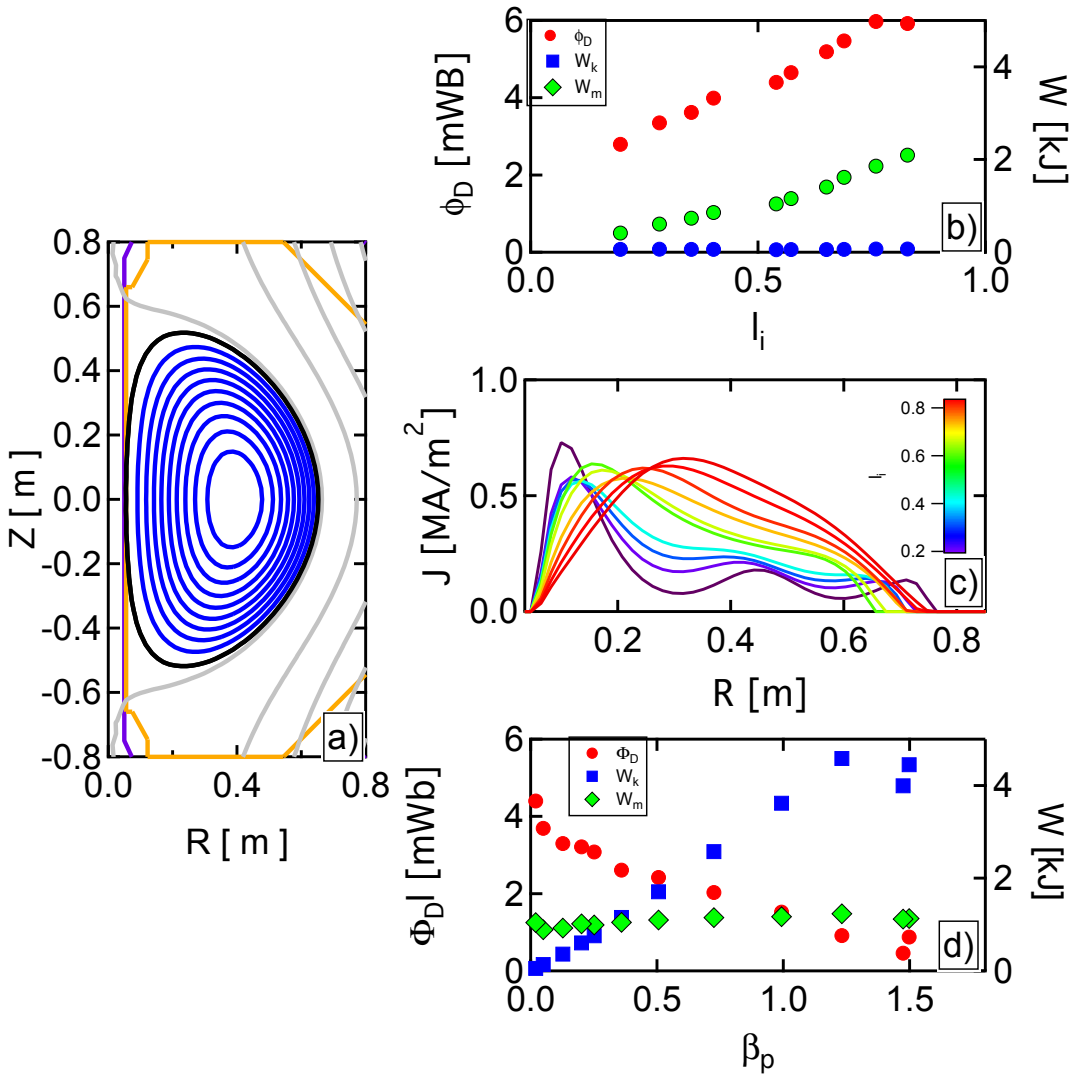

Figure 4.14: Model equilibrium study of varying W_k and W_m . (a): Flux plot; (b): Varying W_m and holding W_k constant; (c): current profiles for (b); (d): Varying W_k and holding W_m constant

The magnetic measurements used to constrain these Grad-Shafranov equilibria in Fig. 4.13 are denoted by the red markers in that figure's flux plot. 31 measurement constraints were used in these discharges. The plasma current, non-core flux loops, wall loops, midplane sensors (PDX5-PDX9), toroidal flux signal and three centerstack poloidal mirnov sensors (HighRes) are all utilized for these reconstructions. A constraint on divertedness was also enabled. The chi square and measurement fits for these plasmas is illustrated in Fig. 4.15 for these plasmas. The majority of the derived measurements agree well with the actual measurements. The highest source of error in these reconstructions is from the midplane sensors and centerstack poloidal sensors. These reconstructions had similar low chi squares, with $\chi_N \sim 2$.

The energy confinement time was calculated by performing six time-evolving reconstructions of two L-mode plasmas and four H-mode plasmas. Of the L-mode discharges, one was limited and the other was diverted. Three limited H-mode plasmas and one diverted H-mode plasma were reconstructed. The results of these time-evolving reconstructions for energy confinement are summarized in Table 4.1. The values of W_k, dW/dt, and P_{OH} were averaged over the time frame specified in the table for each discharge. The Ohmic input power for these discharges is $250-500$ kW. The corrected input power P_H was used to calculate both τ_e and $\tau_{e,98pby2}$ via Equation 3.10 and Equation 2.27, respectively. The dW/dt corrections to the input power are non-negligible and can be a significant portion of the total input power, particularly in H-mode discharges. This correction varies for each discharge, so it must be individually determined. The input power is usually decreased by dW/dt, except in the limited L-mode (65678) discharge where the energy confinement time is calculated during an I_p ramp down. For the H-mode discharges with a positive dW/dt, dW/dt ranges from 0.03–0.7 of P_{OH} with $< dW/dt >= (0.48 \pm 0.18) P_{OH}$.

Since the properties of these plasmas differed, the energy confinement is best described by comparison to the H_{98} factor. A summary of the H_{98} factors for these discharges is given in Fig. 4.16. The average H_{98} factor for L-mode plasmas is 0.5 ± 0.2. Their average H_{98} factor is 1.0 ± 0.2. H-mode discharges at $A \lesssim 1.2$ therefore show a confinement improvement of at least approximately double that of L-mode plasmas, similar to other ATs and STs [26].

The confinement improvement in H-mode is comparable for both limited and diverted magnetic configurations on Pegasus. Since the discharges have τ_e evolving throughout their relatively short

a)

Show Measurement Fits

Measurement	Value	Fit	StdDev, %	Chi Sq
Ip	82116	80804	2	0.63755
fluxloop2	-0.0018539	-0.00199	3	0.074118
fluxloop3	0.0043355	0.0043032	3	0.0041524
fluxloop5	0.026482	0.026723	3	0.091845
fluxloop6	0.065257	0.063081	3	1.2349
fluxloop7	0.07322	0.072583	3	0.084195
fluxloop8	0.083519	0.081125	3	0.91301
fluxloop9	0.088683	0.087244	3	0.29244
fluxloop10	0.095908	0.092392	3	1.4933
fluxloop11	0.063413	0.06203	3	0.52854
fluxloop12	0.064324	0.060565	3	3.7939
fluxloop13	0.059308	0.057324	3	1.2439
fluxloop14	0.056681	0.053594	3	3.2959
fluxloop15	0.051615	0.049017	3	2.816
fluxloop16	0.030608	0.031702	3	1.4209
wallloop1	0.076221	0.07371	3	1.2064
wallloop2	0.13984	0.13983	3	1.7685e-05
wallloop3	0.059337	0.06037	3	0.33699
wallloop4	0.042086	0.043604	3	1.4445
wallloop5	0.091083	0.090674	3	0.022377
wallloop6	0.057711	0.060742	3	3.0653
PDX05	0.022495	0.021457	5	0.85158
PDX06	0.013858	0.01615	5	10.945
PDX07	0.014457	0.014773	5	0.19112
PDX08	0.014225	0.01359	5	0.79683
PDX09	0.016229	0.01613	5	0.01466
diamag	0.0007215	0.0007612	3	3.3632
HighRes07	0.057202	0.0454	5	17.026
HighRes08	0.060487	0.053515	5	5.315
HighRes09	0.061125	0.058191	5	0.92122
IsDiverted?	1	1	1	0

Update Close Total: 63.424

b)

Show Measurement Fits

Measurement	Value	Fit	StdDev, %	Chi Sq
Ip	90282	88476	2	1.0003
fluxloop2	0.0027002	0.002956	3	0.26176
fluxloop3	0.0078526	0.0079457	3	0.034669
fluxloop5	0.030269	0.029776	3	0.29428
fluxloop6	0.073298	0.070673	3	1.4247
fluxloop7	0.082401	0.081592	3	0.10709
fluxloop8	0.094303	0.091454	3	1.0145
fluxloop9	0.10078	0.098393	3	0.62155
fluxloop10	0.11037	0.1034	3	4.426
fluxloop11	0.075166	0.072957	3	0.96029
fluxloop12	0.075067	0.071433	3	2.6039
fluxloop13	0.068703	0.067515	3	0.33192
fluxloop14	0.065533	0.062948	3	1.7292
fluxloop15	0.059934	0.057595	3	1.6923
fluxloop16	0.038501	0.038519	3	0.00024318
wallloop1	0.082574	0.079967	3	1.1074
wallloop2	0.15303	0.15759	3	0.9888
wallloop3	0.080288	0.078605	3	0.48825
wallloop4	0.062226	0.063445	3	0.4265
wallloop5	0.10102	0.10671	3	3.5246
wallloop6	0.064897	0.06942	3	5.3969
PDX05	0.029047	0.02659	5	2.8613
PDX06	0.020868	0.023924	5	8.5799
PDX07	0.021091	0.024388	5	9.7776
PDX08	0.02141	0.0227	5	1.4509
PDX09	0.021584	0.020865	5	0.44405
diamag	0.0011175	0.0011293	3	0.12482
HighRes07	0.05831	0.050512	5	7.1538
HighRes08	0.061936	0.060296	5	0.28022
HighRes09	0.063939	0.070156	5	3.7824
IsDiverted?	1	1	0.5	0

Update Close Total: 62.89

Figure 4.15: KFIT measurement agreement for Fig. 4.13 reconstructions

SN	**Discharge Phase**	**Time** (ms)	P_{OH} (kW)	**dW/dt** (kW)	τ_e (ms)	$\tau_{e,98pby2}$ (ms)	H_{98}
65673	Limited H	26.25–28	383	133	2.05	2.48	0.83
65678	Limited L	26.25–28	400	-189	1.17	1.67	0.7
66221	Limited LHI-OH H	34.6–35.5	489	285	4.27	3.48	1.23
67197	Limited H	26–29	389	119	1.41	2.7	0.52
73580	Diverted L	23.9–25.25	301	20	0.8	2.14	0.37
73580	Diverted H	26.7–28.5	261	180	6.67	4.5	1.48

Table 4.1: Summary of time-evolving reconstructions for energy confinement

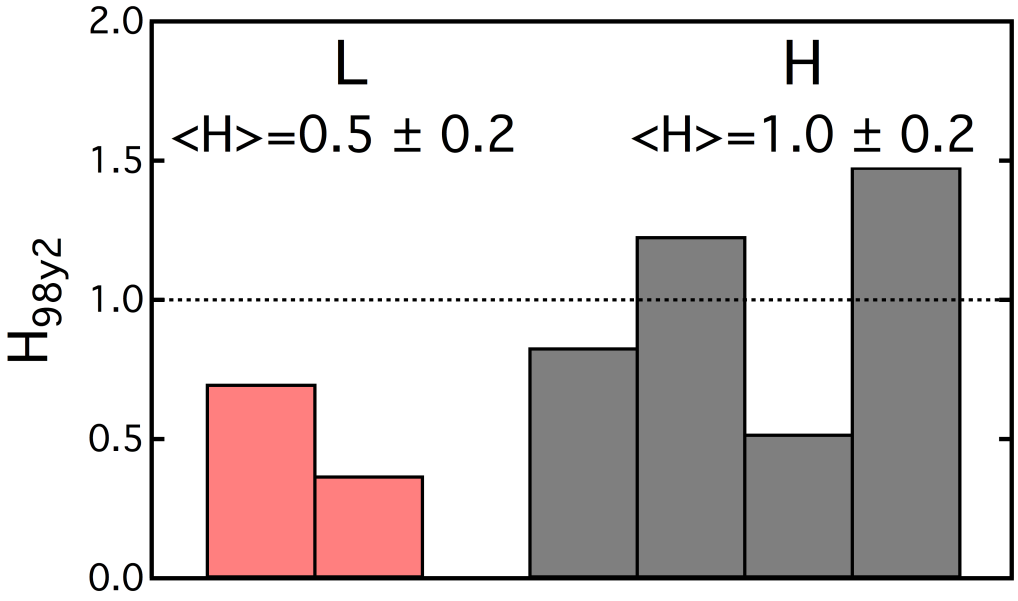

Figure 4.16: H_{98} Summary for L-mode and H-mode discharges

pulse, more precise comparisons of these regimes will be possible when longer pulse plasmas that more closely approach transport equilibrium become available.

Increased core electron and ion heating is seen in H-mode plasmas compared to L-mode plasmas. The ion impurity temperature for the two discharges in Fig. 4.2 was determined from the Doppler broadening of OV and CV impurity lines measured with a passive ion spectrometer. The core ion impurity temperature $T_i(0)$ was calculated throughout these discharges for both spectral lines, as shown in Fig. 4.17 by using Equation 3.2. $T_i(0)$ increases throughout both discharges. However, at the end of these discharges, clear differences in ion impurity temperature are observed with $T_i(0) \sim 40$ eV and $T_i(0) \sim 60$ eV achieved at the end of L-mode and H-mode discharges, respectively. In H-mode, the CV impurity temperature also achieves ~ 60 eV. Thus, the core ion impurity temperature increases between similar L-mode and H-mode discharges.

Increased core electron heating in H-mode is observed in passive ion spectroscopy and Thomson scattering data. CV emission is only observed in H-mode plasmas; L-mode plasmas do not observe CV emission. The presence of CV in H-mode plasmas indicates a higher electron temperature, since CV has a higher ionization potential ($E_i = 392$ eV) than OV ($E_i = 114$ eV). The CV emission increases throughout the evolution of the H-mode discharge, as shown at different

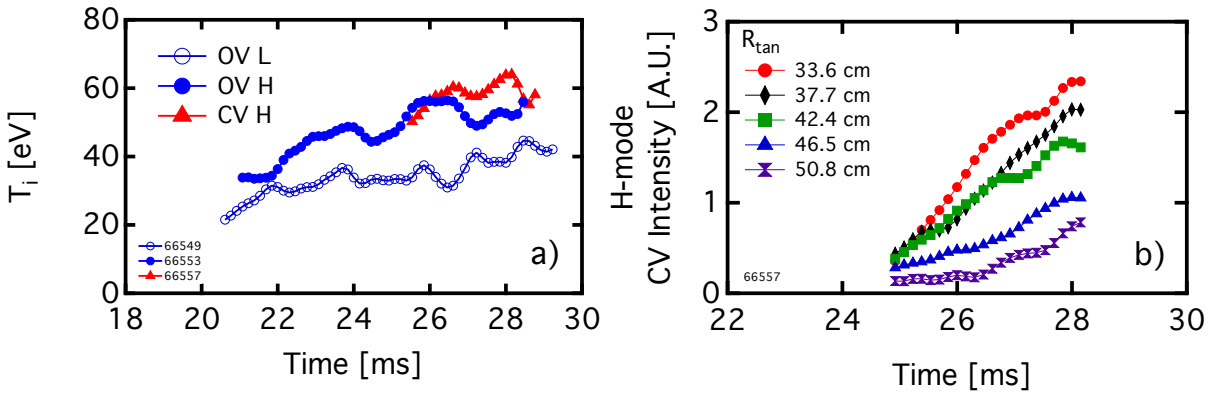

Figure 4.17: Passive ion spectroscopy measurements for Figure 4.2 discharges. (a): Core impurity ion temperature; (b): Tangential H-mode CV intensity with time

tangential radii in Fig. 4.17(b). The emission is peaked near the core (R_{tan} = 33.6 cm.) At the end of the discharge, the emissions have not equilibrated, indicating that the transport equilibrium has not yet been achieved.

Preliminary measurements of the core electron temperature in L-mode and H-mode discharges were obtained using a Thomson scattering system with a low temperature grating installed. These measurements required averaging data from four core spatial points, $\bar{R}_{maj} = 35$ cm, and multiple self-similar discharges. $T_e(0)$ was measured in the limited L-mode and H-mode discharges shown in Fig. 4.18. The discharges achieved similar plasma currents of $I_p \sim 100$ kA and only differed in their fueling location. The two discharges were of similar size and density throughout the discharge. $T_e(0)$ was determined at different time points in each discharge, which are represented by the dashed blue lines in Fig. 4.18.

Figure 4.19 has the measured scattered spectra and their Gaussian fits for the three L-mode time points in Fig. 4.18. The L-mode electron temperature is evolving throughout the discharge. At the beginning of the discharge at 19 ms [Fig. 4.19(a)], $T_e(0) \approx 12$ eV. The core electron temperature increases throughout the discharge, and it achieves ~ 150 eV ten milliseconds later at the discharge termination [Fig. 4.19(c)].

The H-mode electron temperature is also evolving throughout the discharge. At the beginning of the discharge, $T_e(0)$ is the same as in the L-mode discharge [Fig. 4.19(a)]. However, at the end of the H-mode discharge the edge temperature is different than L-mode temperature, as shown

in Fig. 4.19(e). An exact temperature cannot be measured at these H-mode time points. This is due to the decreasing amplitude of the detected signals by $\sim 3\times$ and broadening of the Gaussian spectrum. This makes an accurate Gaussian fit not possible. However, this behavior indicates an increased electron temperature compared to the L-mode discharge, but the low temperature grating is insufficient to make a quantitative measurement. However, the temperature was estimated to be $T_e(0) > 200$ eV at the end of the discharge by comparing the total scattering intensity between the two confinement modes to the analytic, relativistic Thomson scattering model by Selden [96]. Thus, H-mode plasmas have higher core electron temperatures compared to L-mode plasmas. A new high temperature grating has been installed to more accurately measure the H-mode temperatures in the future.

4.2 Power Threshold

These are the first studies of the H-mode power threshold at $A < 1.3$. The L-H power threshold was characterized on Pegasus at $A \lesssim 1.2$ over a wide operational range by varying the plasma density, the Ohmic input power, and the magnetic topology at a nominal $B_T \sim 0.16$ T. As much as possible, experiments were conducted under similar operating conditions to prevent other factors from influencing the power threshold. Exploratory power threshold experiments at a toroidal field of $B_T \sim 0.08$ T were also conducted.

For the experiments characterizing the power threshold with density, power, and geometry, the density was varied from $\bar{n}_e = 0.5 - 5x10^{19}\ m^{-3}$ or $n_G = 0.1 - 0.8$. The Ohmic input power was varied from $200 - 600$ kW. The power threshold was studied in the centerstack limited configuration and the upper single null diverted configuration. An example of these configurations is shown in Fig. 3.27. These diverted plasmas are in the favorable ion ∇B drift direction on Pegasus. This is the conventional topology used for power threshold studies, since it typically has the lowest L-H threshold power. It is also the planned configuration for ITER.

The power threshold was determined at a fixed fueling rate (nominally constant density) by varying the Ohmic input power above and below the power threshold to create discharges that remained in L-mode and ones that transitioned to H-mode. During this sequence of discharges, the external controls on shape and fueling were held constant, if possible. There are two methods

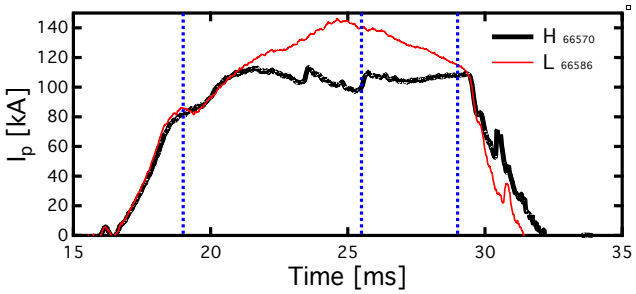

Figure 4.18: I_p for H-mode plasma (in black) and L-mode (in red) used to collect Thomson scattering data. Blue lines represent the time at which data was collected

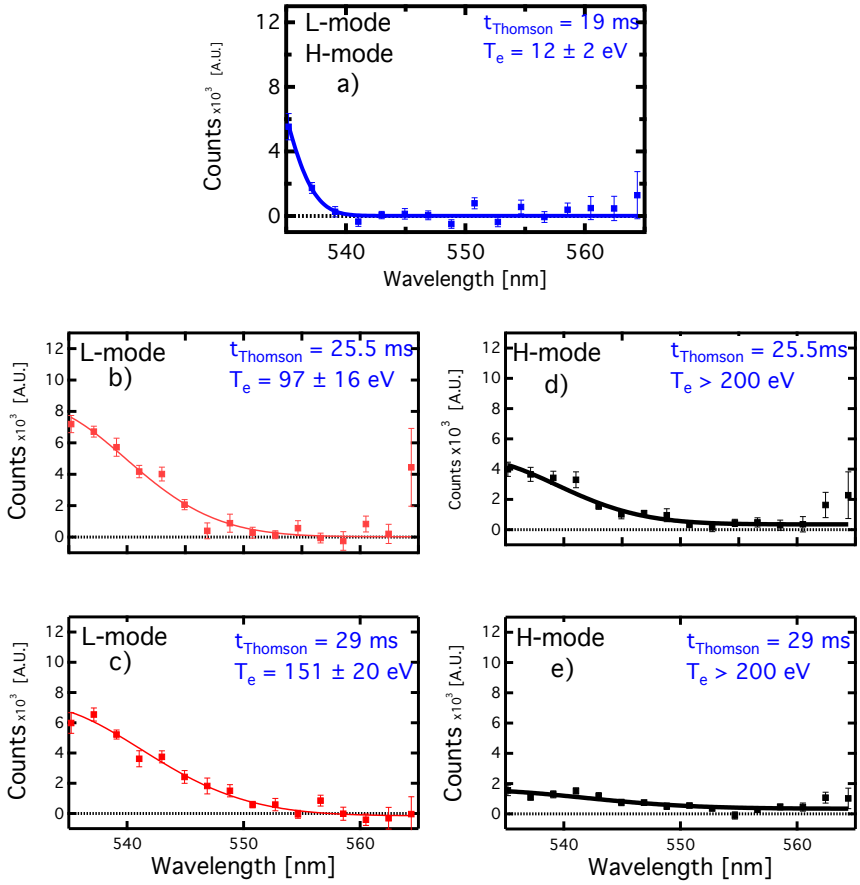

Figure 4.19: Thomson Scattering $T_e(0,t)$ for comparable limited L-mode (a–c) and H-mode (a, d–e) discharges shown in Fig. 4.18

to control the input power at a nominally fixed density: changing the applied loop voltage or changing the equilibrium field currents, which alters the plasma size and plasma current and thus input power. V_{loop} can be transiently varied from $2-5$ V, as shown in Fig. 3.29. However, only ~ 30 mV-s of Ohmic drive are available for each discharge. The equilibrium field current is available up to 16 kA, but it is typically set between $8-14$ kA.

These two methods to change the input power can be used in conjunction with each other, as demonstrated in Fig. 4.20. These discharges had the same fueling and shape, but their applied loop voltage and/or equilibrium field currents were changed. In this scan at $\bar{n}_e \sim 1.5\times10^{19}m^{-3}$, increasing the loop voltage by 10% and the equilibrium field current by 20% raised the plasma current from 57 kA to 86 kA. These changes increased the total input power from 168 kW to 275 kW. At the lower input power, the discharge remained in L-mode, whereas the discharges at the two higher input powers accessed H-mode. This process of varying the power threshold was then repeated at each fueling rate.

The density at the transition was changed by varying the LFS gas systems' fueling rate during the L-mode phase, with the HFS fueling held constant. LFS fueling is halted before or shortly after the initiation of the HFS fueling to allow an H-mode transition to occur. Altering the LFS fueling during the L-phase, changes the density at the L-H transition by $\sim 10\times$ from $\bar{n}_e = 0.5-4x10^{19}\ m^{-3}$. Examples of these extreme density regimes in Pegasus are shown in Fig. 4.21. In these discharges, the open time and duration of the LFS fueling was varied. The low-fueled (low-density) discharge is fueled by the HFS fueler and one array of LFS fuelers with a total open time of 4.8 ms; its density at the L-H transition was $< 1\times10^{19}\,m^{-3}$. In contrast, the high-fueled case is fueled by the HFS fueler and three arrays of LFS valves with open times of 10.78, 7, and 6 ms, respectively. This discharge achieved a line-integrated density of $\sim 4\times10^{19}\ m^{-2}$, approximately $10\times$ more than the low-fueled discharge. The difference in power between the two discharges is also illustrated. The high-fueled case has ~ 600 kW of input power, $\sim 3\times$ more than the low-fueled case.

The Ohmic power required to access H-mode on Pegasus was determined in over 100 limited and diverted discharges on Pegasus. Two separate experimental campaigns to study the input power necessary to access H-mode at various densities were conducted. One campaign was in the

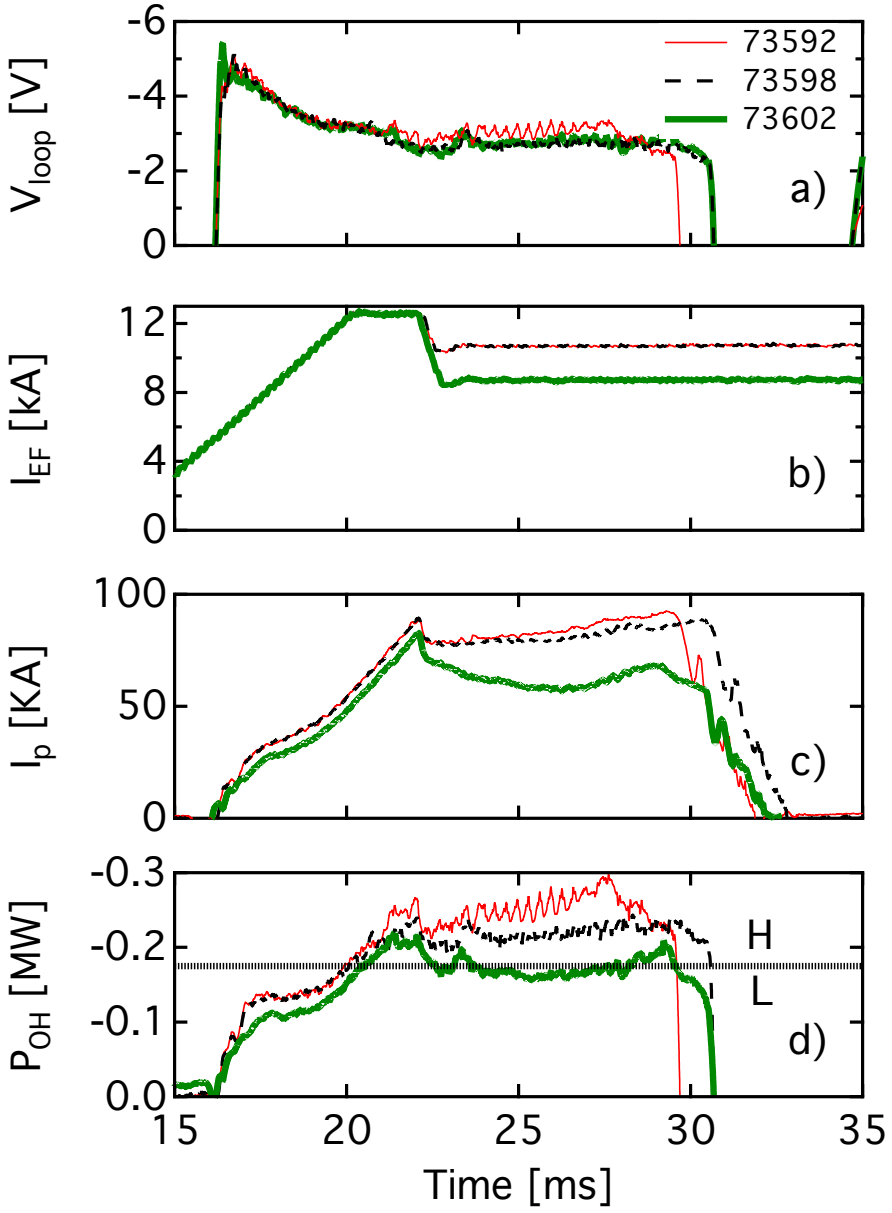

Figure 4.20: Two methods to vary P_{OH}. Changes in V_{loop} (a), I_{EF} (b), and I_p (c) change the applied P_{OH} (d)

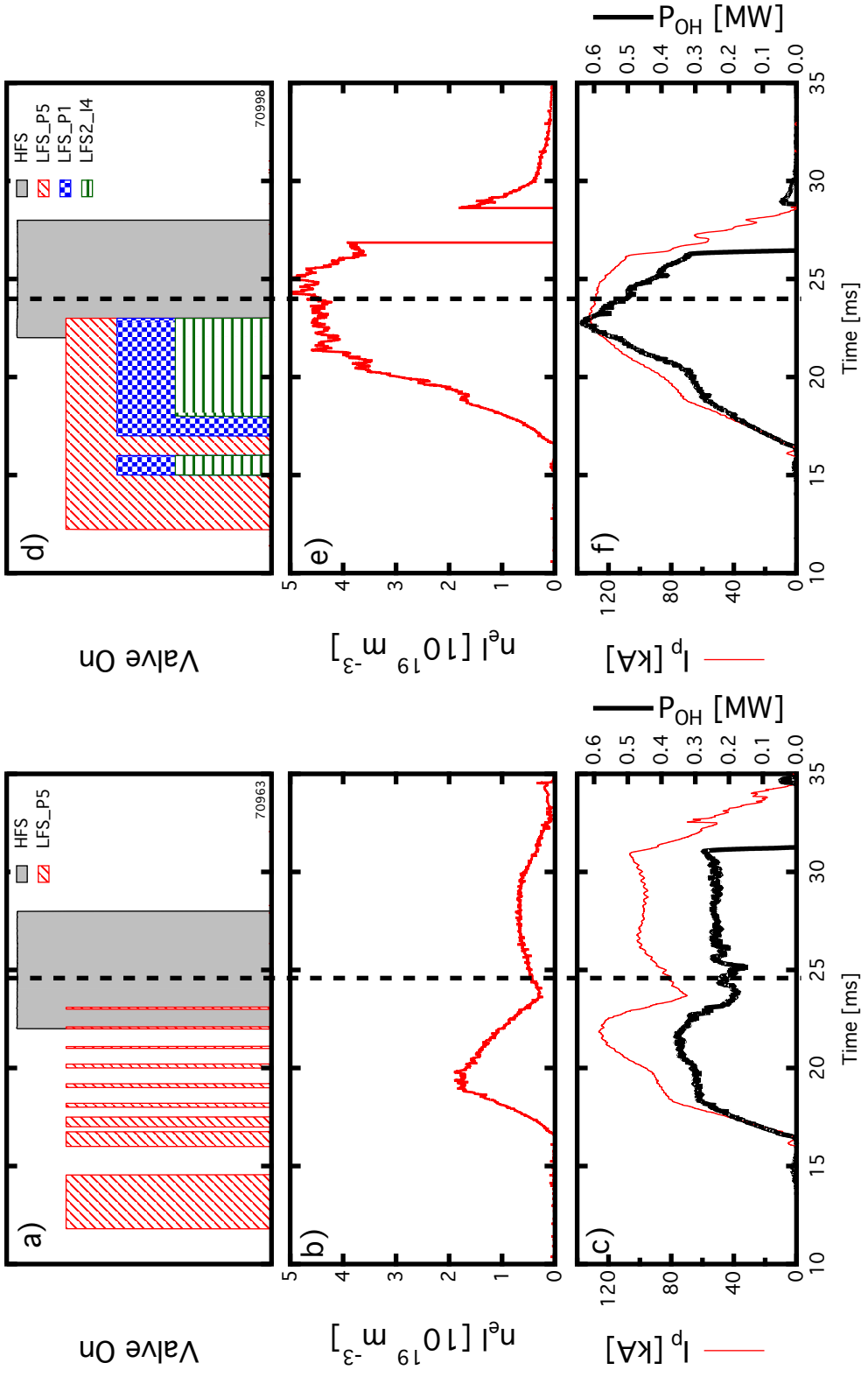

Figure 4.21: Low density (a) and high density (b) discharges used in power threshold scan. The lines denote the time HFS fueling is observed on the camera

limited configuration and the other in the diverted configuration. The limited campaign studied the threshold by varying the density and input power from $\bar{n}_e = 0.5 - 5x10^{19}\ m^{-3}$ and $P_{OH} = 200 - 600$ kW, respectively. These plasmas had $I_p = 40 - 140$ kA, $R_{maj} = 0.2 - 0.35\,m$, and surface area $S = 2.5 - 6\,m^2$. The diverted campaign had a more limited operational space due the negative inductive drive from the divertor coils. Nevertheless, the density and input power were varied from $\bar{n}_e = 0.7 - 2x10^{19}\ m^{-3}$ and $P_{OH} = 200 - 300$ kW, respectively. These plasmas had $I_p = 40 - 120$, with I_p typically less than 100 kA, $R_{maj} = 0.3 - 0.35\,m$, and $S = 5 - 6\,m^2$. The divertor campaign was also complicated by a susceptibility to VDEs.

The L-H transition occurred late in these discharges, to increase the ability to perform reconstructions before and after the L-H transition. The L-H transition time for these plasmas was inferred from at least one of the following H-mode signatures: the plasma edge sharpening on the fast camera, clear bifurcation in the toroidal flux compared to L-mode plasmas, and/or change in the stored energy evolution measured using equilibrium reconstructions, as shown in Fig. 3.24.

The results of this input power threshold survey with density, power and geometry are shown in Fig. 4.22. Fig. 4.22(a) shows the Ohmic input power required to access H-mode as a function of $\bar{n}_e$ for all of these limited and diverted discharges. The line-averaged density is estimated from the line-integrated density and an estimate of the plasma minor radius from the camera image. To improve this analysis, a better estimate of the plasma shape was determined for a subset of the discharges. Plasma shape information is used to accurately determine B_T, $\bar{n}_e$, and surface area, S. In most cases, the plasma shape was estimated using ShapeFIT. In a few cases, including all of the diverted discharges, the shape was determined by a KFIT equilibrium reconstruction at the L-H transition time. These condensed results are shown in Fig. 4.22(b). In this figure, the Ohmic input power is normalized to the ITPA08 toroidal field and surface area dependencies.

While this simplified analysis and shot-to-shot variation results in some scatter in the data, several conclusions on the L-H power threshold on Pegasus may be made. First, there is a general separation of the L and H data, indicating the existence of the power threshold. This threshold increases with density in a fashion consistent with the ITPA empirical scaling, as further illustrated by Fig. 4.23. In this figure, only the discharges with an L-H transition are shown. A scaling proportional to the ITPA density dependence goes through the middle of the L-H threshold data.

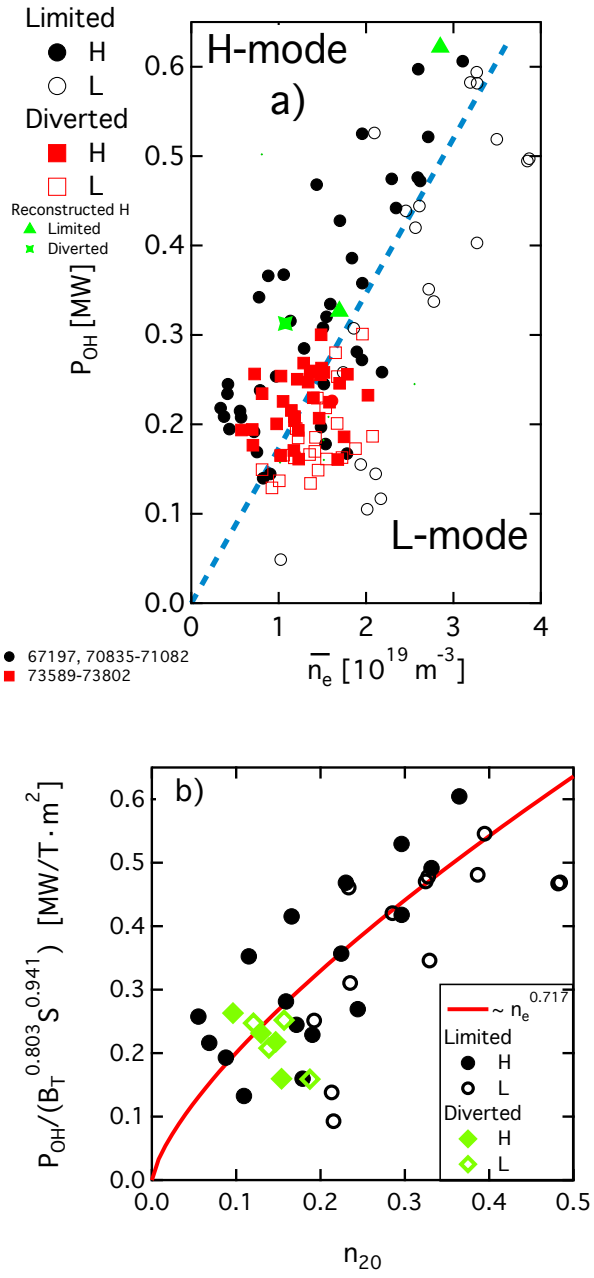

Figure 4.22: Pegasus power threshold density dependence. (a); P_{OH} vs density with the blue lines to generally separate L and H discharges; (b): P_{OH} normalized by B_T and S ITPA dependencies vs density

Second, unlike some high-A tokamaks [36], no apparent minimum in $P_{LH}(\bar{n}_e)$ is observed in Pegasus. Third, the operating space for limited and diverted plasmas topologies overlap: $P_{LH}^{LIM} \approx P_{LH}^{DIV}$.

Some H-mode experiments were conducted at $B_T \sim 0.08$ T to determine H-mode accessibility. H-mode was successfully achieved at this toroidal current with $P_{OH} \sim 300$ kW and $\bar{n}_e = 1-3\times 10^{19} m^{-3}$. Some of these discharges are also included in Fig. 4.23. As expected, the power required to access H-mode is reduced at lower toroidal field compared to the higher field discharge. The normalized power required to access H-mode at this field is consistent with results at higher field. This work illustrates that these experiments were conducted far above the L-H power threshold at this reduced toroidal field.

The local helicity injection initiated discharge in Fig. 4.12 immediately transitioned into H-mode upon the application of Ohmic drive. H-mode is not achieved during local helicity injection plasmas. At the time of transition, $P_{OH} \sim 600$ kW and $\bar{n}_e \sim 1\times 10^{19} m^{-3}$. Based on Ohmic-only discharges, this is sufficient power to induce a transition. So it is not surprising that the discharge immediately transitioned upon entry into the Ohmic phase.

The experimental power threshold is calculated using Equation 3.9. The power radiated in these plasmas is assumed to be zero based on previous work [94]. Thus, the experimental power threshold reduces to

$$P_{LH} = P_{OH} - dW/dt. \tag{4.2}$$

The value of dW/dt is determined by performing time-evolving reconstructions during the L- and H-phase of the discharge. A transition time is inferred by the change in the slope of the plasma or kinetic energy. Power corrections from dW/dt are determined during the L-mode portion of the discharge.

Three time-evolving reconstructions were performed to calculate P_{LH} on Pegasus. These discharges are illustrated by the green points in Fig. 4.22(a) and include two limited and one diverted discharge at densities from $1.2-3.4\times 10^{19}\, m^{-3}$. The results from these reconstructions are summarized in Table 4.2. Reconstructions determined that dW/dt is usually found to $\sim 0.3 P_{OH}$. Thus, P_{LH} ranges from $200-400$ kW on Pegasus. The power threshold predicted by the ITPA08 scaling for these discharges varies from $\sim 10-20$ kW. Thus, Pegasus requires $10-20\times$ more power than predicted by ITPA08 scalings.

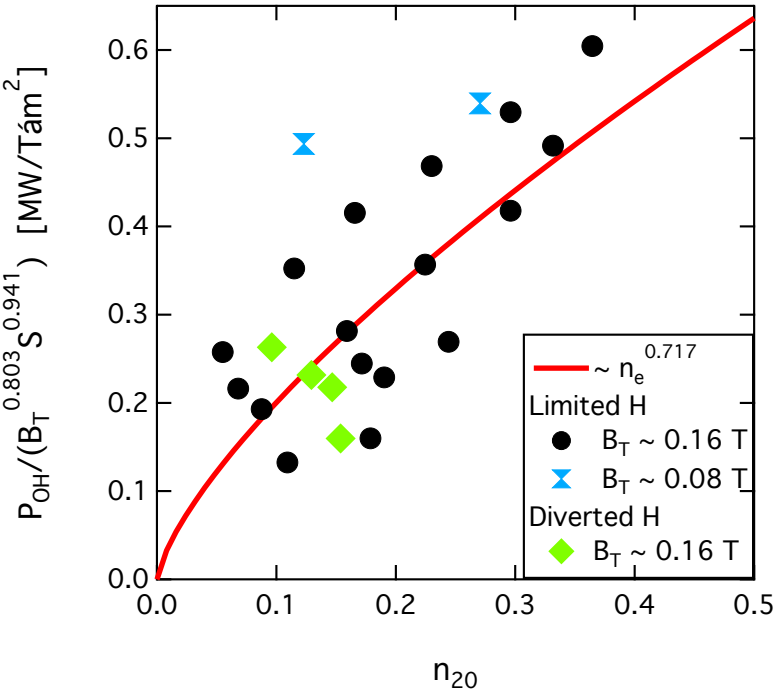

Figure 4.23: H-mode density and B_T dependence. P_{OH} normalized by B_T and S ITPA dependencies vs density for only H-mode discharges

SN	67197	70914	73580
Geometry	Limited	Limited	Diverted
$\bar{n}_e$ ($10^{19} m^{-3}$)	1.67, $n_G = 0.37$	3.43, $n_G = 0.41$	1.21, $n_G = 0.30$
S (m^2)	5.90	4.09	5.82
P_{OH} (kW)	302 $\pm$ 6.3	603 $\pm$ 12.6	319 $\pm$ 6.7
dW/dt (kW)	88.7 $\pm$ 22, $\sim 0.29 P_{OH}$	194 $\pm$ 77.4, $\sim 0.32 P_{OH}$	50.9 $\pm$ 6.0, $\sim 0.16 P_{OH}$
P_{LH} (kW)	214 $\pm$ 22.8	409 $\pm$ 78.4	268 $\pm$ 9.0
P_{ITPA08} (kW)	17.0	20.8	14.2
P_{LH}/P_{ITPA08}	12.6 $\pm$ 1.4	19.7 $\pm$ 3.8	18.8 $\pm$0.6

Table 4.2: Summary of P_{LH} time-evolving reconstructions and comparisons to P_{ITPA08}

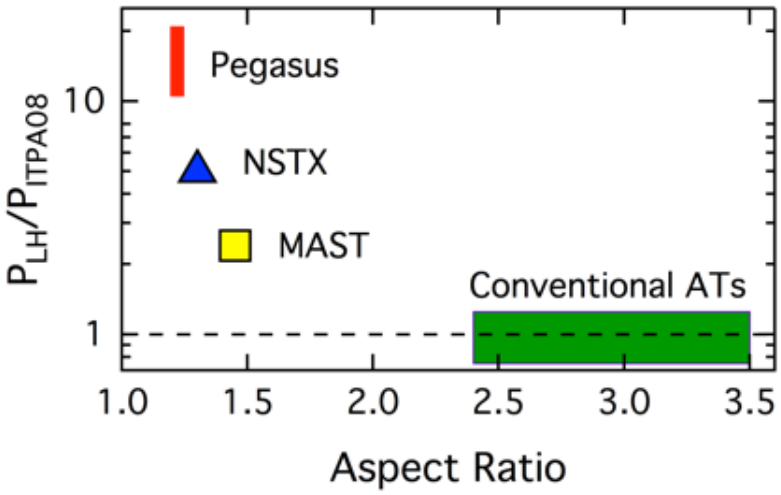

Figure 4.24: P_{LH}/P_{ITPA08} for various aspect ratio tokamaks

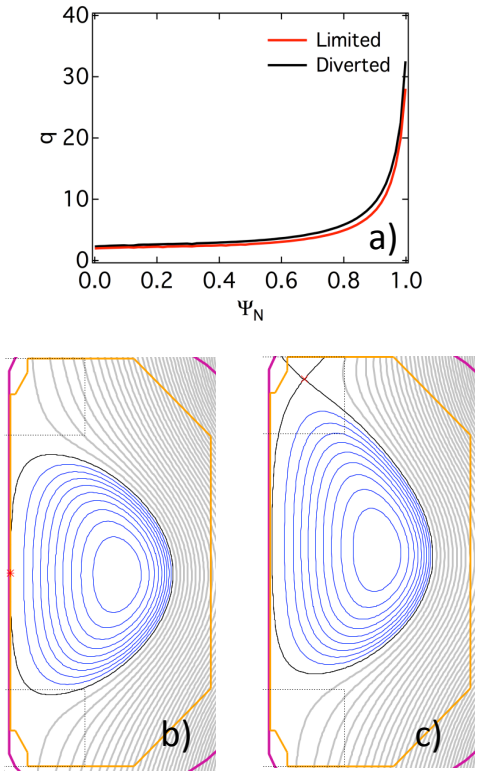

Figure 4.25: Safety profiles for (a) for model equilibria limited (b) and diverted (c) plasmas at $A \sim 1.2$

The power threshold measured on Pegasus exceeds predictions from accepted international scalings by an order of magnitude or more. Figure 4.24 shows the P_{LH} for Pegasus and several tokamaks in the ITPA database [2] normalized to the ITPA08 scaling. As $A \longrightarrow 1$, P_{LH}/P_{ITPA08} significantly increases, confirming a trend suggested by NSTX [2, 40] and MAST [2, 43]. NSTX $(A > 1.3)$ requires $\sim 5\times$ more power than predicted and MAST $(A \approx 1.45)$ requires $\sim 2.5\times$. At $A \geq 2.5$, the power threshold is well described by the ITPA08 scaling. This divergence with aspect ratio hints at underlying physics and calls for more experimental data and refined theory. To date, theoretical models to explain these variations with A are not yet available.

Nevertheless, some of the unique characteristics of P_{LH} at near-unity A (the absence of a P_{LH}-minimizing density n_e^{min} and the P_{LH} insensitivity to magnetic topology) are consistent with the FM^3 L-H transition model [3]. Using Equation 2.17, n_e^{min} is predicted to be $\bar{n}_e \sim 1 \times 10^{18}\, m^{-3}$ $(\bar{n}_e \ll 0.1 n_G)$ for Pegasus. This density is not accessible in Ohmic plasmas due to occurrence of runaways and hence consistent with no appearance of n_e^{min} in Fig. 4.23. The difference in limited and diverted power thresholds is posited to be due to the edge safety factor q_ψ, as shown by Equation 2.18. At high-A, $q_\psi^{LIM} < q_\psi^{DIV}$, which is consistent with the higher observed P_{LH} in limited plasmas. In contrast at $A \lesssim 1.2$, the increased edge shear at low-A results in $q_\psi^{LIM} \approx q_\psi^{DIV}$. This feature is illustrated in Fig. 4.25 for model equilibria Pegasus plasmas at $A \approx 1.2$. Thus, a similar power threshold is expected in both limited and diverted topologies, as observed. The magnitude of P_{LH} on Pegasus is not consistent with the FM^3 model, since the model replicates the ITPA08 scaling by construction.

4.3 Edge Localized Mode Characteristics and Dynamics

ELMs are regularly observed in Pegasus H-mode plasmas. Similar to other tokamaks, ELMs generate characteristic bursts of D_α emission that are temporally correlated with the creation of propagating, field-aligned filamentary structures on fast visible imaging on Pegasus [27].

To date, two classes of ELMs have been seen. The two ELM types are distinguished by their toroidal mode number spectrum and their occurrence at different values of P_{OH}/P_{LH}. Small, Type III-like ELMs are present at $P_{OH} \sim P_{LH}$. As P_{OH} is increased, they transition to large, Type- I-like

ELMs. Large ELM virulence increases further as P_{OH} increases, potentially terminating discharges when $P_{OH}/P_{LH} \gtrsim 2$. Large ELMs typically occur at low density.

Fast camera images of these two ELM types and a quiescent H-mode phase are shown in Fig. 4.26. In the small ELM image, many filaments are present and it is observed as a small edge disturbance. In contrast, the image of a large ELM is very bright, making the filaments difficult to see. Type I ELMs are characterized by a striking spiral heat deposition pattern on the lower divertor plate.

ELM events are detected on a variety of diagnostics on Pegasus, as shown in Fig. 4.27 for a Type I ELM. The ELM event occurs over < 200 μs. During this ELM there is: a characteristic burst of D_α emissions [Fig. 4.27(a)], a change in the Mirnov signal before and during the ELM crash [Fig. 4.27(b)], and a decrease in the line-averaged density [Fig. 4.27(c).]

Transferring from the Type III ELM regime to the Type I regime can be readily accomplished on Pegasus by changing the Ohmic input power. This is demonstrated in a single discharge in Fig. 4.28. Figure 4.28(a) shows the I_p and P_{OH} waveforms for this discharge and Fig. 4.28(b) has its D_α signal. The discharge starts out in L-mode, but as the power is increased an H-mode transition is induced, as illustrated by the drop in D_α signal. Type III ELMs appear immediately in H-mode. They are ubiquitous and cause small perturbations. They are denoted by the small spikes in D_α signal. Then the power is further ramped, creating a period of quiescence, which is interrupted by the triggering of a Type I ELM. This ELM occurred at very high input power $P_{OH}/P_{LH} > 2$, and it caused a L-H back-transition. Very large Type I ELMs on Pegasus cause a back-transition, but smaller Type I ELMs do not. This is demonstrated in Fig. 4.2. In this discharge, a small Type I ELM occurred at ~ 24.5 ms, as illustrated by the D_α spike. The discharge remained in H-mode after this ELM. Typically, only one or two large ELMs is seen in a H-mode discharge, due to the short discharge pulses currently available on Pegasus.

A similar dependence of power on ELM type, as shown in Fig. 4.28(a–c) on Pegasus is also seen on DIII-D, as shown in Fig. 4.28(c) [1]. The DIII-D discharge starts in L-mode and has an H-mode transition when the neutral beam power is increased. Type III ELMs are present at this power level. As the power is increased from 2 to 10 MW a period of quiescence occurs. This is then interrupted by the triggering of Type I ELMs.

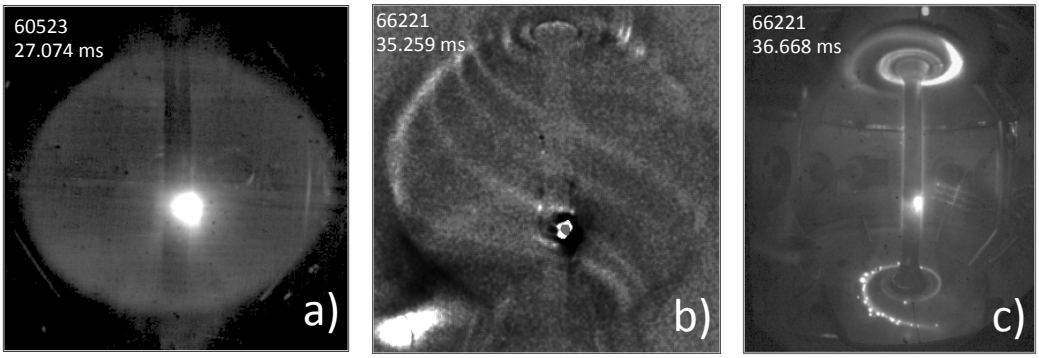

Figure 4.26: Fast camera images of a quiescent H-mode phase (a) and small (b) and large (c) ELMs on Pegasus

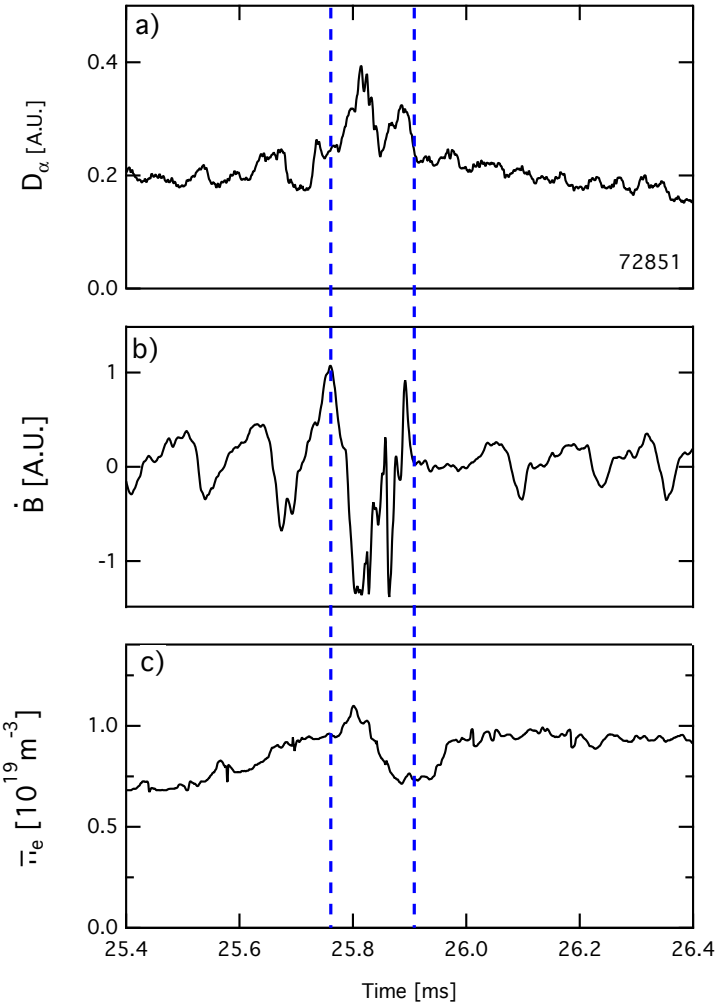

Figure 4.27: Type I ELMs are observed in the D_α signal (a), $\dot{B}$ (b), and $\bar{n}_e$(c)

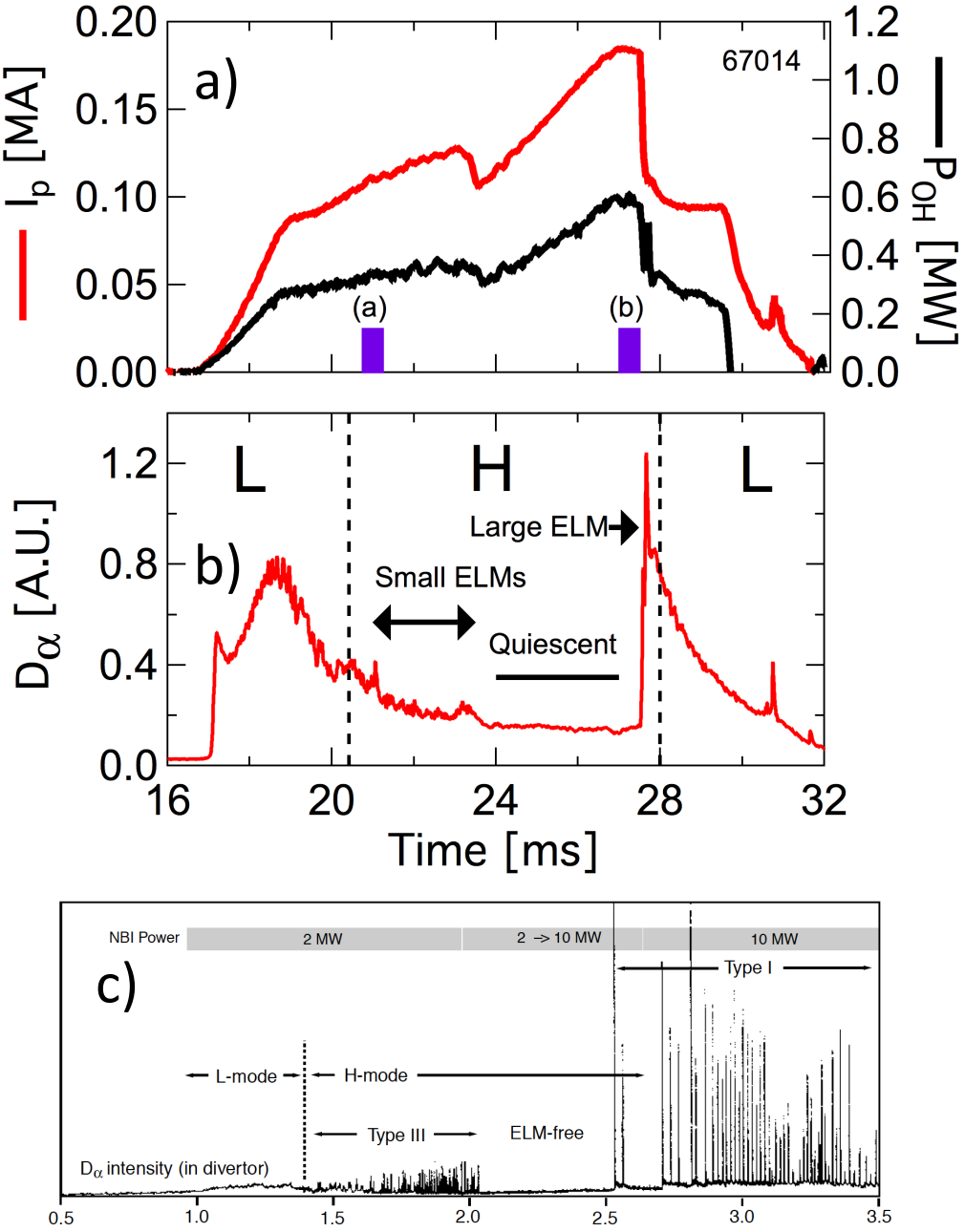

Figure 4.28: ELM dependence on power on Pegasus. I_p and P_{OH} waveforms (a) and D_α signal (b) for a discharge with an L-period, an H-period with Type III ELMs, a quiescent H-mode power and an H-mode period with Type I ELMs. (c) D_α emissions from a DIII-D discharge with an L-period, an H-period with Type III ELMs, a quiescent H-mode power and an H-mode period with Type I ELMs

Type III and Type I ELMs are also distinguished from each other by their toroidal mode spectra. On Pegasus, a magnetic precursor is observed for both ELM types. Mode spectra are derived from cross-phase spectral analysis of a near-edge Mirnov coil array. An example of such an analysis is shown in Fig. 4.29. Multiple n mode numbers are observed during both types of ELMs; this behavior is consistent with the simultaneous presence of multiple unstable peeling-ballooning modes. The mode spectra was measured for the discharge in Fig. 4.28 during the Type III (labeled a) and Type I (labeled b) time periods. The toroidal mode numbers for each ELM type are shown in Fig. 4.30.

Type III ELMs have $n \leq 4$. Type I ELMs have intermediate $5 < n < 15$ present. This trend in n spectra is similar to that reported at $A \sim 1.3$ in NSTX [64].

When comparing dominant n spectra in Type I and Type III ELMs, a marked difference is found in low- and high-A plasmas. At high-A, Type III spectra are dominated by mode numbers greater than those seen in Type I ELMs ($n_{III} > n_I$) [97, 65]. However, at low-A, Type III spectra are dominated by mode numbers less than those in corresponding Type I ELMs ($n_{III} < n_I$). At both aspect ratios, Type I ELM spectra are generally dominated by intermediate $n \sim 6$–15, but at low-A (Pegasus and NSTX [64]) the mode numbers are somewhat lower than on high-A experiments. These trends presumably reflect the increased peeling mode drive ($\propto J_{edge}/B_T$) [98, 99] that naturally occurs at low-A. This influence of peeling drive strength on the n-spectra of ELMs is also reflected in lowered dominant ELM n-values with an increased J_{edge} at high-A [63].

The high spatiotemporal resolution offered by probes at low-A allows unique measurements of ELM nonlinear dynamics. Simultaneous unstable modes are shown in the Type I ELM magnetic spectra in Fig. 4.30. These time behaviors of the dominant $n = 8$ and subdominant $n = 6$ modes before and during the ELM are shown in Fig. 4.31. This figure shows different time evolutions of the modes when they are isolated using a bandpass filter. The $n = 8$ grows continuously throughout this time period, as shown by its $dB_{z_n/dt}$ [Fig. 4.31(a)] and Hilbert transform in [Fig. 4.31(b)]. Nonlinear behavior is also observed during this time trajectory. The $n = 6$ mode is representative of all the other modes in Fig. 4.30. Its $dB_{z_n/dt}$ [Fig. 4.31(c)] and Hilbert transform in [Fig. 4.31(c)] illustrate that it fluctuates during the ELM.

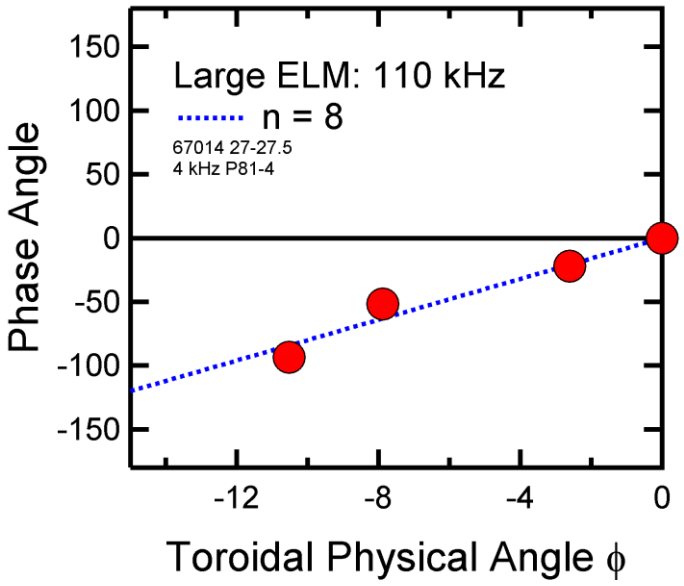

Figure 4.29: Cross-phase spectral analysis of n=8 component during a Type I ELM in Fig. 4.28

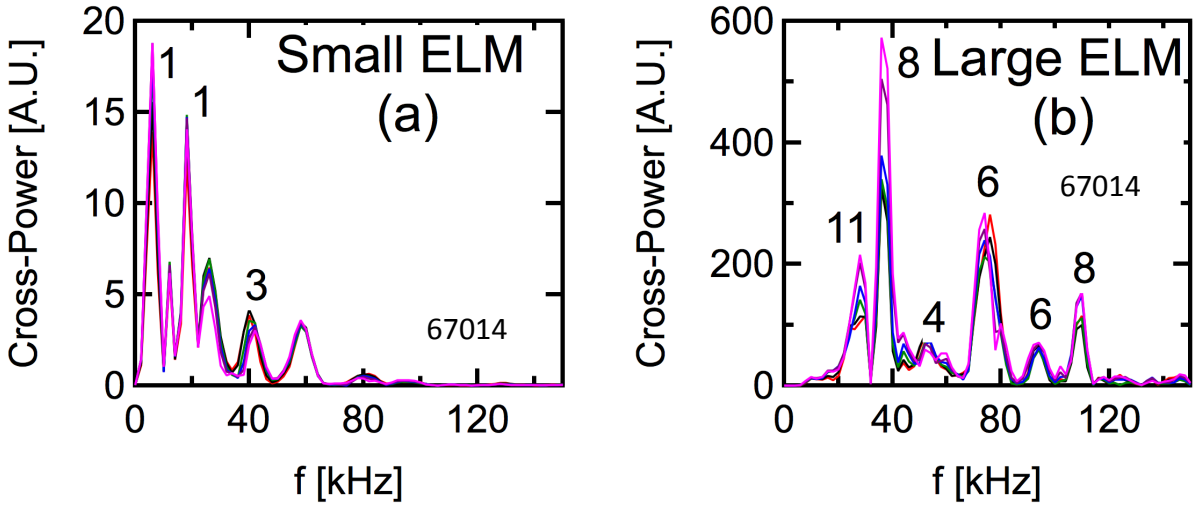

Figure 4.30: ELM toroidal magnetic spectra for small ELMs (a) and large ELMs (b) in Fig. 4.28

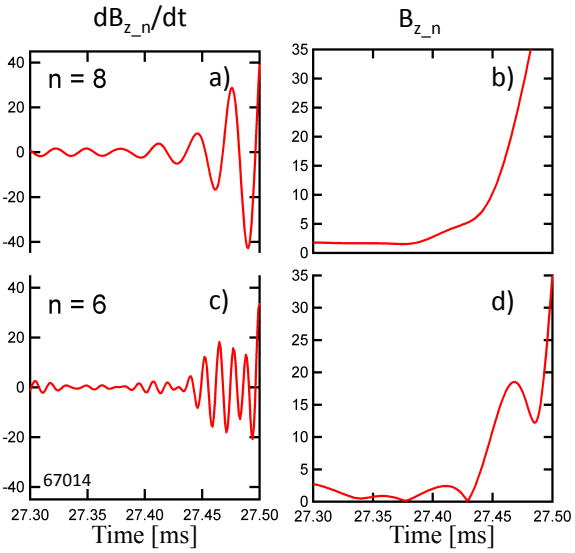

Figure 4.31: Time evolution of n=8 and n=6 components of Type I ELM in Figure 4.28

Both ELM types generate and expel current-carrying filaments during the ELM crash. This feature is hypothesized by electromagnetic blob transport theory [100], observed in nonlinear ELM simulation [101], and is qualitatively similar to prior experimental studies of the nonlinear peeling mode [89]. These measurements of the edge current density profile in Pegasus provide the first experimental evidence of their nonlinear J_{edge} dynamics on Alfvénic timescales ($t < 200$ μs) in both ELM types.

The current profile through a Type III ELM is shown in Fig. 4.32. This figure shows a dynamic current evolution measured at high time and spatial resolution. A modest pedestal exists before the ELM [Fig. 4.32(a)]. The current pedestal begins to build in Fig. 4.32(b). Then there is a rapid collapse accompanied by a current-hole ejection and then a pedestal crash in Fig. 4.32(c). After the ELM, the pedestal begins to recover in Fig. 4.32(d–e). These current dynamics are identical to those observed previously on Pegasus in the L-mode peeling studies [89].

Type I ELM current dynamics were also measured and show similar behavior to those of Type III ELMs. This ELM event was measured at higher temporal and spatial (less spatial smooth was applied) resolution and is shown in Fig. 4.33. Figure 4.33 depicts the complex evolution of $J_{edge}(R,t)$ during a time interval spanning a Type I ELM crash. Time values are referenced to the first detectable rise in ELM magnetic activity [Fig. 4.33(a)]. The pre-ELM current pedestal builds

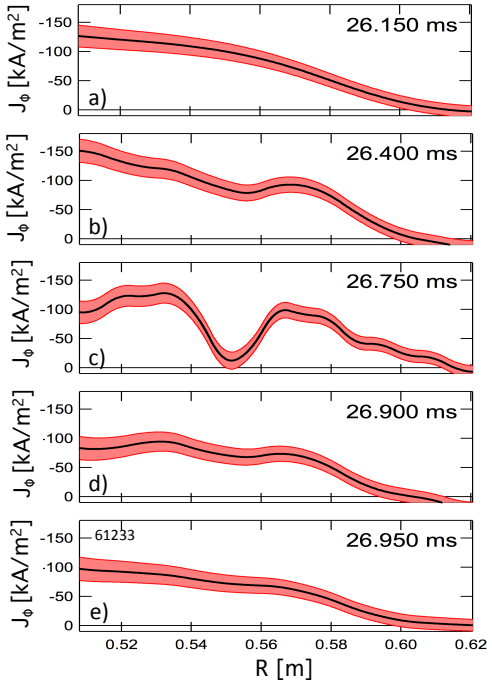

Figure 4.32: Current profile evolution through a Type III ELM

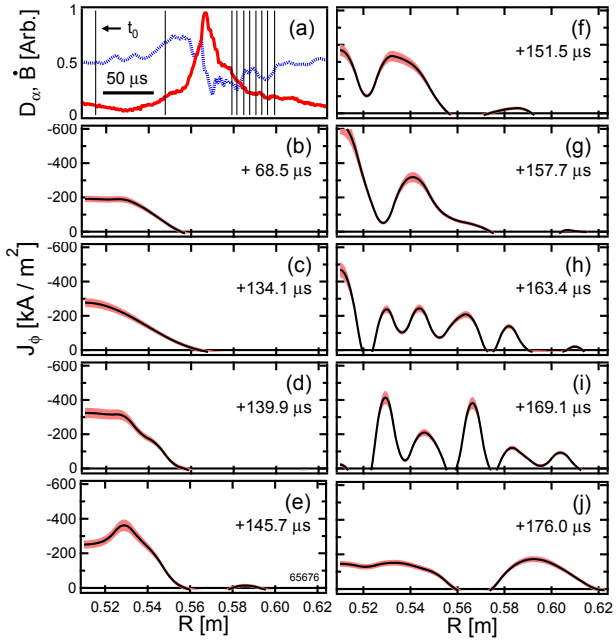

Figure 4.33: Current profile evolution through Type I ELM on Pegasus. (a): D_α (solid red), $\dot{B}$ (dashed blue), and profile time indicators (thin black); (b)–(j): local $J_\phi\,(R,t)$

over [Fig. 4.33(b)–(d)], with the innermost sensor nominally doubling in local J_ϕ. During the following collapse phase [Fig. 4.33(e)–(j)], J_{edge} first develops fragmentary "current-hole" perturbations [Fig. 4.33(f)] that expand past the equilibrium last closed flux surface location at $R \approx 0.56$ m [Fig. 4.33(g)]. Current is transported radially outward [Fig. 4.33(h)–(i)]. J_ϕ then coalesces into two regions separated at $R \approx 0.57$ m that become the post-ELM pedestal and a current-carrying filament [Fig. 4.33(j)]. The filament is subsequently expelled and radially accelerates away from the plasma. Such inferred filament generation is temporally coincident with an outwardly-propagating filament detected with fast visible imaging at the Hall sensor locations.

Finally, initial tests of the effects of injecting a perturbing helical current into the scrape off region of an H-mode plasma were conducted. In particular, the local helicity current injectors injected strong current streams along the open helical field lines a few centimeters outside the pedestal region. The injection current I_{Bias} was varied from 0–4 kA. The perturbation was applied from 24–28 ms.

The resulting effects on the plasma current and toroidal flux are shown in Fig. 4.34. At relatively low $I_{Bias} = 0 - 1$ kA, no effects on I_p or Φ_D are evident. Although there is a marked decrease in Type III ELM activity, as illustrated by the D_α emissions in Fig. 4.35. At $I_{Bias} \geq 2$kA, a strong drop in I_p and Φ_D is evident, as the perturbing field is applied. For the $I_{Bias} = 2$ kA case, the bias current was applied for only $24 - 26$ ms, due to a controller failure. The plasma current and H-mode behavior recovered upon this early I_{Bias} termination.

These first tests suggest that this strongly asymmetric magnetic perturbation applied to the plasma edge region can both alter ELM activity, and possibly stability, and that the plasma edge pedestal and H-mode confinement itself may be susceptible to edge current injection. In addition, the strong difference in discharge behavior between $I_{Bias} = 1$ kA and 2 kA, suggest a threshold-like behavior for transition to a region less favorable than the H-mode region. These results are clearly preliminary and somewhat speculative. Nonetheless, they suggest that the use of injected local current streams into the H-mode edge region for H-mode perturbation and/or ELM mitigation may be a fruitful research direction in the future.

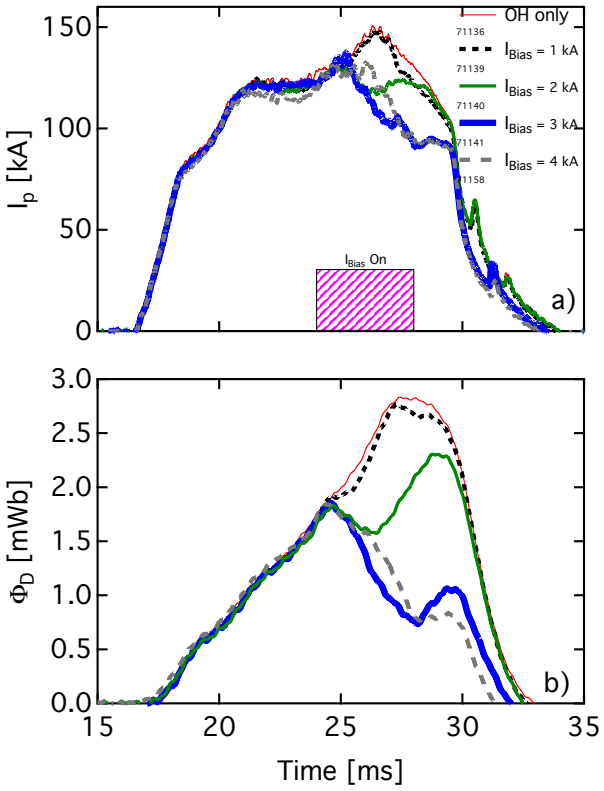

Figure 4.34: H-mode plasmas perturbed with a helical current. (a): I_p; (b): Φ_D

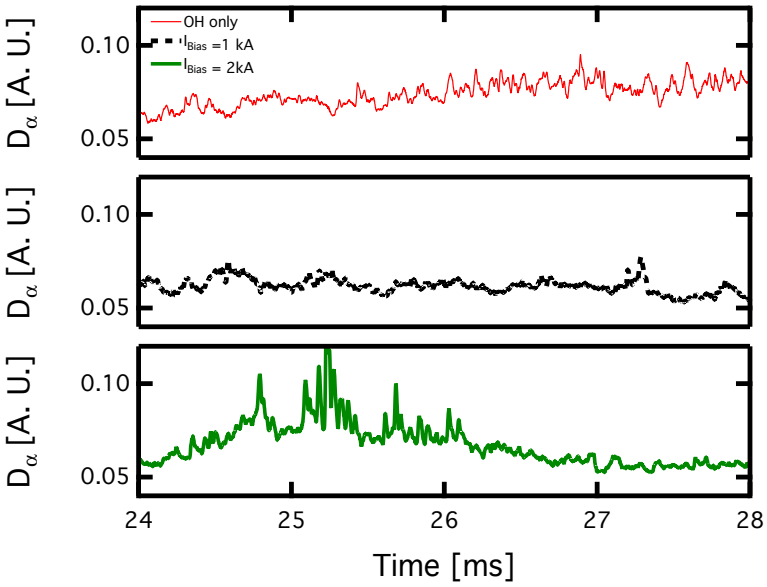

Figure 4.35: D_α emissions for OH only, I_{Bias} of 1 and 2 kA case of Figure 4.34

Chapter 5

Summary and Conclusions

This dissertation begins the documentation of the H-mode confinement regime on the Pegasus Toroidal Experiment. The particular topics studied in this thesis were: 1) determining the general characteristics of H-mode plasmas and how they differed from L-mode plasmas; determining the H-mode operational space and the power threshold; and 3) determining the ELM characteristics and dynamics observed on Pegasus. These points will be summarized and discussed below and possible future directions of this work will be suggested.

H-mode Characteristics

H-mode plasmas on Pegasus are distinguished from L-mode plasmas by: formation of a quiescent edge, increased core intrinsic toroidal rotation, development of edge pressure and current pedestals, improvement in energy confinement by $\sim 2\times$, change in the peakedness of the current profiles, and heating of the electron and ion channels. A sharp quiescent edge is observed in H-mode plasmas, whereas a noisy turbulent edge is observed in L-mode plasmas. A quiescent edge is formed on the fast camera in < 1 ms at the L-H transition. L-mode plasmas have negligible toroidal rotation, whereas the core of H-mode plasmas rotate at ~ 10 km/s in the counter-current direction. Edge pedestals are observed in both the current and pressure profiles. The scales lengths of the current and pressure pedestals are both ~ 2 cm.

The improvement in energy confinement is illustrated by the increase in $< H_{98} >$ from 0.5 to 1.0 from L-mode to H-mode, respectively. The current profiles in H-mode plasmas are more peaked than L-mode plasmas. This increase in l_i is consistent with the increase in paramagnetism from L-to-H plasmas. H-mode plasmas have higher core impurity ion temperatures than L-mode

plasmas, indicated central ion heating. Heating in the electron core is indicated by the presence of CV emissions and increased core electron temperature determined from Thomson scattering measurements.

H-mode Operational Space and Power Threshold

Several recent upgrades to the Pegasus facility have facilitated and improved H-mode access on Pegasus. The installation of HFS fueling coupled with the low edge recycling on Pegasus provides reliable H-mode access. The installation of augmented divertor coils and radial coils allows single null diverted H-mode access in the favorable direction.

H-mode is regularly achieved in both limited and favorable single null diverted topologies. It is accessible over a wide operating space at $B_T \sim 0.16$ T: $n_e = 0.5 - 5 \times 10^{19} m^{-3}$, $P_{OH} = 200 - 600$ kW, and $I_p = 40 - 170$ kA. Exploratory studies also indicate H-mode access at $B_T \sim 0.08$ T.

The power threshold was studied on Pegasus at $B_T \sim 0.16$ T by varying the density, power and geometry. It was found to behave quite differently at low-A when compared with high-A operations. The threshold is 10–20$\times$ higher than projected by the conventional ITPA08 scaling. This continues and emphasizes the trend indicated from other low-A tokamaks, MAST and NSTX, that increasingly more power than predicted by the scaling is required as A decreases. A density dependence proportional to that in the ITPA08 scaling is observed on Pegasus. Unlike at higher-A, no minimum P_{LH} with density is observed. Also in contrast to higher-A tokamaks, where P_{LH} is $\gtrsim 2\times$ higher in limited plasmas than diverted plasmas, the threshold in approximately the same in both limited and favorable single null diverted Pegasus plasmas. Some of these P_{LH} results (the absence of a P_{LH}-minimizing density n_e^{min} and the P_{LH} insensitivity to magnetic topology) are consistent with the FM^3 model for the L-H transition.

ELM Characteristics and Dynamics

Two classes of ELMs have been identified on Pegasus by their presence at different power levels and their toroidal mode spectra. These ELMs have a similar power dependence as observed elsewhere: small Type III ELMs occur at low input power $P_{OH} \sim P_{LH}$ and large Type I ELMs occur at high input power $P_{OH} \gg P_{LH}$. Their measured n are consistent with NSTX results but differ

from high-A plasmas with n systematically lower than at high-A. This is presumably due to the higher peeling mode drive at low-A. Nonlinear ELM dynamics are observed on Pegasus with high spatiotemporal resolution, due to the unique edge parameters on Pegasus that allow probe pedestal measurements. Simultaneously unstable modes are seen in Type I ELM magnetic spectra and they are observed to have different nonlinear time evolutions. Current profile measurement through an ELM show a complex, multimodal pedestal collapse and subsequent ejection of a current-carrying filament.

5.1 Conclusions

This dissertation extends the observations of the H-mode confinement regime to $A \lesssim 1.2$. H-mode is readily accessible in a small-scale tokamak with Ohmic heating alone in both limited and diverted configurations. The characteristics of this regime are generally similar to that observed at higher-A, but clear differences are observed in P_{LH} and ELM characteristics. To date, the energy confinement time in H-mode plasmas is consistent with the IPB(y,2) scaling.

The L-H power threshold has a similar dependence on density and toroidal field as observed elsewhere. However, no minimum in the power threshold with density is observed. Also no difference is seen in the power threshold between limited and diverted plasmas. These two results are consistent with the FM^3 model of the L-H transition. Most strikingly though, the values of P_{LH} at $A \lesssim 1.2$ are $> 10\times$ than expected by the ITPA08 scaling. This extends the trend of P_{LH} depending upon aspect ratio as observed on NSTX and MAST and hints as underlying physics not yet understood. The only empirical scaling with an aspect ratio dependence, the ITPA04 scaling, also does not explain this phenomena. It predicts a lower power threshold $\sim 5\times$ than observed on Pegasus.

Two common ELM types, Type I and III, are observed and have similar dependencies on power and toroidal mode number, as observed elsewhere. However, the toroidal mode numbers of both ELM types are systematically lower than at higher-A, in agreement with NSTX data. This suggests that STs operate on a different part of the peeling ballooning diagram. Typically, it is believed that ATs operate on the ballooning portion of the diagram. However, due to their lower toroidal field,

STs have much higher peeling drive than ATs. This explanation is consistent with experiments on JET, where increased peeling drive decreased the dominant ELM n-values [63].

A novel experiment of injecting a perturbing helical current into the scrape off region of an H-mode plasma changed the plasma performance and possibly ELM behavior.

These observations hint at new insights into the H-mode power threshold and ELM behavior and highlight the importance of studying H-mode and ELMs at extremes in parameter space.

5.2 Outstanding Questions and Future Direction

This work begins the process of characterizing H-mode and ELM properties at near-unity aspect ratio. However, there is still more more physics to be studied in H-mode plasmas at $A \lesssim 1.2$. Pegasus provides a rich test facility to continue these studies. By operating at near-unity aspect ratio, Pegasus has access to unique physics, including edge pedestal access with probes, that allow detailed measurements that are not possible at larger facilities.

Suggestions for future H-mode work on Pegasus include: detailed energy confinement studies; pedestal profile characterization; turbulence characterization; H-mode power threshold studies with B_T, I_p, geometry, and working gas; further experiments and analysis of nonlinear ELM dynamics; and detailed studies of current injection into H-mode plasmas.

In order to best accomplish this work, improved capabilities of the facility and diagnostics would be beneficial. Plasmas with a stable edge and longer pulse length are desired. This would provide: more reliable pedestal measurements; a transport equilibrated plasma; and increase the number of Type I ELMs observed per discharge. An upgrade has been proposed that would allow many of these capabilities. However, in the short term, local helicity injection startup to Ohmic handoff would also extend the current operating space. Initial experiments suggest that local helicity injection to Ohmic plasmas have reduced MHD. This startup technique also increases the available V–s. New and improved diagnostics are also coming online that will help with these studies. In particular, Thomson scattering now has a high temperature grating and improved radial resolution.

APPENDIX
Virial Analysis for Energy Confinement

A conventional and straightforward method to accurately determine the energy confinement time is accomplished through the "Virial Analysis." In this method, magnetic measurements of the external polodial magnetic field and flux are used to constrain the plasma shape and then solve for β_p and the plasma internal inductance, l_i. The Virial Analysis is a fast and efficient technique that can be derived from the stationary MHD equilibrium equations for an axisymetric torus as described by Lao *et al.* [102] and [4]. For isotropic plasmas, as is the case of Pegasus, the following equations are utilized:

$$3\beta_p + l_i = S_1 + S_2 \tag{A.1}$$

$$\beta_p + l_i + \mu = \frac{R_t}{R_0} S_2 \tag{A.2}$$

$$\beta_p - (\alpha - 1)\, l_i = S_3. \tag{A.3}$$

S_1, S_2, and S_3 are integrals of the poloidal magnetic field over the surface, defined as:

$$S_1 = \frac{1}{B_{pa}^2 \Omega} \int_\Gamma dS B_p^2 \left(R\overrightarrow{e_R} + Z\overrightarrow{e_Z} - R_0\overrightarrow{e_R}\right) \cdot \vec{n}, \tag{A.4}$$

$$S_2 = \frac{1}{B_{pa}^2 \Omega} \int_\Gamma dS B_p^2 R_0 \overrightarrow{e_R} \cdot \vec{n}, \tag{A.5}$$

$$S_3 = \frac{1}{B_{pa}^2 \Omega} \int_\Gamma dS B_p^2 Z \overrightarrow{e_Z} \cdot \vec{n}, \tag{A.6}$$

where B_{pa} is the averaged poloidal magnetic field at the minor radius, Ω is the volume of a torus containing the plasma, Γ is the surface bounding Ω, dS is an outward facing surface element, B_p is the polodial magnetic field, R and Z are the relevant spatial coordinates, $\overrightarrow{e_R}$ and $\overrightarrow{e_Z}$ are the normalized vectors in the radial and vertical direction, and $\vec{n}$ is the unit vector normal to Γ. R_T is a characteristic radius of the toroidal configuration that is defined as:

$$R_t = \frac{\int_\Gamma dV\, g}{\int_\Gamma dV \frac{g}{R}}. \tag{A.7}$$

dV is the volume element and $g = P_\parallel + n_m U_t^2 + \frac{B_p^2 + B_{tv}^2 - B_t^2}{8\pi}$, where $P_\parallel$ is the parallel component of the pressure tensor, n_m is the mass density of the plasma, U_t is the toroidal component of the plasma flow velocity, B_{tv} is the vacuum toroidal magnetic field, and B_t is the toroidal magnetic field. α characterizes the ratio between twice the magnetic energy stored in the vertical poloidal field and the poloidal magnetic energy stored in the plasma as described by:

$$\alpha = 2\frac{\int_\Omega \left(\vec{B}_p \cdot \overrightarrow{e_Z}\right)^2}{\int_\Omega dV B_p^2}. \tag{A.8}$$

μ is the plasma diamagnetism as described by:

$$\mu = \frac{1}{B_{pa}^2 \Omega} \int_\Omega \left(B_{tv}^2 - B_t^2\right). \tag{A.9}$$

It is frequently estimated from the toroidal flux measured by a diamagnetic loop to be:

$$\mu \approx \frac{4\pi B_{T0} R_0 \Phi_D}{B_{pa}^2 V}. \tag{A.10}$$

The energy confinement time is calculated by determining β_p from Equations A.1–A.3:

$$\beta_p = \frac{S_1}{2} + \frac{S_2}{2}\left(1 - \frac{R_T}{R_0}\right) + \mu \tag{A.11}$$

and/or

$$\beta_p = \frac{\left[\left(S_1 + S_2\right)(\alpha - 1) + S_3 + \alpha\mu\right]}{1 + 3(\alpha - 1)}. \tag{A.12}$$

l_i is solved similarly and is equal to:

$$l_i = \frac{1}{\alpha - 1}\left[\frac{S_1}{2} + \frac{S_2}{2}\left(1 - \frac{R_t}{R_0}\right) - S_3\right]. \tag{A.13}$$

β_p is then readily related to W_k via

$$W_k = \frac{3\beta_p B_{pa}^2 \Omega}{4\mu_0}, \tag{A.14}$$

where B_{pa} is in T and Ω is in m^3. The energy confinement is then calculated using Equation 3.10, usually with the assumption that $dW/dt \approx 0$. Thus, $\tau_e \propto W_k$.

Equation A. 11 is frequently simplified by using high-A and circular approximations to:

$$\beta_p^{circ} = 1 + \mu. \tag{A.15}$$

However, this approximation does not accurately determine β_p and W_k as $A \to 1$, as illustrated in Fig. A.1. Figure A.1(a) compares β_p calculated using this approximation with β_p calculated from predictive Grad-Shafranov equilibria. This analysis was performed by constructing predictive KFIT equilibria at various aspect ratios from 1.15 (very low-A on Pegasus) to 6 (very high-A) and β_p from the paramagnetic regime $(0-1)$ to the diamagnetic regime $(1-2)$. Figure A.1(b) compares the kinetic energies determined from these two β_p calculation methods at various polodial betas. This approximation well describes β_p and W_k at $A = 6$. However, as the aspect ratio approaches unity, the accuracy of this approximation decreases rapidly. At $A \sim 2.5$ and $\beta_p < 1$, W_k is overestimated by a factor of ≤ 2. At the lowest aspect ratio $A = 1.15$, W_k and τ_e are over predicted by $\lesssim 10\times$.

The accuracy of this approximation also depends strongly on β_p. At $\beta_p \sim 1$, $\beta_{p,circ}$ matches $\beta_{p,KFIT}$ reasonably well at all aspect ratios. For $\beta_p < 1$, Equation A.15 overpredicts β_p and W_k, but for $\beta_p > 1$ it underpredicts β_p and W_k. $\beta_p < 1$ is the operational regime of interest for Pegasus, with typical $\beta_p = 0.3 - 0.6$. As $\beta_p \to 1$ at $A \leq 2.5$, the accuracy of $W_{k,circ}$ decreases, with $\frac{W_{k,circ}}{W_{k,KFIT}}$ varying from 2 to 8 at A of 2.5 to 1.15, respectively. Thus, utilizing Equation A.15 is inappropriate for Pegasus and similar low-A plasmas, since it would grossly overpredict the energy confinement time by $2-8\times$.

However, if instead Equation A.11 is used to calculate the polodial beta, β_p is accurately calculated at all aspect ratios and poloidal betas as shown in Fig. A.2. This figure illustrates that β_p calculated using the full Virial Analysis is in good agreement with β_p calculated from predictive Grad-Shafranov equilibria. Thus, by utilizing Equation A.11, the energy confinement time can be

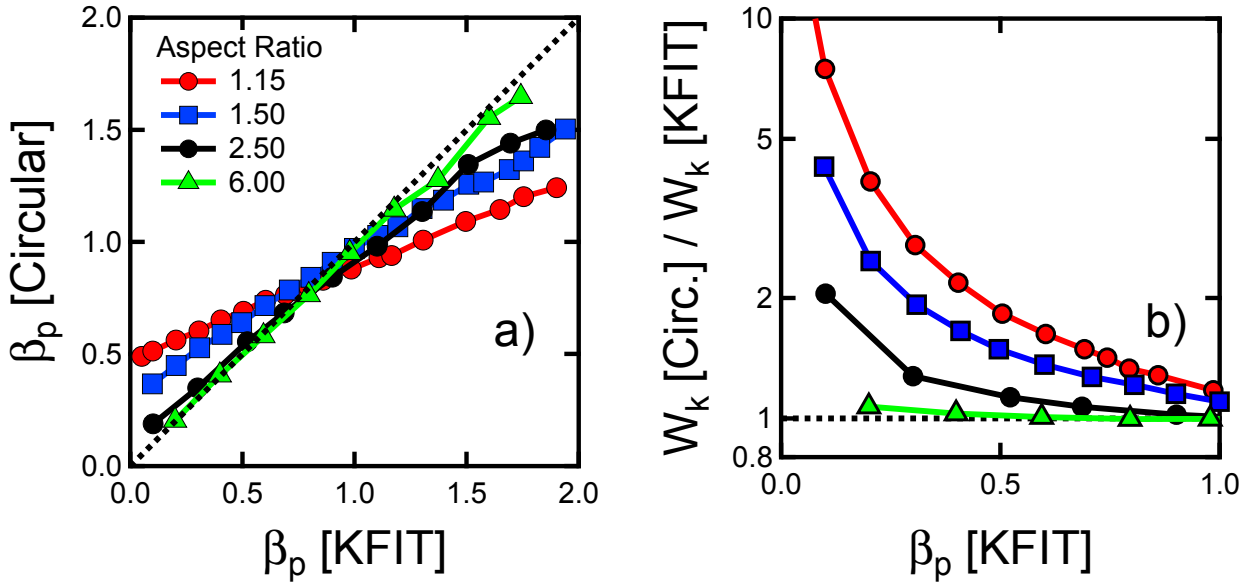

Figure A.1: (a): Comparison of β_p calculated using model equilibria and Equation A.15, (b): Comparison of resultant W_k compared to β_p

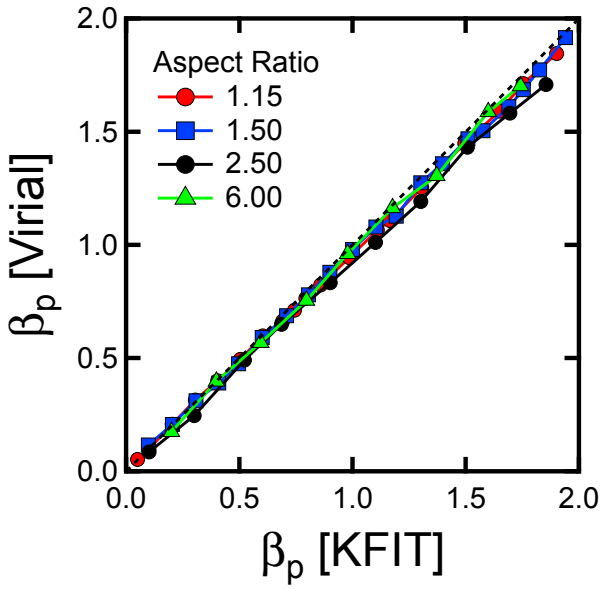

Figure A.2: Comparison of β_p calculated using model equilibria and Equation A.11

accurately determined from external magnetic measurements. Using Equation A.12 also provides β_p in agreement with Grad-Shafranov equilibria. This calculation method is currently being implemented for Pegasus plasmas in the ShapeFIT fast boundary reconstruction code to provide fast estimates of the energy confinement time.

Bibliography

[1] ITER Physics Basis Editors, "Chapter 2: Plasma confinement and transport," *Nuclear Fusion*, vol. 39, p. 2175, 1999.

[2] Y. R. Martin, T. Takizuka, and the ITPA CDBM H-mode Threshold Data Group, "Power requirement for accessing the H-mode in ITER," *Journal of Physics: Conference Series*, vol. 123, p. 012033, 2008.

[3] W. Fundamenski, F. Militello, D. Moulton, and D. C. McDonald, "A new model of the L–H transition in tokamaks," *Nuclear Fusion*, vol. 52, p. 062003, 2012.

[4] J. Wesson, *Tokamaks*, 4th ed. Oxford University Press, 2011.

[5] E. A. Unterberg, "Accesing High Normalized Current in an Ultra-low-aspect-ratio Torus," Ph.D. dissertation, University of Wisconsin–Madison, 2007.

[6] N. A. Uckan, "Tokamak confinement projections and performance goals," *Fusion Technology*, vol. 15, p. 391, 1989.

[7] D. E. Post, K. Borass, J. D. Callen, S. A. Cohen, J. G. Cordey, F. Engelmann, N. Fujisawa, M. F. A. Harrison, J. T. Hogan, H. J. Hopman, Y. Igitkhanov, O. Kardaun, S. M. Kaye, S. Krasheninnikov, A. Kukushkin, V. Mukhovatov, W. M. Nevins, A. Nocentini, G. W. Pacher, H. D. Pacher, V. V. Parail, L. D. Pearlstein, L. J. Perkins, S. Putvinskij, K. Reidel, D. J. Sigmar, M. Sugihara, D. W. Swain, T. Takizuda, K. Tani, T. Tsunematsu, N. A. Uckan, J. G. Wegrowe, J. Wesley, S. Yamamoto, R. Yoshino, K. Young, P. N. Yushmanov, and i. Contributors, *ITER Physics*. Vienna: International Atomic Energy Agnecy, 1991.

[8] A. Sontag, "Determination of Equilibrium and Stability Characteristics of low-A ST Plasmas in the PEGASUS Toroidal Experiment," Ph.D. dissertation, University of Wisconsin-Madison, 2002.

[9] E. J. Doyle, W. A. Houlberg, Y. Kamada, V. Mukhovatov, T. Osborne, A. Polevoi, G. Bateman, J. W. Connor, J. G. C. retired, T. Fujita, X. Garbet, T. S. Hahm, L. D. Horton, A. E. Hubbard, F. Imbeaux, F. Jenko, J. E. Kinsey, Y. Kishimoto, J. Li, T. C. Luce, Y. Martin, M. Ossipenko, V. Parail, A. Peeters, T. Rhodes, J. E. Rice, C. M. Roach, V. Rozhansky, F. Ryter, G. Gaibene, R. Sartori, A. C. C. Sips, J. A. Snipes, M. Sugihara, E. J. Synakowski, H. Takenaga, T. Takizuda, K. Thomsen, M. R. Wade, H. R. Wilson, I. T. P. T. Group, I. C. D. Group, M. Topical, Pedestal, and I. Edge Topical Group, "Plasma confinement and transport," *Nuclear Fusion*, vol. 47, p. S18, 2007.

[10] R. S. Granetz, I. H. Hutchinson, J. Sorci, J. H. Irby, B. LaBombard, and D. Gwinn, "Disruptions and halo currents in Alcator C-Mod," *Nuclear Fusion*, vol. 36, p. 545, 1996.

[11] W. M. Stacey, *Fusion Plasma Physics*. Wiley-VCH, 2012.

[12] F. Troyon, R. Gruber, H. Saurenmann, S. Semenzato, and S. Succi, "MHD-limits to Plasma Confinement," *Plasma Physics and Controlled Fusion*, vol. 26, p. 209, 1983.

[13] J. L. Cecchi, R. J. Knize, H. F. Dylla, R. J. Fonck, D. K. Owens, and J. J. Sredniawski, "Reduction of recycling by pumping at the PDX limiter," *Journal of Nuclear Materials*, vol. 111-112, p. 305, 1982.

[14] E. S. Marmar, "Recycling processes in tokamaks," *Journal of Nuclear Materials*, vol. 76-77, p. 59, 1978.

[15] G. Federici, C. H. Skinner, J. N. Brooks, J. P. Coad, C. Grisolia, A. A. Haasz, A. Hassanein, V. Philipps, C. S. Pitcher, J. Roth, W. R. Wampler, and D. G. Whyte, "Plasma-material interactions in current tokamaks and their implications for next step fusion reactors," *Nuclear Fusion*, vol. 41, p. 1967, 2001.

[16] M. W. Bongard, "Edge magnetohydrodynamic instability studies in the Pegasus Toroidal Experiment," Ph.D. dissertation, University of Wisconsin–Madison, 2011.

[17] A. W. Morris, R. J. Akers, G. F. Counsell, T. C. Hender, B. Lloyd, A. Sykes, G. M. Voss, and H. R. Wilson, "Spherical tokamaks: Present status and role in the development of fusion power," *Fusion Engineering and Design*, vol. 74, p. 67, 2005.

[18] Y. K. M. Peng and D. J. Strickler, "Features of spherical torus plasmas," *Nuclear Fusion*, vol. 26, p. 769, 1986.

[19] Y. K. M. Peng, "The physics of spherical torus plasmas," *Physics of Plasmas*, vol. 7, p. 1681, 2000.

[20] S. A. Sabbagh, A. C. Sontag, J. M. Bialek, D. A. Gates, A. H. Glasser, J. E. Menard, W. Zhu, M. G. Bell, R. E. Bell, A. Bondeson, C. E. Bush, J. D. Callen, M. S. Chu, C. C. Hegna, S. M. Kaye, L. L. Lao, B. P. LeBlanc, Y. Q. Liu, R. Maingi, D. Mueller, K. C. Shaing, D. Stutman, K. Tritz, and C. Zhang, "Resistive wall stabilized operation in rotating high beta NSTX plasmas ," *Nuclear Fusion*, vol. 46, p. 635, 2006.

[21] A. Sykes, the START Team, the NBI Team, the MAST Team, and the Theory Team, "The spherical tokamak programme at Culham," *Nuclear Fusion*, vol. 39, p. 1271, 1999.

[22] T. C. Hender, S. J. Allfrey, R. Akers, L. C. Appel, M. K. Bevir, R. J. Buttery, M. Gryaznevich, I. Jenkins, O. J. Kwon, and K. G. McClements, "Magneto-hydro-dynamic limits in spherical tokamaks," *Physics of Plasmas*, vol. 6, p. 1958, 1999.

[23] M. Kubic, "Review of plasma parameters of the JET tokamak in various regimes of its operation," Ph.D. dissertation, Czech Technical University, 2007.

[24] F. Wagner, G. Becker, K. Behringer, D. Campbell, A. Eberhagen, W. Engelhardt, G. Fussmann, O. Gehre, J. Gernhardt, G. v. Gierke, G. Haas, M. Huang, F. Karger, M. Keilhacker, O. Kl uber, M. Kornherr, K. Lackner, G. Lisitano, G. G. Lister, H. M. Mayer, D. Meisel, E. R. M uller, H. Murmann, H. Niedermeyer, W. Poschenrieder, H. Rapp, H. R ohr, F. Schneider, G. Siller, E. Speth, A. St abler, K. H. Steuer, G. Venus, O. Vollmer, and Z. Y u, "Regime of Improved Confinement and High Beta in Neutral-Beam-Heated Divertor Discharges of the ASDEX Tokamak," *Physical Review Letters*, vol. 49, p. 1408, 1982.

[25] K. H. Burrell, "Summary of experimental progress and suggestions for future work (H mode confinement)," *Plasma Physics and Controlled Fusion*, vol. 36, p. A291, 1994.

[26] F. Wagner, "A quarter-century of H-mode studies," *Plasma Physics and Controlled Fusion*, vol. 49, p. B1, 2007.

[27] A. Kirk, N. B. Ayed, G. Counsell, B. Dudson, T. Eich, A. Herrmann, B. Koch, R. Martin, A. Meakins, S. Saarelma, R. Scannell, S. Tallents, M. Walsh, H. R. Wilson, and the MAST Team, "Filament structures at the plasma edge on MAST," *Plasma Physics and Controlled Fusion*, vol. 48, p. B433, 2006.

[28] R. J. Groebner, "An emerging understanding of H-mode discharges in tokamaks," *Physics of Fluids B: Plasma Physics*, vol. 5, p. 2343, 1993.

[29] ASDEX Team, "The H-mode of ASDEX," *Nuclear Fusion*, vol. 29, p. 1959, 1989.

[30] M. E. Manso, "Reflectometry in fusion devices," *Plasma Physics and Controlled Fusion*, vol. 35, p. B141, 1993.

[31] A. R. Field and others, "The influence of gas fuelling location on H-mode access in the MAST spherical tokamak," *Plasma Physics and Controlled Fusion*, vol. 46, p. 981, 2004.

[32] J.-K. Park, R. E. Bell, S. M. Kaye, W. M. Solomon, B. P. LeBlanc, A. Diallo, J. E. Menard, S. Kubota, and the NSTX Research Team, "Intrinsic rotation generation in NSTX ohmic H-mode plasmas," *Nuclear Fusion*, vol. 53, p. 063012, 2013.

[33] J. W. Connor and H. R. Wilson, "A review of theories of the L-H transition ," *Plasma Physics and Controlled Fusion*, vol. 42, p. R1, 2000.

[34] Z. Yan, G. R. McKee, R. Fonck, P. Gohil, R. J. Groebner, and T. H. Osborne, "Observation of the L-H Confinement Bifurcation Triggered by a Turbulence-Driven Shear Flow in a Tokamak Plasma," *Physical Review Letters*, vol. 112, p. 125002, 2014.

[35] ITPA Confinement and H-mode Threshold Database Working Group, H-mode Threshold Database Working Group, and p. b. J. A. S. Snipes, "Multi-Machine Global Confinement and H-mode Threshold Analysis," in *19th Annual IAEA Fusion Energy Conference*, 2002.

[36] Y. Ma, J. W. Hughes, A. E. Hubbard, B. LaBombard, R. M. Churchill, T. Golfinopolous, N. Tsujii, and E. S. Marmar, "Scaling of H-mode threshold power and L–H edge conditions with favourable ion grad- Bdrift in Alcator C-Mod tokamak," *Nuclear Fusion*, vol. 52, no. 2, p. 023010, 2012.

[37] T. N. Carlstrom, M. Shimada, K. H. Burrell, J. DeBoo, P. Gohil, R. Groebner, C. Hsieh, H. Matsumoto, and P. Trost, "H-mode Transition Studies in DIII-D," in *Proceedings of the 16th European Conference on Controlled Fusion and Plasma PHysics*, Venice, 1989, p. 241.

[38] K. H. Burrell, S. L. Allen, G. Bramson, N. H. Brooks, R. W. Callis, T. N. Carlstrom, M. S. Chu, A. P. Colleraine, D. Content, J. C. DeBoo, R. R. Dominguez, J. R. Ferron, R. L. Freeman, P. Gohil, C. M. Greenfield, R. J. Groebner, G. Haas, W. W. Heidbrink, D. N. Hill, F. L. Hinton, R. M. Hong, W. Howl, C. L. Hsieh, G. L. Jackson, G. L. Jahns, R. A. James, A. G. Kellman, J. Kim, L. L. Lao, E. A. Lazarus, T. Lehecka, J. Lister, J. Lohr, T. C. Luce, J. L. Luxon, M. A. Mahdavi, H. Matsumoto, M. Mayberry, C. P. Moeller, Y. Neyatani, T. Ohkawa, N. Ohyabu, T. Okazaki, T. H. Osborne, D. O. Overskei, T. Ozeki, A. Peebles, S. Perkins, M. Perry, P. I. Petersen, T. W. Petrie, R. Philipona, J. C. Phillips, R. Pinsker, P. A. Politzer, G. D. Porter, R. Prater, M. E. Rensink, M. J. Schaffer, D. P. Schissel, J. T. Scoville, R. P. Seraydarian, M. Shimada, T. C. Simonen, R. T. Snider, G. M. Staebler, B. W. Stallard, R. D. Stambaugh, R. D. Stav, H. S. John, R. E. Stockdale, E. J. Strait, T. P. L, T. S. Taylor, P. K. Trost, U. Stroth, R. E. Waltz, S. M. Wolfe, R. D. Wood, and D. Wroblewski, "Confinement physics of H-mode discharges in DIII-D," *Plasma Physics and Controlled Fusion*, vol. 31, p. 1649, 1989.

[39] H. Meyer, P. G. Carolan, G. D. Conway, G. Cunningham, L. Horton, A. Kirk, R. Maingi, F. Ryter, S. Saarelma, and J. Schirmer, "H-mode physics of near double null plasmas in MAST and its applications to other tokamaks," *Nuclear Fusion*, vol. 46, p. 64, 2006.

[40] R. Maingi, S. M. Kaye, R. E. Bell, T. M. Biewer, C.-S. Chang, D. A. Gates, S. P. Gerhardt, J. Hosea, B. P. LeBlanc, and H. Meyer, "Overview of L–H power threshold studies in NSTX," *Nuclear Fusion*, vol. 50, p. 064010, 2010.

[41] P. Gohil, T. C. Jernigan, T. H. Osborne, J. T. Scoville, and E. J. Strait, "The torque dependence of the H-mode power threshold in hydrogen, deuterium and helium plasmas in DIII-D," *Nuclear Fusion*, vol. 50, p. 064011, 2010.

[42] F. Ryter, T. Putterich, M. Reich, A. Scarabosio, E. Wolfrum, R. Fischer, M. Gemisic Adamov, N. Hicks, B. Kurzan, C. Maggi, R. Neu, V. Rohde, G. Tardini, and the ASDEX Upgrade TEAM, "H-mode threshold and confinement in helium and deuterium in ASDEX Upgrade," *Nuclear Fusion*, vol. 49, p. 062003, 2009.

[43] ITPA H-mode Power Threshold Database and p. b. T. Takizuda, "Roles of aspect ratio, absolute B and effective Z of the H-mode power threshold in tokamaks of the ITPA database," *Plasma Physics and Controlled Fusion*, vol. 46, p. A227, 2004.

[44] E. J. Doyle, A. M. Garofalo, and C. M. Greenfield, "Progress on advanced tokamak and steady-state scenario development on DIII-D and NSTX ," *Plasma Physics and Controlled Fusion*, vol. 48, p. B39, 2006.

[45] P. C. Stangeby, *The Plasma Boundary of Magnetic Fusion Devices*. CRC Press, 2000.

[46] Y. Ma, "Study of H-mode access in the Alcator C-Mod tokamak: density, toroidal field and divertor geometry dependence," in *24th IAEA Fusion Energy Conference*, San Diego, USA, 2012.

[47] P. B. Snyder, T. H. Osborne, K. H. Burrell, R. J. Groebner, A. W. Leonard, R. Nazikian, D. M. Orlov, O. Schmitz, M. R. Wade, and H. R. Wilson, "The EPED pedestal model and edge localized mode-suppressed regimes: Studies of quiescent H-mode and development of a model for edge localized mode suppression via resonant magnetic perturbations," *Physics of Plasmas*, vol. 19, p. 056115, 2012.

[48] A. Kirk, G. F. Counsell, G. Cunningham, J. Dowling, M. Dunstan, H. Meyer, M. Price, S. Saarelma, R. Scannell, M. Walsh, H. R. Wilson, and the MAST Team, "Evolution of the pedestal on MAST and the implications for ELM power loadings," *Plasma Physics and Controlled Fusion*, vol. 49, p. 1259, 2007.

[49] D. A. Mossessian, P. B. Snyder, M. Greenwald, J. W. Hughes, Y. Lin, A. Mazurenko, S. Medvedev, H. R. Wilson, and S. Wolfe, "H-mode pedestal characteristics and MHD stability of the edge plasma in Alcator C-Mod," *Plasma Physics and Controlled Fusion*, vol. 44, p. 423, 2002.

[50] J. W. Connor, A. Kirk, and H. R. Wilson, "Edge Localised Modes (ELMs): Experiments and Theory," *AIP Conference Proceedings*, vol. 1013, p. 174, 2008.

[51] A. Diallo, J. Canik, G. J. Kramer, S.-H. Ku, J. Manickam, R. Maingi, D. Smith, P. Snyder, T. Osborne, R. E. Bell, C.-S. Chang, W. Guttenfelder, B. P. LeBlanc, and S. Sabbagh, "Progress in characterization of the pedestal structure, stability and fluctuations during ELM cycle on NSTX," in *24th IAEA Fusion Energy Conference*, San Diego, 2012.

[52] J. W. Connor, "Magnetic geometry, plasma profiles, and stability," *Plasma Physics Reports*, vol. 32, p. 539, 2006.

[53] P. B. Snyder, H. R. Wilson, J. R. Ferron, L. L. Lao, A. W. Leonard, D. Mossessian, M. Murakami, T. H. Osborne, A. D. Turnbull, and X. Q. Xu, "ELMs and constraints on the H-mode pedestal: peeling–ballooning stability calculation and comparison with experiment," *Nuclear Fusion*, vol. 44, p. 320, 2004.

[54] P. B. Snyder, N. Aiba, M. Beurskens, and R. J. Groebner, "Pedestal stability comparison and ITER pedestal prediction ," *Nuclear Fusion*, vol. 49, p. 08035, 2009.

[55] P. B. Snyder, K. H. Burrell, H. R. Wilson, M. S. Chu, M. E. Fenstermacher, A. W. Leonard, R. A. Moyer, T. H. Osborne, M. Umansky, W. P. West, and X. Q. Xu, "Stability and dynamics of the edge pedestal in the low collisionality regime: physics mechanisms for steady-state ELM-free operation," *Nuclear Fusion*, vol. 47, p. 961, 2007.

[56] P. A. Schneider, E. Wolfrum, R. J. Groebner, T. H. Osborne, M. N. A. Beurskens, M. G. Dunne, J. R. Ferron, S. Günter, B. Kurzan, K. Lackner, P. B. Snyder, H. Zohm, the ASDEX Upgrade TEAM, the DIII-D Team, and JET EFDA Contributors, "Differences in the H-mode pedestal width of temperature and density," *Plasma Physics and Controlled Fusion*, vol. 54, p. 105009, 2012.

[57] R. J. Groebner, C.-S. Chang, J. W. Hughes, R. Maingi, P. B. Snyder, X. Q. Xu, J. A. Boedo, D. P. Boyle, J. D. Callen, J. M. Canik, I. Cziegler, E. M. Davis, A. Diallo, P. H. Diamond, J. D. Elder, D. P. Eldon, D. R. Ernst, D. P. Fulton, M. Landreman, A. W. Leonard, J. D. Lore, T. H. Osborne, A. Y. Pankin, S. E. Parker, T. L. Rhodes, S. P. Smith, A. C. Sontag, W. M. Stacey, J. Walk, W. Wan, E. H. J. Wang, J. G. Watkins, A. E. White, D. G. Whyte, Z. Yan, E. A. Belli, B. D. Bray, J. Candy, R. M. Churchill, T. M. Deterly, E. J. Doyle, M. E. Fenstermacher, N. M. Ferraro, A. E. Hubbard, I. Joseph, J. E. Kinsey, B. LaBombard, C. J. Lasnier, Z. Lin, B. L. Lipschultz, C. Liu, Y. Ma, G. R. McKee, D. M. Ponce, J. C. Rost, L. Schmitz, G. M. Staebler, L. E. Sugiyama, J. L. Terry, M. V. Umansky, R. E. Waltz, S. M. Wolfe, L. Zeng, and S. J. Zweben, "Improved understanding of physics processes in pedestal structure, leading to improved predictive capability for ITER," *Nuclear Fusion*, vol. 53, p. 093024, 2013.

[58] P. A. Schneider, E. Wolfrum, R. J. Groebner, T. H. Osborne, M. N. A. Beurskens, B. Kurzan, T. Putterich, E. Viezzer, the ASDEX Upgrade TEAM, the DIII-D Team, and JET EFDA Contributors, "Analysis of temperature and density pedestal in a multi-machine database," in *24th IAEA Fusion Energy Conference*, San Diego, 2012.

[59] G. T. A. Huysmans, "ELMs: MHD instabilities at the transport barrier," *Plasma Physics and Controlled Fusion*, vol. 47, p. B165, 2005.

[60] C. F. Maggi, "Progress in understanding the physics of the H-mode pedestal and ELM dynamics," *Nuclear Fusion*, vol. 50, p. 066001, 2010.

[61] H. R. Wilson, S. C. Cowley, A. Kirk, and P. B. Snyder, "Magneto-hydrodynamic stability of the H-mode transport barrier as a model for edge localized modes: an overview," *Plasma Physics and Controlled Fusion*, vol. 48, p. A71, 2006.

[62] D. N. Hill, "A review of ELMs in divertor tokamaks," *Journal of Nuclear Materials*, vol. 241-243, p. 182, 1997.

[63] C. P. Perez, H. R. Koslowski, G. T. A. Huysmans, T. C. Hender, P. Smeulders, B. Alper, E. d. l. Luna, R. J. Hastie, L. Meneses, M. F. F. Nave, V. Parail, M. Zerbini, and J. E. Contributors, "Type-I ELM precursor modes in JET," *Nuclear Fusion*, vol. 44, p. 609, 2004.

[64] R. Maingi, C. E. Bush, E. D. Fredrickson, D. A. Gates, S. M. Kaye, B. P. LeBlanc, J. E. Menard, H. Meyer, D. Mueller, and N. Nishino, "H-mode pedestal, ELM and power threshold studies in NSTX," *Nuclear Fusion*, vol. 45, p. 1066, 2005.

[65] T. Kass, S. Günter, M. Maraschek, W. Suttrop, H. Zohm, and the ASDEX Upgrade TEAM, "Characteristics of type I and type III ELM precursors in ASDEX upgrade," *Nuclear Fusion*, vol. 38, p. 111, 1998.

[66] S. Ethier, W. M. Tang, R. Walkup, and L. Oilker, "Large-scale gyrokinetic particle simulation of microturbulence in magnetically confined plasmas," *IBM Journal of Resarch and Development*, vol. 52, p. 105, 2008.

[67] P. N. Yushmanov, T. Takizuka, K. S. Riedel, O. Kardaun, J. G. Cordey, S. M. Kaye, and D. E. Post, "Scalings for tokamak energy confinement," *Nuclear Fusion*, vol. 30, p. 1999, 1990.

[68] S. M. Kaye, M. Greenwald, U. Stroth, O. Kardaun, A. Kus, D. Schissel, J. DeBoo, G. Bracco, K. Thomsen, J. G. Cordey, Y. Miura, T. Matsuda, H. Tamai, T. Takizuda, T. Hirayama, H. Kikuchi, O. Naito, A. Chudnovskij, J. Ongena, and G. Hoang, "ITER L mode confinement database," *Nuclear Fusion*, vol. 37, p. 1303, 1997.

[69] M. Ono, M. G. Bell, R. E. Bell, T. Bigelow, and M. Bitter, "Overview of the initial NSTX experimental results ," *Nuclear Fusion*, vol. 41, p. 1435, 2002.

[70] D. C. Robinson, "The physics of spherical confinement systems," *Plasma Physics and Controlled Fusion*, vol. 41, p. A143, 1999.

[71] N. J. Conway, P. G. Carolan, C. M. Roach, A. Sykes, R. J. Akers, G. F. Counsell, A. Y. Dnestrovskij, Y. N. Dnestrovskij, M. P. Gryaznevich, and C. Ribeiro, "H-mode and confinement studies in the START spherical tokamak," in *Proc of 26th EPS Conf. on Contr. Fusion and Plasma Physics*, 1999, p. 233.

[72] S. M. Kaye, M. V. von c, A. Chudnovskij, J. G. Cordey, D. McDonald, A. Meakins, K. Thomsen, R. Akers, G. Bracco, C. Brickley, C. Bush, A. Cote, J. C. DeBoo, M. Greenwald, G. T. Hoang, D. Hogweij, F. Imbeaux, Y. Kamada, O. J. W. F. Kardaun, A. Kus, S. Lebedev, V. Leonov, S. Lynch, Y. Martin, Y. Miura, J. Ongena, G. Pacher, C. C. Petty, M. Romanelli, F. Ryter, K. Shinohara, J. Snipes, J. Stober, T. Takizuda, K. Tsuzuki, and H. Urano, "The role of aspect ratio and beta in H-mode confinement scalings," *Plasma Physics and Controlled Fusion*, vol. 48, p. A429, 2006.

[73] M. Valovič, R. Akers, G. Cunningham, L. Garzotti, B. Lloyd, D. Muir, A. Patel, D. Taylor, M. Turnyanskiy, M. Walsh, and MAST Team, "Scaling of H-mode energy confinement with I_p and B_T in the MAST spherical tokamak," *Nuclear Fusion*, vol. 49, p. 075016, 2009.

[74] S. M. Kaye, S. Gerhardt, W. Guttenfelder, R. Maingi, R. E. Bell, A. Diallo, B. P. LeBlanc, and M. Podesta, "The dependence of H-mode energy confinement and transport on collisionality in NSTX," *Nuclear Fusion*, vol. 53, p. 063005, 2013.

[75] G. D. Garstka, S. J. Diem, N. W. Eidietis, R. J. Fonck, B. T. Lewicki, G. Taylor, D. J. Battaglia, M. W. Bongard, M. J. Frost, B. A. Kujak-Ford, B. J. Squires, and G. R. Winz, "The upgraded Pegasus Toroidal Experiment," *Nuclear Fusion*, vol. 46, p. S603, 2006.

[76] P. P. Wise, B. L. Lesch, H. J. S. Muntau, T. P. Intrator, R. J. Fonck, and G. R. Winz, "The Wisconsin Pegasus solenoid," *Physica B: Condensed Matter*, vol. 246-247, p. 350, 1998.

[77] S. P. Burke, "Lurch: A new control system for the Pegasus Toroidal Experiment," Master's thesis, University of Wisconsin–Madison, 2005.

[78] P. C. Stangeby and G. M. McCracken, "Plasma boundary phenomena in tokamaks," *Nuclear Fusion*, vol. 30, p. 1225, 1990.

[79] D. J. Battaglia, M. W. Bongard, R. J. Fonck, A. J. Redd, and A. C. Sontag, "Tokamak Startup Using Point-Source dc Helicity Injection," *Physical Review Letters*, vol. 102, p. 225003, 2009.

[80] D. J. D. Hartog, D. J. Craig, G. Fiksel, and J. S. Sarff, "Impurities, temperature and density in a miniature electrostatic plasma and current source," *Plasma Sources Science and Technology*, vol. 6, p. 492, 1999.

[81] R. I. Davydenko, I. I. Morozov, G. V. Roslyakov, and V. Y. Savkin, "The Proton Source in the Atom Injector for the AMBAL Installation ," *Instruments and Experimental Techniques*, vol. 6, p. 1278, 1987.

[82] E. T. Hinson, "Injector Physics of Helicity Drive in the Pegasus Toroidal Experiment," Ph.D. dissertation, University of Wisconsin-Madison, 2015.

[83] J. L. Barr, "A Lumped-Paramter Circuit Model for Local Helicity Injection Plasma Startup on the Pegasus Toroidal Experiment," Tech. Rep. Preliminary Report, 2014.

[84] L. W. Owen, T. Uckan, P. K. Mioduszewski, and A. Pospieszczyk, "H-alpha measurements and modeling of plasma confinement in TEXTOR with the ALT-II pump limiter," *Journal of Nuclear Materials*, vol. 176-177, p. 803, 1990.

[85] R. B. Howell, J. Terry, E. S. Marmar, K. W. Hill, R. Hulse, A. Janos, H. Park, A. T. Ramsey, and G. Taylor, "Z_{eff} behavior following Li and C pellet injection into TFTR," *Review of Scientific Instruments*, vol. 61, p. 3087, 1990.

[86] M. G. Burke, R. J. Fonck, M. W. Bongard, D. J. Schlossberg, and G. R. Winz, "Multi-point, high-speed passive ion velocity distribution diagnostic on the Pegasus Toroidal Experiment," *Review of Scientific Instruments*, vol. 83, p. 10D516, 2012.

[87] D. J. Schlossberg, N. L. Schoenbeck, A. S. Dowd, R. J. Fonck, J. I. Moritz, K. E. Thome, and G. R. Winz, "A Thomson scattering diagnostic on the Pegasus Toroidal experiment," *Review of Scientific Instruments*, vol. 83, p. 10E335, 2012.

[88] R. J. Fonck, A. T. Ramsey, and R. V. Yelle, "Multichannel grazing-incidence spectrometer for plasma impurity diagnosis," *Applied Optics*, vol. 21, p. 2115, 1982.

[89] M. W. Bongard, R. J. Fonck, C. C. Hegna, A. J. Redd, and D. J. Schlossberg, "Measurement of Peeling Mode Edge Current Profile Dynamics," *Physical Review Letters*, vol. 107, p. 035003, 2011.

[90] C. C. Petty, W. R. Fox, T. C. Luce, M. A. Makowski, and T. Suzuki, "Analysis of current drive using MSE polarimetry without equilibrium reconstruction," *Nuclear Fusion*, vol. 42, p. 1124, 2002.

[91] K. Tritz, "Current profile reconstruction using X-ray imaging on the PEGASUS toroidal experiment," Ph.D. dissertation, University of Wisconsin–Madison, 2002.

[92] J. L. Barr, G. M. Bodner, M. W. Bongard, M. G. Burke, R. J. Fonck, E. T. Hinson, J. M. Perry, J. A. Reusch, and D. J. Schlossberg, "Power Balance Modeling and Validation for ST Startup Using Local Helicity Injection," *Bull. Am. Phys. Soc.*, vol. 60, p. 126, 2015.

[93] C. Everson, "Plasma Boundary Reconstruction Using Magnetic Diagnostics at Pegasus Toroidal Experiment," Bachelor's Thesis, University of Wisconsin-Madison, 2014.

[94] K. E. Thome, "H-mode Studies on Pegasus," Tech. Rep. Preliminary Report, 2013.

[95] R. J. Groebner and T. N. Carlstrom, "Critical edge parameters for H-mode transition in DIII-D," *Plasma Physics and Controlled Fusion*, vol. 40, p. 673, 1998.

[96] A. C. Selden, "Simple analytic form of the relativistic Thomson scattering spectrum," *Physics Letters A*, vol. 79, p. 405, 1980.

[97] H. Zohm, "Edge localized modes (ELMs)," *Plasma Physics and Controlled Fusion*, vol. 38, p. 105, 1996.

[98] R. Maingi, T. H. Osborne, B. P. LeBlanc, R. E. Bell, J. Manickam, P. B. Snyder, J. E. Menard, D. K. Mansfield, H. W. Kugel, R. Kaita, S. P. Gerhardt, S. A. Sabbagh, and F. A. Kelly, "Edge-Localized-Mode Suppression through Density-Profile Modification with Lithium-Wall Coatings in the National Spherical Torus Experiment," *Physical Review Letters*, vol. 103, p. 075001, 2009.

[99] J. W. Connor, "Edge-localized modes -physics and theory," *Plasma Physics and Controlled Fusion*, vol. 40, p. 531, 1998.

[100] J. R. Myra, "Current carrying blob filaments and edge-localized-mode dynamics," *Physics of Plasmas*, vol. 14, p. 102314, 2007.

[101] S. J. P. Pamela, G. T. A. Huysmans, M. N. A. Beurskens, S. Devaux, T. Eich, S. Benkadda, and JET EFDA Contributors, "Nonlinear MHD simulations of edge-localized-modes in JET," *Plasma Physics and Controlled Fusion*, vol. 53, p. 054014, 2011.

[102] L. L. Lao, H. S. John, R. D. Stambaugh, and W. Pfeiffer, "Separation of $\bar{\beta}_p$ and ℓ_i in tokamaks of non-circular cross-section," *Nuclear Fusion*, vol. 25, p. 1421, 1985.